



TECHNISCHE
UNIVERSITÄT
WIEN

DIPLOMARBEIT

Design and setup of a cold atom experiment with potassium

ausgeführt am Atominstitut



der Technische Universität Wien
Fakultät für Physik

unter der Anleitung von
Ass.Prof. Dr. Philipp Haslinger

durch

Matthias Kolb

Matrikelnummer: 01425976

Johann Böhm-Gasse 4
2201 Gerasdorf

Wien, am 01.09.2020

Abstract

The development of laser cooling techniques has led to a plethora of exciting experiments, from investigating quantum-mechanical phenomena such as Schrödinger cat states and Bose-Einstein condensates to basic tests of the standard model of physics using the unprecedented sensitivity of atom interferometry. This thesis describes the design and first steps of a cold atom setup with potassium to implement lattice atom interferometry (LATIN), to investigate light induced atom-atom interactions or to coherently drive hyperfine transitions using the near field of a density modulated electron beam. The laser setup is designed to produce the desired frequencies to cool potassium atoms, and the controlling system, including DDS frequency generators, has been set up. Also, simulations for magnetic field coils have been carried out.

Zusammenfassung

Die Entwicklung von Laserkühltechniken hat zu einer Fülle an Experimenten geführt, von der Untersuchung quantenmechanischer Phänomene wie Schrödingerkatzenzustände und Bose-Einstein-Kondensaten bis zu Tests des Standardmodells der Teilchenphysik mit der beispiellosen Sensitivität der Atominterferometrie. Diese Diplomarbeit beschreibt das Design und die ersten Schritte des Aufbaus eines Experiments mit kalten Kalium-Atomen, um geführte Atominterferometrie in einem optischen Resonator zu betreiben (engl. Lattice ATom INterferometry, kurz LATIN), lichtinduzierte Wechselwirkungen zwischen Atomen zu untersuchen oder zum ersten Mal Hyperfineübergänge mit dem Nahfeld eines dichtemodulierten Elektronenstrahls zu treiben. Der Aufbau des Lasersystems wurde entworfen um die benötigten Laserfrequenzen zu erhalten und das Experiment-Kontrollsystem mit digitalen Frequenzgeneratoren (DDS) wurde aufgebaut. Des weiteren wurden Simulationen für die benötigten Magnetfeldspulen ausgeführt.

Contents

1. Introduction	1
2. Theory	4
2.1. Doppler cooling	4
2.2. Potassium	8
2.2.1. Feshbach resonances	10
2.3. Spectroscopy	13
2.3.1. Saturation spectroscopy	13
2.3.2. Frequency modulation spectroscopy	16
2.3.3. Modulation transfer spectroscopy	19
2.4. Magneto-optical trap	19
2.4.1. 1-dimensional magneto-optical trap	20
2.4.2. 3-dimensional MOT	22
2.4.3. Single-beam magneto-optical trap	23
2.5. MOT loading	25
2.5.1. Loading from background gas	26
2.5.2. Zeeman slower	28
2.5.3. The low velocity intense source	28
2.5.4. 2D MOT	29
2.5.5. Pyramidal LVIS	31
2.5.6. Conclusion	31
2.6. Compressing the MOT	32
2.6.1. CMOT	32
2.6.2. Dark SPOT	33
2.7. Sub-Doppler cooling	33
2.7.1. Polarization gradient cooling with circularly polarized light	34
2.7.2. Gray molasses cooling	37
2.8. Optical dipole trap	41
2.9. Raman sideband cooling	43
2.9.1. Raman sideband cooling to BEC	45

3. Experimental setup	46
3.1. Vacuum setup	47
3.1.1. Science chamber	49
3.1.2. 2D MOT	49
3.2. Laser setup	50
3.3. Optical setup	56
3.4. Frequency generation with direct digital synthesis	61
3.5. Controlling system	65
3.6. Magnetic field coils	68
3.6.1. 3D MOT gradient coils	68
3.6.2. 2D MOT	69
3.6.3. Compensation coils	72
3.7. Imaging	74
3.7.1. Estimation of the atom number	75
3.7.2. Temperature measurement	75
4. Outlook	77
Appendix	78
A. DDS Frequency generator design and schematics	78
List of Figures	82
List of Tables	84
List of Symbols	85
References	88

1. Introduction

In the last quarter of the twentieth century, techniques for cooling and trapping neutral atoms (mostly alkalis due to the favorable transitions since they are “hydrogen-like“) in the sub-mK regime have been developed [1]. This led to bosonic atoms being cooled to a common ground state where their wavefunctions overlap. The resulting “quantum gas” is called a Bose-Einstein condensate (below a critical temperature depending on the density of the atoms, [2],[3]).

These developments initiated a new area of research where the properties of the quantum gases were studied, demonstrating effects such as phase transitions and Higgs and Goldstone modes that resemble phenomena in condensed matter and particle physics [4]. By trapping atoms in optical lattices, Hamiltonians like the Bose-Hubbard model can be implemented, making it possible to simulate those systems (“Quantum Simulator”, [5]).

Furthermore, the feasibility of laser cooling atoms has led to atom interferometry. Using the recoil momentum $\hbar k_{eff}$ of a two-photon Raman transition, where k_{eff} is the wave vector of laser light driving the transition, an atomic cloud is split in two parts and finally recombined. It is important to note that each atom has a 50 % chance to undergo this transition and its wavefunction is thus split in two parts. The spatial separation of the two clouds allows to measure accelerations a , e.g. variations of the gravitational field. The phase difference $\Delta\phi$ accumulated when recombining the two atomic clouds is approximately (the leading order in a)

$$\Delta\phi \approx k_{eff}aT^2 \quad (1.1)$$

with the evolution time T . Further improvements, such as stronger lasers or the use of cavities for power enhancement allow for multiphoton interactions (thereby increasing k_{eff}) leading to higher sensitivities, has triggered experiments to check theoretical models for dark energy [6], to investigate the effect of blackbody radiation on atoms [7] and precision measurements of the fine structure constant [8].

In addition of increasing the recoil momentum, the evolution time T between the Raman pulses has been elongated by launching atoms upwards (where T is limited by the time the atoms are in free fall, [9]), using parabolic flights [10] and drop towers

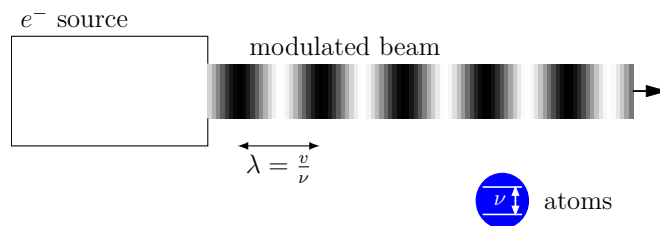


Figure 1.1.: The proposed Quantum Klystron experiment: A density modulated electron beam with velocity v passes by a cloud of atoms. The frequency ν of the density modulation (λ is its wavelength) equals the transition frequency of the ground state hyperfine transition ($F = 1$ to $F = 2$ in fig. 2.2). The varying beam current causes an oscillating magnetic field experienced by the atoms, thereby imitating a photon which is normally used to drive the transition.

[11]. Recently it was demonstrated that by trapping the atoms of the two arms of an interferometer into an optical lattice, it is possible to achieve interferometry times of 20 seconds [12].

A theoretical proposal [13] suggests to drive transitions such as the magnetic dipole hyperfine transitions of alkalis by an electron beam with modulated density. The varying electron density (where the frequency of the variation equals the frequency of the atomic transition) leads to a varying electro-magnetic field, which imitates a microwave photon which is generally used to drive magnetic dipole transitions (see fig. 1.1). For electrons with a kinetic energy of 18 kV, the de Broglie wavelength is $\approx 1 \text{ \AA}$, whereas the wavelength of the photons for these transition is in the range of centimeters. Driving transitions with electron beams would make it possible to address smaller regions in an atomic cloud or even single atoms when trapped in an optical lattice, depending on the beam diameter. The modulation of an electron beam is known to be used in a *Klystron*, where an electron beam modulated while passing through a cavity is used to amplify microwave signals by inducing a voltage in a second cavity. The proposed experiment can be viewed as a Klystron [14] where the second cavity is replaced by atoms, and is therefore called *Quantum Klystron* (QUAK). With this electron beam, the transitions are driven coherently, and Rabi oscillations should be observable. This could facilitate applications for quantum computing by driving and coupling atomic qubits (e.g. atoms trapped in optical lattices or with tweezers, [15], [16]). In addition, spectroscopic measurements in scanning electron microscopy could lead to a higher signal when driving transitions in the specimen *on resonance*, compared to incoherent scattering processes [13], and in biological electron microscopy, the radiation damage could be reduced by indirectly driving transitions [17].

The scope of this thesis is to build up an experiment to cool and trap ^{39}K and ^{41}K to low temperatures needed for lattice atom interferometry. With this setup, called

LATIN, it is planned to search for new physics e.g. forces caused by dark energy. In addition, light-induced inter-particle interactions shall be investigated [18]. Finally, the setup allows for implementation of the proposed QUAK experiment.

The setup consists of a *science chamber* with a 3-dimensional magneto-optical trap (MOT), loaded by an atomic beam generated by a 2-dimensional MOT. The 2D-MOT ensures fast loading rates to shorten the experiment cycle. For the two magneto-optical traps, laser light stabilized to the D2 line of potassium is needed. To cool the atoms to even lower temperatures (on the order of a few microkelvins), a gray molasses cooling scheme on the D1 line is used [19]. If needed, Raman sideband cooling [20] can be used to achieve lower temperatures and prepare all atoms in one magnetic sub-state. Afterwards, the atoms can be loaded into an optical lattice (for atom interferometry) or highly confined in an optical dipole trap (for QUAK). A transfer chamber which can be separated from the science chamber by a valve will be used to easily exchange electron sources for the QUAK experiment and also allows for insertion of test masses or surfaces to measure interactions with *LATIN*.

In this thesis, the theoretical background of the laser cooling is outlined in chapter 2, where techniques that will be used in the planned setup to cool and trap atoms are explained. One subsection also addresses spectroscopy methods, which are needed to stabilize the lasers on the desired frequencies. In chapter 3 the experimental setup is shown, with a focus on the optical and electronic systems. Simulations conducted to design magnetic fields needed to trap atoms are presented as well as first magnetic field measurements.

2. Theory

This chapter covers the theory of laser cooling of potassium. Doppler cooling and magneto-optical traps are explained and the peculiarities of the potassium level structure are outlined. Different ways of loading the trap are discussed, and possible miniaturizations of the setup are further explored. Techniques to cool the atoms to temperatures below a few μK are compared. The concept of an optical dipole trap is presented, making it possible to hold atoms in absence of a magnetic field. Furthermore, two spectroscopy-based laser stabilization methods, which are used in the setup, are shown.

2.1. Doppler cooling

The Doppler cooling technique can be used to cool atoms at room temperature ($T = 300\text{ K}$ implies a mean velocity of $\approx 400\text{ m s}^{-1}$ for ^{39}K , [21, p.195]) to the sub-mK regime and is generally the first step in cold atom experiments. The following derivation mainly follows [22].

In a simplified model, atoms are pictured as two-level systems (see figure 2.1a). They can be excited from the ground state $|g\rangle$ using a laser beam at frequency ω_L matching the transition frequency ω_0 . The excitation of the atom does not only change its state to $|e\rangle$, but, since the photon is absorbed by the atom, it also exerts a recoil momentum of $\hbar k_L$ on the atom (this corresponds to a velocity change of $\approx 1.3\text{ m s}^{-1}$ in case of ^{39}K atoms, [23]). Thus, if beam and atom are moving towards (with) each other, the atom is decelerated (accelerated). At nonzero temperatures the Doppler effect must be considered: An atom moving towards a laser beam with wave vector \vec{k}_L at a velocity \vec{v} experiences the laser frequency increased by $+\vec{k}_L \cdot \vec{v}$, as shown in figure 2.1c [24, p. 249]. Consequently, by detuning the laser by δ to compensate for the Doppler effect, the atom is excited when moving towards the beam, being slowed down, but is off resonance when moving in the same direction as the beam. After a short time in the excited state (the lifetime τ is the inverse of the decay rate Γ and amounts to 26.4 ns for the D2 line of ^{39}K , [23, p.4]), a photon is spontaneously emitted in a random direction. The recoil momenta of these photons average out over many

scattering events (e.g. a slow potassium atom with initial speed of 10 m s^{-1} needs to scatter about 800 photons to reach a temperature of $145 \text{ } \mu\text{K}$, which is the lowest achievable temperature with Doppler cooling, see below). If the light intensity is low enough, stimulated emission, which would lead to a velocity-independent force (the stimulated emission by a photon from a similar direction would accelerate the atom), can be neglected.

The resulting force can be written as

$$F = \frac{\Delta p}{\Delta t} = \hbar k \Gamma \rho_{ee}, \quad (2.1)$$

where $\hbar k \approx \hbar k_L$ is the transferred momentum. Since this force requires spontaneous emission for the recoil momenta of the emitted photons to cancel out, the rate of this process is determined by the decay rate Γ and the population ρ_{ee} of the excited state $|e\rangle$, which is, according to the optical Bloch equations [22, p.23ff].

$$\rho_{ee} = \frac{s_0/2}{1 + s_0 + \left(\frac{2\delta}{\Gamma}\right)^2}, \quad (2.2)$$

with detuning δ , the saturation parameter at resonance $s_0 = \frac{I}{I_S}$ and the saturation intensity at resonance $I_S = \frac{\pi \hbar c \Gamma}{3 \lambda^2}$ (\hbar is Planck's constant, c the speed of light, λ is the wavelength of the atomic transition). Inserting equation 2.2 into equation 2.1, and considering the Doppler effect, one gets

$$\vec{\mathbf{F}}(\vec{\mathbf{k}}) = \frac{\hbar \vec{\mathbf{k}} s_0 \Gamma / 2}{1 + s_0 + \left[\frac{2(\delta - \vec{\mathbf{k}} \cdot \vec{\mathbf{v}})}{\Gamma}\right]^2}. \quad (2.3)$$

This equation corresponds to the force exerted on atoms with velocity $\vec{\mathbf{v}}$ by *one* laser beam with frequency ω_L detuned by δ from the atomic resonance ω_0 . In figure 2.1b, the blue dotted curve is the force of a laser beam with detuning $\delta = -\Gamma$ (the decay rate Γ was taken from table 2.1 for the D2 line), moving in positive z -direction, thus slowing down atoms propagating in $-z$ -direction. Adding a second laser in the opposite direction (with the same detuning but the opposite $\vec{\mathbf{k}}$ vector, drawn in orange in fig. 2.1b) results in the radiation pressure force $\vec{\mathbf{F}}_{OM} = \vec{\mathbf{F}}(\vec{\mathbf{k}}) + \vec{\mathbf{F}}(-\vec{\mathbf{k}})$ shown as the green curve in figure 2.1b. Neglecting terms of order $\left(\frac{\vec{\mathbf{k}} \cdot \vec{\mathbf{v}}}{\Gamma}\right)^2$ gives for small velocities

$$\vec{\mathbf{F}}_{OM} = \vec{\mathbf{F}}(\vec{\mathbf{k}}) + \vec{\mathbf{F}}(-\vec{\mathbf{k}}) \approx \frac{8 \hbar k^2 \delta s_0 \vec{\mathbf{v}}}{\Gamma \left[1 + s_0 + \left(\frac{2\delta}{\Gamma}\right)^2\right]^2} = -\beta \vec{\mathbf{v}}, \quad (2.4)$$

shown in the red dashed curve in figure 2.1b. This force is proportional to the velocity \vec{v} , can thus be regarded as a damping or friction force and is often referred to as *optical molasses*.

As mentioned above, spontaneous emission plays a key role in the Doppler cooling process. However, the scattering of photons also sets a limit to the temperatures that can be achieved, since it causes heating. When the frictional force and the heating are in equilibrium, one can calculate the minimal achievable temperature, known as the *Doppler cooling limit*. For the optimized detuning $\delta = -\frac{\Gamma}{2}$, the Doppler temperature is $T_D = \frac{\hbar\Gamma}{2k_B}$. In case of potassium $T_D = 145 \mu\text{K}$ (see tables 2.1 and 2.2).

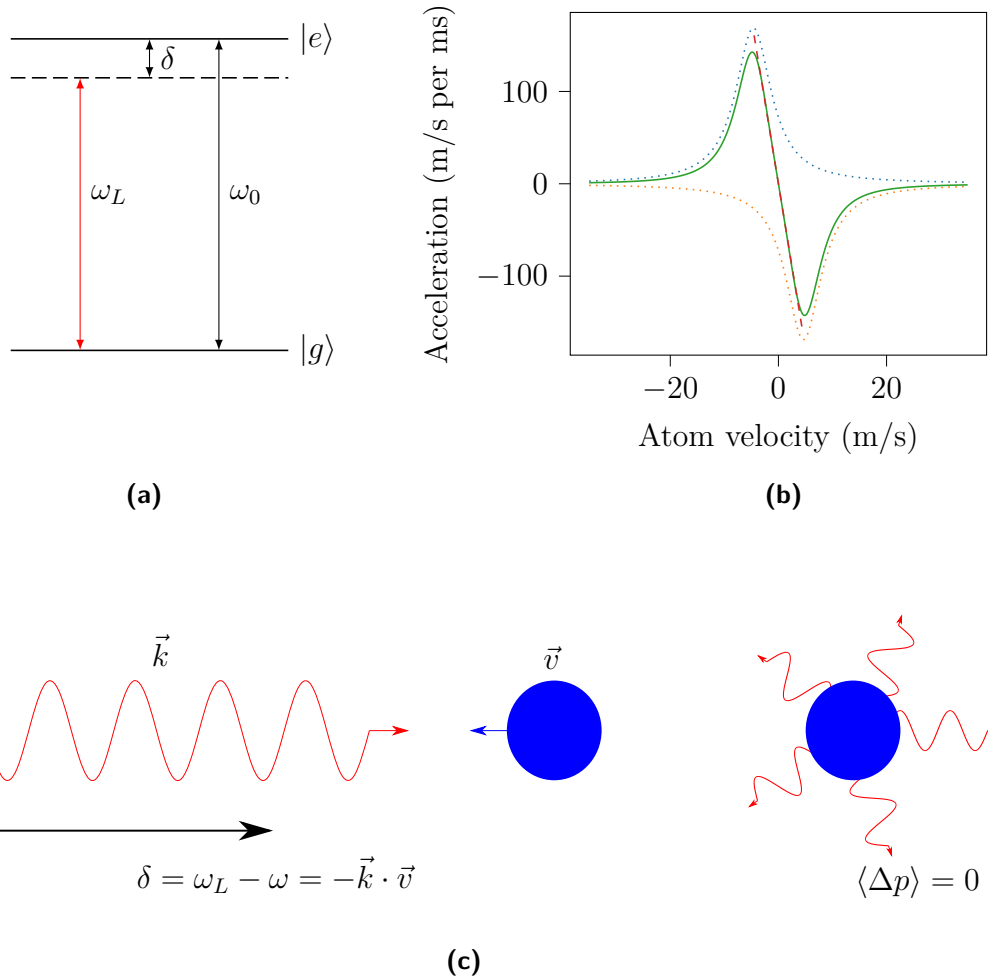


Figure 2.1.: (a) A two-level system. The laser with frequency ω_L is detuned by δ relative to the atomic transition with frequency ω . If $\delta < 0$, the laser light is *red-detuned*, for $\delta > 0$ one refers to *blue detuning*. (b) The Doppler cooling force generated by a laser beams propagating in $+z$ direction (the blue dotted line) and $-z$ direction (in orange), giving the total radiation pressure force (in green) with the saturation parameter $s_0 = 2$ and the detuning $\delta = -\gamma$. On the ordinate, the acceleration on a potassium atom is given. The values of γ and λ where taken from table 2.1 for the D2 line. For small atomic velocities, the force can be approximated as a linear friction force (the red dashed curve). (c) The Doppler cooling process: the laser beam is detuned from the atomic transition by δ to compensate for the Doppler effect. Thus, only atoms propagating in opposite direction to the laser beam are retarded. Through spontaneous emission, the atoms gets a kick of $\hbar k$ in a random direction, but are heated.

2.2. Potassium

The Doppler cooling process discussed in the previous section was explained for a two-level atom. However, real atoms have more energy levels, leading to effects that must be taken into account in order for Doppler cooling to work. This section will mainly focus on the atomic species chosen for the setup presented in this thesis, namely ^{39}K and ^{41}K .

Alkali atoms are preferable for laser cooling, since they only have one valence electron in the outer shell. The excitations of this electron form a relatively simple level structure, as shown in figure 2.2. The main structure is similar for the other alkali atoms: the $4^2\text{S}_{1/2}$ ground state can be excited to two excited states ($4^2\text{P}_{1/2}$ and $4^2\text{P}_{3/2}$) with a different spin-orbit coupling. This gives the D1 and D2 line different properties, which are shown in tables 2.1 and 2.2 for ^{39}K and ^{41}K respectively. Their frequencies are typically in the visible / near infrared part of the spectrum, which makes it easier to generate light, since appropriate lasers are readily available (CD and DVD drives used laser diodes at 780 nm and 650 nm respectively [25]). Most alkali isotopes have two hyperfine ground states due to the spin-spin interaction of the nucleus and the unpaired valence electron [22, p.39ff]. Assuming laser cooling is mediated on the D2 line via the $F=2$ ground state to the $F'=3$ excited state, the atom cannot decay to the $F=1$ ground state, due to dipole selection rules. This is called a *cycling transition*. But due to the detuning of the cooling laser from the transition, a fraction of atoms are excited to the $F'=2$ state as well. From $F'=2$ they can decay to the $F=1$ ground state and become transparent to the cooling light, resulting in atom loss. To account for this, a second laser on the $F=1$ to $F'=2$ transition is needed to pump the atoms back to the $F=2$ ground state. This laser is generally referred to as *repumper*, while the main cooler laser is called *cooler* [26, p.84].

Potassium shows one peculiarity which impacts laser cooling; the narrow hyperfine splitting in the $4^2\text{P}_{3/2}$ excited state of less than 35 MHz, compared to ≈ 496 MHz for the widely used ^{87}Rb [27], resulting in even more atoms decaying to the $F=1$ ground state (compared to ^{87}Rb , [28]). Thus, the repumper beam has to be much stronger than for Rubidium, sometimes equally strong as the cooler [29]. In this case, both cooling beams are red detuned to the whole excited state manifold. Other experimental realizations used ratios (cooler : repumper) of about 2:1 [19] or 3:1 [30]. Consequently, the term *repumper* is not adequate anymore, it should rather be referred to two cooler beams that form a closed cooling cycle. Since the majority of the publications still name them cooler and repumper, these notions will be used in this thesis too. However, it should be kept in mind that the repumper plays a more significant role when laser cooling potassium compared to other alkalies.

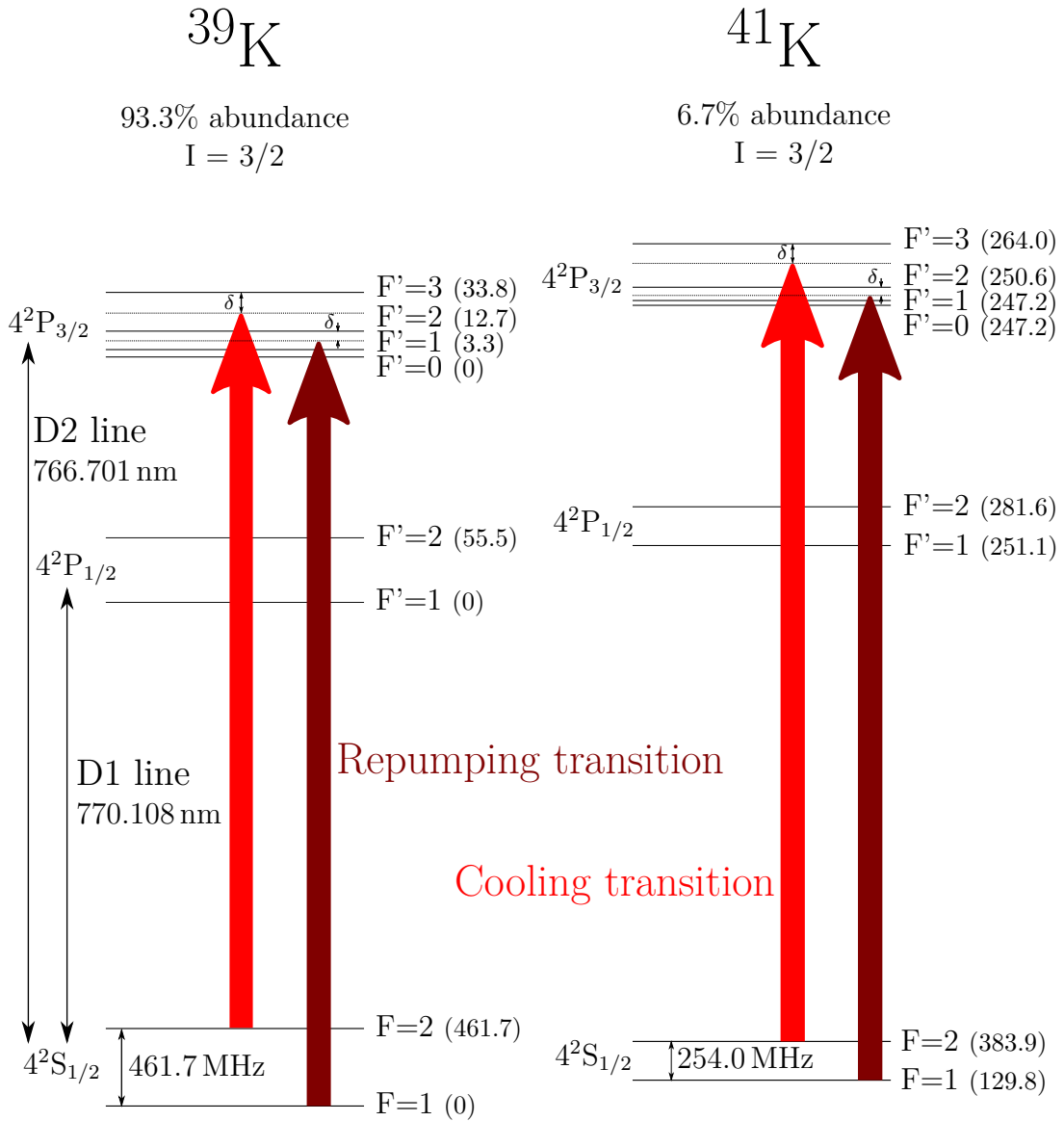


Figure 2.2.: The D1 and D2 lines of ^{39}K and ^{41}K . For each S/P-state, the relative frequencies between the hyperfine states in brackets are given in MHz. The cooler and repumper transitions are colored red and dark red, with small detuning δ . I is the nuclear spin quantum number.

2.2.1. Feshbach resonances

Scattering properties are important to consider for these types of experiments, even more so when creating Bose-Einstein condensates using evaporation cooling. In this section, the concept of a *Feshbach resonance* is explained and the experimental benefits are shown.

Regarding an atom at low energies (with a large de Broglie wavelength) scattering another atom, the *scattering length* a describes the scattering probability (its modulus) and a potential phase shift (its sign). The interaction potential between two atoms distanced by R can be described by the Lennard-Jones potential

$$V(R) \propto \frac{1}{R^{12}} - \frac{1}{R^6} \quad (2.5)$$

shown in figure 2.3a. For shorter interatomic distances, the atoms can form a molecule, represented by a bound state in the potential well [24, p.314ff]. At small energies, the collision process will take place in the *entrance channel*, or *open channel* V_o (the intermolecular state with energy ≈ 0). Coupling the open channel with the bound state of the closed channel V_c (an intermolecular state at higher energy) leads to a Feshbach resonance. Using a magnetic or optical field, the energy difference between the entrance channel and the bound state can be controlled. By changing the coupling between the states, the scattering length changes dependent on the magnetic field B (see figure 2.3b) as:

$$a(B) = a_{bg} \left(1 - \frac{\Delta}{B - B_0} \right). \quad (2.6)$$

The Feshbach resonance occurs at magnetic field B_0 , the width of the resonance is Δ . All known resonances of ^{39}K are listed in table 2.3. Compared to other atomic species, several Feshbach resonances at comparably low magnetic field facilitate the experimental implementation.

There are various applications of Feshbach resonances. In order to allow evaporation cooling to form a Bose-Einstein condensate, some atoms have unfavorable collision properties (e.g. ^{133}Cs or ^{39}K). By tuning a with a magnetic field, large positive scattering lengths needed can be achieved. By adiabatically changing the magnetic field the atoms are transferred to a molecular state to form *Feshbach molecules*. Finally, the zero-crossing can be used to reduce the interactions to minimize systematic errors, for example in atom interferometry with Bose-Einstein condensates [31].

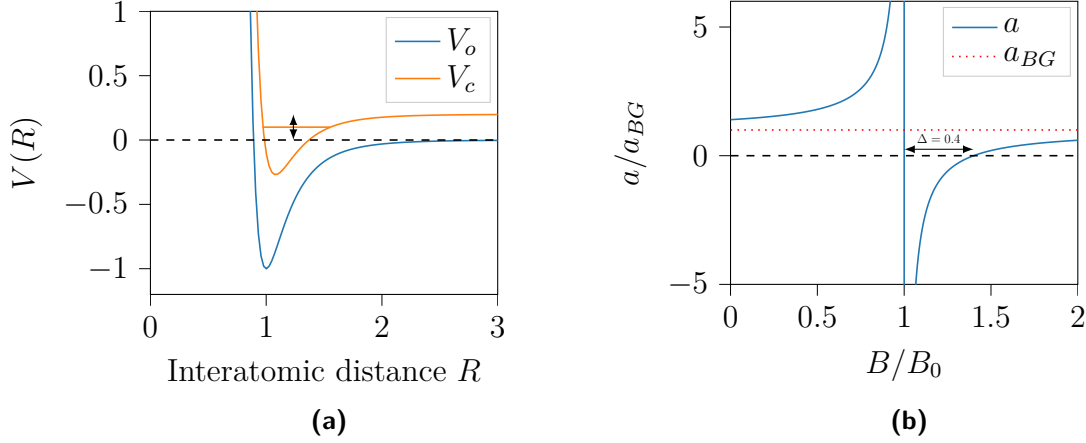


Figure 2.3.: (a) The Lennard-Jones potential describes the interaction between two atoms. If they are close, they might be bound in a molecular state. Coupling of the entrance channel V_o to the bound state of V_c leads to a *Feshbach resonance* which can be controlled with a magnetic or optical field. The values on the abscissa and the ordinate are a relative measure from a Lennard-Jones-Potential $V \propto \frac{1}{R^{12}} - \frac{1}{R^6}$. (b) The scattering length can be tuned as a consequence of the coupling between V_o and V_c . This allows to control the interaction between the atoms. At a distance Δ from the resonance B_0 , a zero crossing appears. The scattering length is given relative to the background scattering length a_{BG} (i.e. the scattering length in absence of the coupling).

Table 2.1.: Important transitions of ^{39}K . Data were taken from [23].

Property	D1 line	D2 line
wavelength λ	770.108 385 049(123) nm	766.700 921 822(24) nm
lifetime τ	26.72(5) ns	26.37(5) ns
Decay rate $\Gamma = \frac{1}{\tau}$	37.43 s $^{-1}$	37.92 s $^{-1}$
Natural linewidth $\Gamma/2\pi$	5.956(11) MHz	6.035(11) MHz
Doppler temperature T_D	145 μK	145 μK
Recoil temperature T_{rec}	0.414 367 02 μK	0.414 367 02 μK
Recoil velocity v_{rec}	1.329 825 973(7) cm s $^{-1}$	1.335 736 144(7) cm s $^{-1}$
Saturation intensity I_S		1.75 mW/cm 2

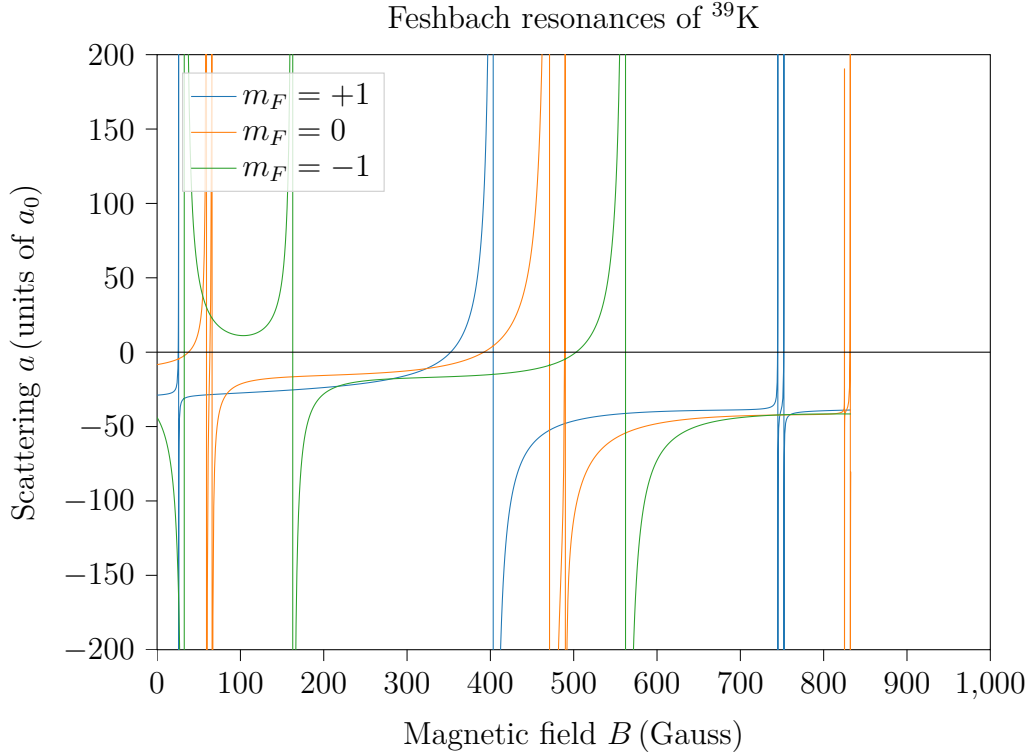


Figure 2.4.: The Feshbach resonances for ^{39}K from table 2.3 are plotted for the various m_F states. For atom interferometry, the resonances of the $m_F = 0$ state are of particular interest because this state is insensitive to magnetic fields as a first order approximation (data were taken from [32], the background scattering length a_{bg} , which varies with B , was interpolated).

Table 2.2.: Important transitions of ^{41}K . Data were taken from [23].

Property	D1 line	D2 line
wavelength λ	770.107 919 192(123) nm	766.700 458 70(2) nm
lifetime τ	26.72(5) ns	26.37(5) ns
Decay rate $\Gamma = \frac{1}{\tau}$	37.43 s $^{-1}$	37.92 s $^{-1}$
Natural linewidth $\Gamma/2\pi$	5.956(11) MHz	6.035(11) MHz
Doppler temperature T_D	145 μK	145 μK
Recoil temperature T_{rec}	0.414 082 79 μK	0.414 082 79 μK
Recoil velocity v_{rec}	1.264 957 788(6) cm s $^{-1}$	1.207 057 966 2(7) cm s $^{-1}$
Saturation intensity I_S		1.75 mW/cm 2

Table 2.3.: Feshbach resonances of ^{39}K . “exp.” and “th.” refer to experimental / theoretical values. Data were taken from [32].

m_F	B_0 (G) exp.	B_0 (G) th.	Δ (G) th.	a_{bg} (a_0) th.
1,1	25.85(10)	25.9	-0.47	-33
	403.4(7)	402.4	-52	-29
	752.3(1)	745.1	-0.4	-35
0,0	59.3(6)	58.8	-0.4	-35
	66.0(9)	65.6	-9.6	-18
		471	-7.9	-18
		490	-72	-28
		825	-5	-28
		832	-0.032	-36
-1,-1	32.6(15)	33.6	-0.52	-36
	162.8(9)	162.3	55	-19
	562.2(15)	560.7	-37	-19
		-56	-29	

2.3. Spectroscopy

Laser cooling requires precise control of the laser frequencies. Therefore, it is necessary to run the lasers at the desired frequencies and to correct frequency drifts. One way to achieve this is by locking the laser frequency to an atomic transition using spectroscopy of the atomic species that are to be cooled. Below, the most commonly used technique to see a spectrum is explained. Then, two methods for generating a feedback signal for the laser which are used in the experimental setup are shown.

2.3.1. Saturation spectroscopy

When a laser beam is sent through a vapour cell with potassium atoms, it is absorbed if its frequency ω_L is on resonance with one of the atomic transition lines. However, since the atoms in the vapour cell have a nonzero temperature (at room temperature $T \approx 300$ K), they are moving at velocities given by the Maxwell-Boltzmann distribution with a most probable velocity of about 350 m s^{-1} (see equation 2.24 and below). This gives rise to a Doppler shift, i.e. in the reference frame of an atom moving with velocity \vec{v} , a photon's frequency appears shifted by $\Delta\omega_D = -\vec{k}\vec{v}$, where \vec{k} is the wave vector of the photon. Consequently, the observed linewidth of the atomic transition is broadened by the Doppler shifts for the various velocities, resulting in a Gaussian

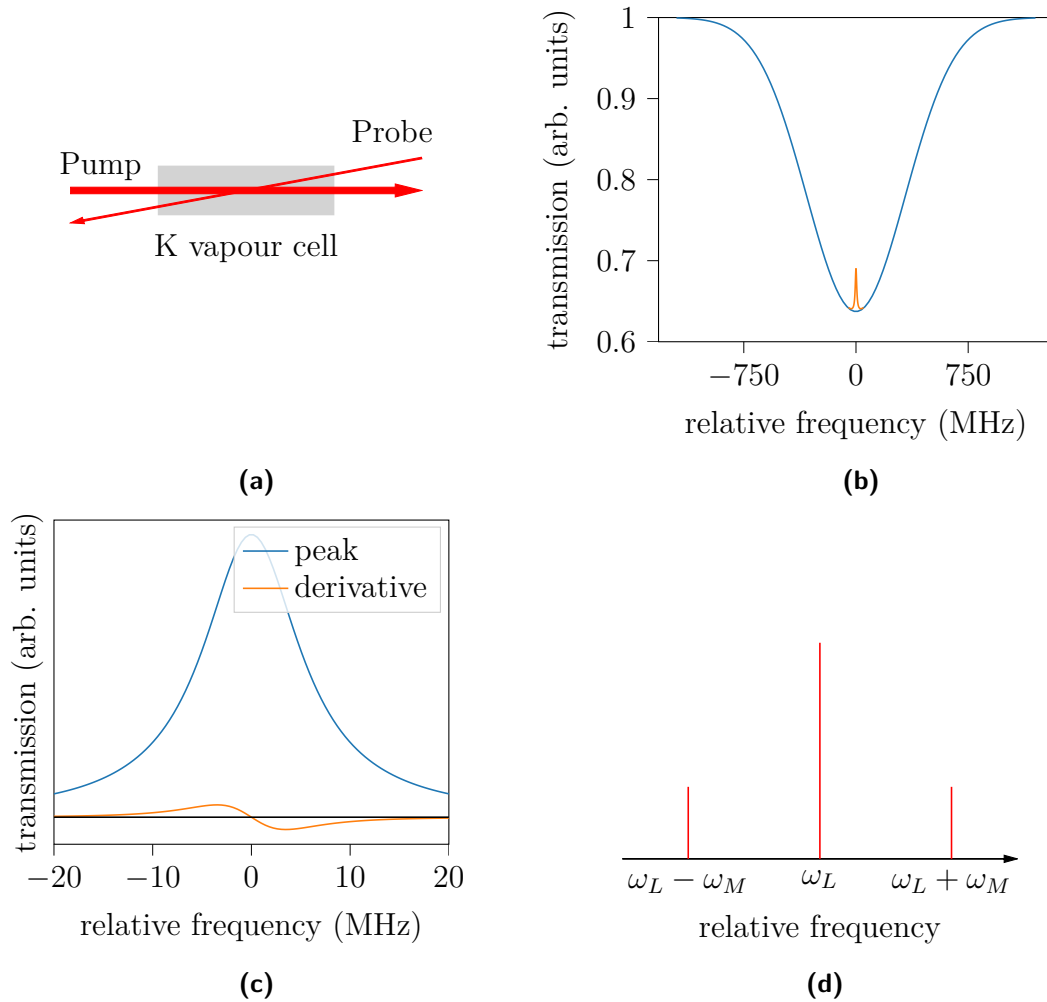


Figure 2.5.: (a) The pump-probe scheme used in saturation absorption spectroscopy to overcome the Doppler broadening (777 MHz FWHM for potassium) caused by the temperature inside the vapour cell. The pump beam saturates the atoms at velocity v it is in resonance with, while the probe beam, propagating in the opposite direction, is absorbed by atoms at $-v$. If the laser is on resonance, both beams interact with the same atoms, thereby increasing the transmission of the probe beam, due to on average half of the atoms in the excited state, due to the saturation. (b) The transmission signal obtained by scanning the frequency of the probe beam. The blue curve denotes the Doppler valley caused by absorption, the orange peak denotes the real transition with a linewidth $\Gamma \approx 2\pi \cdot 6$ MHz for potassium. (c) To stabilize the laser on the transition, frequency drifts must be compensated for. However, due to the symmetry of the peak (in blue) one does not know in which direction it deviated. This could be solved by generating the derivative (in orange). (d) To generate the derivative of the spectrum, one beam is phase modulated with a frequency ω_M , creating two additional sidebands $\omega_L \pm \omega_M$ with the central *carrier frequency* ω_L . The sidebands experience different absorption, the interference with the carrier yields the derivative.

profile with the Full Width at Half Maximum (FWHM)

$$\Delta\omega_D = \frac{\omega_0}{c} \sqrt{\frac{8k_B T \ln 2}{m}}. \quad (2.7)$$

ω_0 is the transition frequency, T the temperature of the atoms and m the atomic mass [24, pp.249–250].

For potassium, the Doppler width is 777 MHz (FWHM) at room temperature. For laser cooling, a stability better than the natural linewidth of about 6 MHz is required to be able to resolve the hyperfine transitions (which is not entirely possible for potassium D2 line). Consequently, some form of *Doppler-free Spectroscopy* is needed. The main idea is shown in figure 2.5a. A *pump beam* is sent through the vapour cell and gets absorbed which gives a Doppler valley when scanning the frequency (the blue curve in fig. 2.5b). The *probe beam*, at much lower power, passes through the cell from the opposite direction. Now assume that the laser beams are not on resonance. The pump beam is absorbed by atoms with velocity v , saturating them (on average half of the atoms with v are in the excited state). The Doppler shift can equal the detuning from resonance. The same happens in case of the probe beam, but with *different* atoms at speed $-v$, because it is propagating in the opposite direction. Thus, off resonance, scanning the probe beam gives the same blue curve as in fig. 2.5b. On resonance however, atoms with $v = 0$ are excited by both pump and probe beams thus less absorptive for the probe beam. This causes increased transmission, resulting in the orange peak in figure 2.5b, the *lamb dip*. This peak has a Lorentzian shape, and is mainly limited by the natural linewidth of the transition. Therefore saturation spectroscopy is a viable option for laser stabilization [33].

The D1 and D2 lines of alkali atoms have multiple excited states and thus multiple transition lines. When the laser is set to a frequency $(\omega_A + \omega_B)/2$ between two transition A and B at frequencies ω_A and ω_B , it is possible that the pump beam is absorbed by an atom with velocity $v > 0$ on the A transition, while the probe beam is resonant with the B transition. Because atoms with velocity v are saturated by the pump beam (thus in the excited state A), the atoms are transparent for the probe beam, resulting in a *crossover peak*, which is generally larger than the real transition. For the D2 lines, the three allowed transitions from each hyperfine state ($F = 1$ and $F = 2$ for ^{39}K and ^{41}K), form three crossovers, resulting in a total of six peaks in the spectrum. The formation of the crossovers is possible because the excited state energy splittings are small compared to the width of the Doppler valley. For ^{39}K and ^{41}K , with its narrow hyperfinesplittings of 461.7 MHz and 254.0 MHz, a crossover appears between the two hyperfine ground states is formed. This is not a peak but a hole, since atoms that have been excited by the pump beam e.g. from the $F = 2$ hyperfine ground

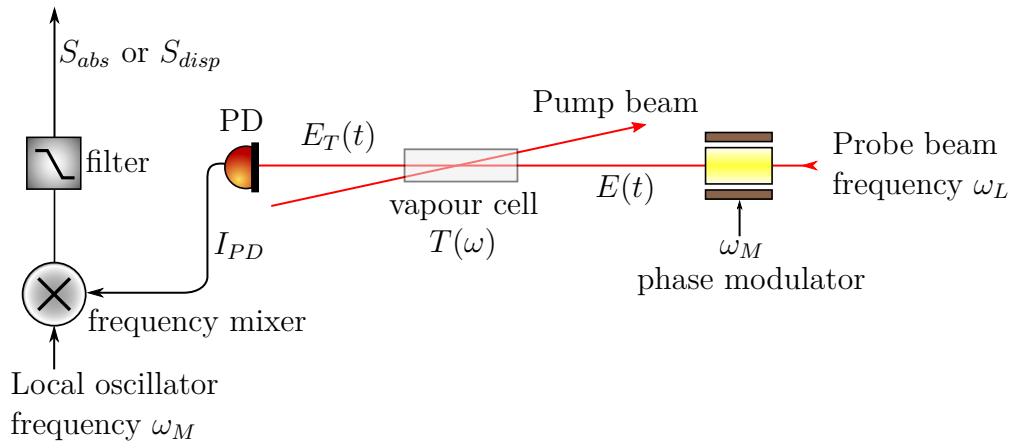


Figure 2.6.: Frequency modulation spectroscopy: the probe beam with frequency ω_L is modulated in a phase modulator with frequency ω_M , resulting in the frequency sidebands shown in fig. 2.5d. When passing through the vapour cell, the sidebands experience different transmission $T(\omega)$. The interference of the sidebands with the carrier on the photodiode PD leads to parts of the signal proportional to the derivatives δ' and ϕ'' of absorption and dispersion, which are extracted by mixing the signal with a *Local Oscillator* (at frequency ω_M) and a filter. Depending on the phase between Local Oscillator either the absorptive (S_{abs}) or dispersive (S_{disp}) part of the signal is obtained.

state can decay to the $F = 1$ ground state, and more atoms in $F = 1$ cause greater absorption of the probe beam. In addition, the Doppler valleys of the two isotopes overlap, causing crossover peaks between isotopes. The narrow hyperfine splittings in the excited state is sometimes lower than Γ causes peaks to be unresolvable, as does the smaller abundance of ^{41}K [34].

Saturation spectroscopy produces a Doppler free spectrum. In order to stabilize the laser on a certain transition, the direction of the deviation has to be known. Since the Lorentzian lamb dip is symmetric, it is convenient to use the derivative depicted in figure 2.5c. Subsequently, two techniques to generate a suitable feedback signal are introduced.

2.3.2. Frequency modulation spectroscopy

Frequency modulation spectroscopy (FMS) modulates the frequency of the probe beam, resulting in frequency sidebands (see fig. 2.5d). The transmission through the vapour cell is frequency dependent (fig. 2.5b), and the interference between carrier (the center frequency) and sidebands on a photodiode can be extracted electronically, giving the derivative of the saturation absorption spectrum.

Below, the generation of the error signal is derived, mainly following [35]. It is depicted in fig. 2.6. The electric field of the probe beam with frequency ω_L

$$E(t) = E_0 e^{i\omega_L t} \quad (2.8)$$

is phase modulated with $\psi(t) = M \sin \omega_M t$, the modulation index M describes the strength of the modulation. The resulting field is

$$E(t) = E_0 e^{i(\omega_L t + \psi(t))} = E_0 e^{i(\omega_L t + M \sin \omega_M t)}, \quad (2.9)$$

which can be rewritten for small M as

$$E(t) \approx E_0 e^{i\omega_L t} (1 + iM \sin \omega_M t) = E_0 \left(-\frac{M}{2} e^{i(\omega_L - \omega_M)t} + e^{i\omega_L t} + \frac{M}{2} e^{i(\omega_L + \omega_M)t} \right). \quad (2.10)$$

It consists of a *carrier frequency* ω_L with two frequency sidebands $\omega_L \pm \omega_M$, as depicted in figure 2.5d. The transmission through the vapour cell is described by

$$T(\omega) = e^{-\delta(\omega) - i\phi(\omega)}, \quad (2.11)$$

with absorption $\delta(\omega)$ and dispersion $\phi(\omega)$. After passing through the vapour cell, the probe beam electric field becomes

$$E_T = E_0 \left(-\frac{M}{2} T(\omega_L - \omega_M) e^{i(\omega_L - \omega_M)t} + T(\omega_L) e^{i\omega_L t} + \frac{M}{2} T(\omega_L + \omega_M) e^{i(\omega_L + \omega_M)t} \right). \quad (2.12)$$

When detected on a photodiode, neglecting terms on the order of M^2 , the measured intensity is

$$\begin{aligned} I_{PD} &= E_T^* E_T \propto T^2(\omega_0) \\ &\quad - \frac{M}{2} (T^*(\omega_L - \omega_M) T(\omega_L) e^{+i\omega_M t} + c.c.) \\ &\quad + \frac{M}{2} (T^*(\omega_L + \omega_M) T(\omega_L) e^{-i\omega_M t} + c.c.). \end{aligned} \quad (2.13)$$

E^* and T^* denote the complex conjugates of E and T respectively, “c.c.” the complex conjugate of the preceding term. Considering that $\delta(\omega)$ and $\phi(\omega)$ are small, second-

order terms can be neglected giving the simplified expression

$$\begin{aligned}
 I_{PD} &\propto 1 - 2\delta \\
 &- \frac{M}{2} (1 - \delta(\omega_L - \omega_M) - \delta(\omega_M)) (1 + i\phi(\omega_L - \omega_M) - i\phi(\omega_L)) e^{+i\omega_M t} + c.c. \\
 &+ \frac{M}{2} (1 - \delta(\omega_L + \omega_M) - \delta(\omega_M)) (1 + i\phi(\omega_L + \omega_M) - i\phi(\omega_L)) e^{-i\omega_M t} + c.c.
 \end{aligned} \tag{2.14}$$

Rearranging gives

$$\begin{aligned}
 I_{PD} &\propto 1 - 2\delta(\omega) \\
 &- \frac{M}{2} [(1 - \delta(\omega_L - \omega_M) - \delta(\omega_M)) 2 \cos \omega_M t - (\phi(\omega_L - \omega_M) - \phi(\omega_L)) 2 \sin \omega_M t] \\
 &+ \frac{M}{2} [(1 - \delta(\omega_L + \omega_M) - \delta(\omega_M)) 2 \cos \omega_M t + (\phi(\omega_L + \omega_M) - \phi(\omega_L)) 2 \sin \omega_M t],
 \end{aligned} \tag{2.15}$$

and further

$$\begin{aligned}
 I_{PD} &\propto 1 - 2\delta(\omega) \\
 &+ M \cos \omega_M t (\delta(\omega_L + \omega_M) - \delta(\omega_L - \omega_M)) \\
 &- M \sin \omega_M t (\phi(\omega_L - \omega_M) + \omega_L + \omega_M) - 2\phi(\omega_L).
 \end{aligned} \tag{2.16}$$

Introducing the derivatives δ' and ϕ'' yields

$$I_{PD} \propto 1 - 2\delta(\omega_L) + 2\omega_M \delta' M \cos \omega_M t - 4\omega_M^2 \phi'' M \sin \omega_M t. \tag{2.17}$$

The first two terms represent the transmitted power, terms two and three are the interferences of the carrier with the sidebands yielding (double-)derivatives of absorption and dispersion respectively. Multiplying I_{PD} electronically with a signal at the modulation frequency (called Local Oscillator) and filtering out frequencies higher than ω_M gives (applying basic trigonometric identities)

$$S_{abs} = I_{PD} \cdot \cos \omega_M t \propto M\omega_M \delta' \tag{2.18}$$

and

$$S_{disp} = I_{PD} \cdot \sin \omega_M t \propto M\omega_M \phi'', \tag{2.19}$$

the absorptive and dispersive signals depending on the phase of the Local Oscillator. These signals describe the deviation from the transition and are thus called *error signals*. When using the S_{abs} signal for stabilization, it must be considered that the phase

modulation causes a residual amplitude modulation, which shifts the zero-crossing of the derivative. In addition, fluctuations of the laser intensity might shift the signal. Consequently, it is difficult to stabilize the laser exactly to the desired transition. In the following section, a technique is presented which overcomes these challenges.

2.3.3. Modulation transfer spectroscopy

Modulation transfer spectroscopy (MTS) uses a nonlinear process in the vapour cell to transfer the sidebands of the modulated pump beam to the probe beam. This is achieved via the third-order susceptibility $\chi_{ijkl}^{(3)}$, which causes a polarization (using index notation)

$$P_i = \chi_{ijkl}^{(3)} E_j E_k E_l \quad (2.20)$$

by three light fields [36, p.312]. The coupling to a fourth field $P_i \cdot E_i$ gives the *four-wave mixing*. In MTS, the nonlinear mixing of the pump beam with $(\omega_L)_{pump}$, $(\omega_L \pm \omega_M)_{pump}$ with the unmodulated probe beam $(\omega_L)_{probe}$ results in the creation of sidebands on the probe beam, $(\omega_L \pm \omega_M)_{probe}$. Because the four-wave mixing process only happens when both beams are resonant with atoms at a certain velocity, resulting in a flat baseline. After detection of the probe beam on a photodiode, a signal in line with equ. 2.17 is obtained. For $\omega_M \leq \Gamma$, both absorptive and dispersive components have a similar lineshape [37].

Compared to FMS, the slopes are steeper and some transitions are enhanced. For instance, the mixing process works better on closed transitions, while other (especially crossover) peaks are suppressed. This is an advantage in case of potassium, since the narrow splitting of the excited state transitions makes it impossible to differentiate them [34]. Depending on the polarization (which is generally circular for MTS), the opposite effect might be achieved [38, p.59].

In conclusion, saturation spectroscopy is a powerful technique that allows the transitions with linewidths below the Doppler width to be resolved. By modulation of either pump or probe beam, an error signal can be generated that specifies the deviation of the laser frequency from the resonance. Both techniques are used in the setup (see sec. 3.2).

2.4. Magneto-optical trap

In section 2.1, the Doppler cooling process, which uses radiation pressure to cool neutral atoms, was explained in one dimension. The resulting damping force leads to lower temperatures. However, the atoms are not captured. To simultaneously cool

and trap atoms at a certain point in space, a magnetic field can be used to perform trapping in addition to the optical Doppler cooling. This is the most common used configuration in laser cooling and known as a *magneto-optical trap*. In this section, the concept is first explained in one spatial dimension and then extended to three dimensions.

2.4.1. 1-dimensional magneto-optical trap

The idea of a magneto-optical trap (MOT) is to use a spatially varying magnetic field to alter the damping force making it position-dependent. The principle is shown in figure 2.7 for a two-level system with a ground state $|g\rangle$ with zero magnetic moment, $F = 0$, and the excited state $|e\rangle$ with $F = 1$, with a Zeeman splitting occurring only in the excited state $|e\rangle$ due to a magnetic field gradient A along z (the magnetic field being $B = Az$). The two laser beams are circular polarized, with opposite polarizations in the laboratory frame. σ^+ -polarized light propagating from the left excites atoms to the $|e, m_F = +1\rangle$ state (the blue line). Considering the detuning of the laser beams with frequency ω_L , atoms at $z \leq 0$ are pushed towards the center. For $z > 0$, the force gets weak due to the larger detuning. There, the σ^- -beam is less detuned and pushes the atoms towards the center. Close to $z = 0$, the overall radiation pressure force is smaller, so the atoms are trapped around $z = 0$ [22, pp. 156–157].

In the frame of a photon moving towards the center, the magnetic field decreases. A photon with σ^+ polarization, whose spin is pointing towards the center (antiparallel to the magnetic field), will excite the atom to the Zeeman substate with decreased energy. Photons that passed through the center moving outwards, have their spin parallel with the magnetic field, exciting to the Zeeman substate with increased energy, which is further detuned and therefore unlikely. The polarization in the frame of the laser beam is the same for both beams.

The additional detuning caused by the Zeeman splitting field is $\pm\mu'B/\hbar$, with the effective magnetic moment $\mu' = (g_e m_e - g_g m_g)\mu_B$ (g_g and g_e are the Landé factors of the ground respectively excited state, m_g and m_e are the magnetic quantum numbers, and μ_B is the Bohr magneton). The resulting force is

$$\vec{\mathbf{F}} = -\beta\vec{\mathbf{v}} - \kappa\vec{\mathbf{r}}, \quad (2.21)$$

with the spring constant $\kappa = \frac{\mu'A}{\hbar k}\beta$. This is a damped harmonic oscillator with frequencies $\sqrt{\frac{\kappa}{m}}$ and damping coefficient $\frac{\beta}{m}$. The damping coefficient is usually larger than the frequency, thus the system is overdamped [22, p. 158].

In the damped harmonic oscillator model, potential and kinetic energy are ex-

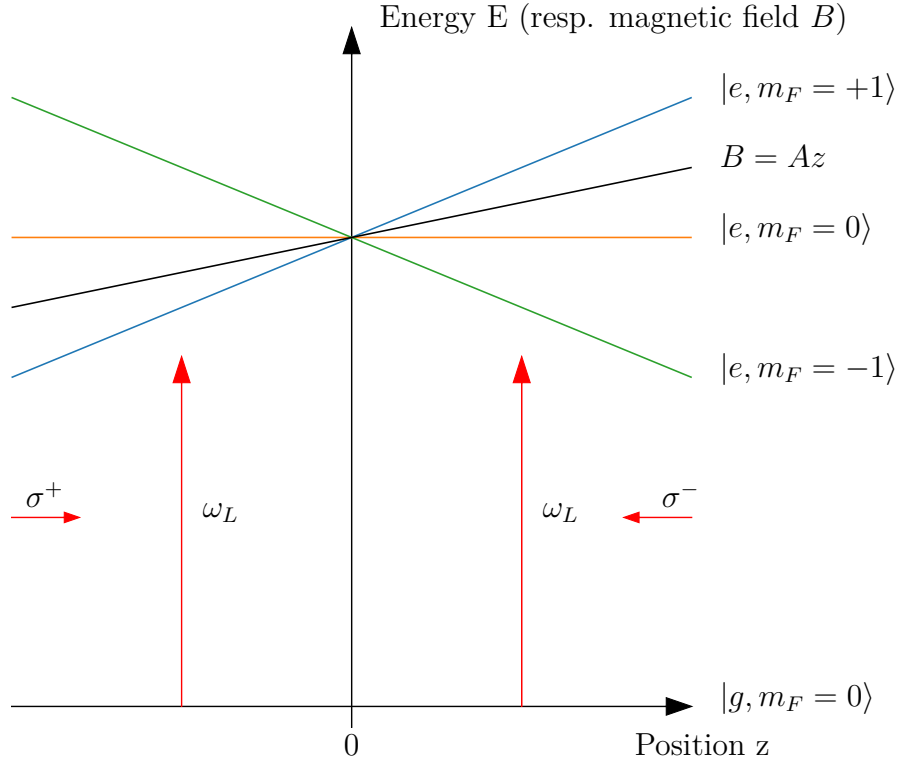


Figure 2.7.: The principle of a magneto-optical trap in one dimension: a magnetic field gradient (black) causes a Zeeman splitting in the excited state. With circularly polarized light, a spatially varying detuning is present, leading to a position-dependent force: the σ^+ -beam on the left-hand side is closer to resonance for $z < 0$, exciting the atoms to the $|e, m_F = +1\rangle$ state, while for $z > 0$ it is further detuned from resonance, so the force gets weaker. The same applies for the σ^- -beam and $|e, m_F = -1\rangle$, finally the atoms are trapped around the zero of the magnetic field.

changed periodically. Assuming the energy for the oscillation is $E = k_B T$ [21, p. 268], one can give an estimate of the size Δz and velocity spread Δv of the MOT:

$$k_B T = m(\Delta v)^2 = \kappa(\Delta z)^2. \quad (2.22)$$

m and κ are mass of an atom and the spring constant of the MOT respectively. For ^{39}K atoms at the Doppler temperature, the size of the MOT is estimated about 0.1 mm at a gradient $A = 10 \text{ G cm}^{-1}$ (for $\delta = -\Gamma$), Δv is approximately 20 cm s^{-1} [22, p. 159].

2.4.2. 3-dimensional MOT

To extend the scheme of a magneto-optical trap to three spatial dimensions, six laser beams are used (as in fig. 2.9) and magnetic field gradients in three dimensions are needed. From Maxwell's equations, it follows that the magnetic flux Φ through the surface \vec{S} of the MOT volume V (which is defined by the sphere formed by the six overlapping beams) $\Phi = \oint \vec{B} \cdot d\vec{S} = \int \nabla \cdot \vec{B} dV$ is conserved [39, p.86]. Consequently, it is not possible to provide the same magnetic field gradient along all three dimensions. Creating a magnetic field with a positive gradient on the x and y -axis and a negative, twice as large gradient on the z -axis

$$\vec{B} = A \begin{pmatrix} x \\ y \\ -2z \end{pmatrix}, \quad (2.23)$$

with magnetic field gradient A , is possible. This can be achieved using the *anti-Helmholtz configuration* (two coils of radius R at a distance R with currents flowing in opposite directions) shown in figure 2.9. The resulting magnetic field is a *quadrupole field* (its name stemming from the four poles observed in the cross section of the magnetic field) plotted in fig. 2.8a [26, pp.62–63], [39, pp.92–93], [22, pp.157–158].

The magnetic field gradient on the z -axis requires a different polarization on the two beams along z -axis since it has a negative gradient. In figure 2.9, the polarizations are given relative to the propagation direction of each laser beam. In this description, both beams would have σ^+ polarization in the one-dimensional case described above. Since the magnetic field is now pointing towards the center in z -direction, the polarization has to point outwards to excite the Zeeman substate closer to resonance, and is therefore σ^- .

For now, an atom with a $|F = 0\rangle$ ground state and an $|F = 1\rangle$ excited state is assumed. Real atoms might have more complex level structures, e.g. the cooling transition of potassium is $|F = 2\rangle$ to $|F = 3\rangle$. Considering the selection rules, each of the five $|F = 2, m_F = n\rangle$ ground states ($n = \pm 2, \pm 1, 0$) together with the respective three excited states $|F = 3, m_F = n - 1\rangle$, $|F = 3, m_F = n\rangle$ and $|F = 3, m_F = n + 1\rangle$ corresponds to the simplified case described above. Since the spontaneous decays are not restricted to one σ -transition, atoms can make transitions between the different m_F ground states. Atoms mainly interacting with σ^+ (σ^-)-polarized light can only increase (decrease) their m_F quantum number and will end up in the $m_F = +2$ ($m_F = -2$) state [22, pp.157–158].

In addition, the repumping light is more important for laser cooling potassium than for other alkali metals, as described in section 2.2.

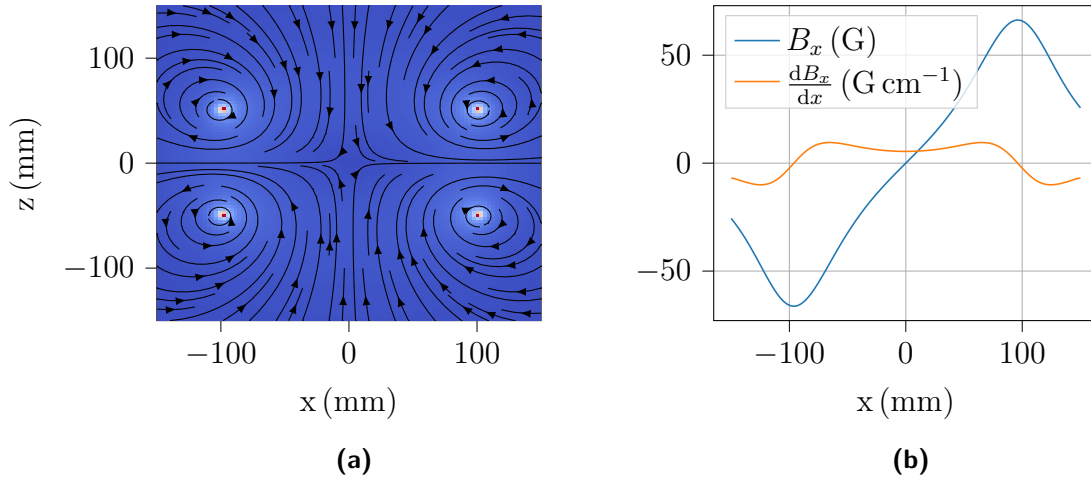


Figure 2.8.: (a) The cross section of the magnetic field resulting from the anti-Helmholtz configuration (two coils of radius $R = 100$ mm with their axis in z -direction are at a distance of R): the field is pointing towards the origin on the z -axis, and outwards on x - and y -axis (because of the cylindrical symmetry, the magnetic field is the same in x - and y -direction), so the magnetic flux is conserved. The coil current is 10 A for 100 windings. (b) Magnetic field and gradient on the x -axis ($y = z = 0$) for the magnetic field from 2.8a. The field gradient is 5.4 G cm^{-1} , which is a typical value for a MOT [40, p.42]. Along the z -direction the gradient is negative and twice as steep.

2.4.3. Single-beam magneto-optical trap

There are a few attempts towards minituarization of magneto-optical traps. Using only one laser beam, one can save laser power and the setup is more stable in terms of the alignment of the beam.

The most notable is the *pyramidal MOT*. The idea is shown in figure 2.10: a mirror with a concave pyramidal structure works as a retroreflector, so light that enters is reflected twice and returns in the exact direction which it came from. After the first reflection, the beam propagates along the x -direction, creating two beams along the x -axis. The same happens along the y -axis, resulting in six “effective” beams. Now, one has to check whether this setup can produce the desired polarizations. Again, the polarizations are defined with respect to the propagation direction of each laser beam. For the anti-Helmholtz coils above (again aligned along the z -axis), σ^- -polarization is needed in z -direction. With each reflection, σ^- -polarization is changed to σ^+ and vice-versa. This can be easily checked by projecting the direction of rotation of the incident and reflected beam onto the reflecting surface. It follows that the “effective beams” in x - and y -direction have the required σ^+ -polarization [41].

The pyramidal MOT simplifies the setup and alignment. However, the atoms are

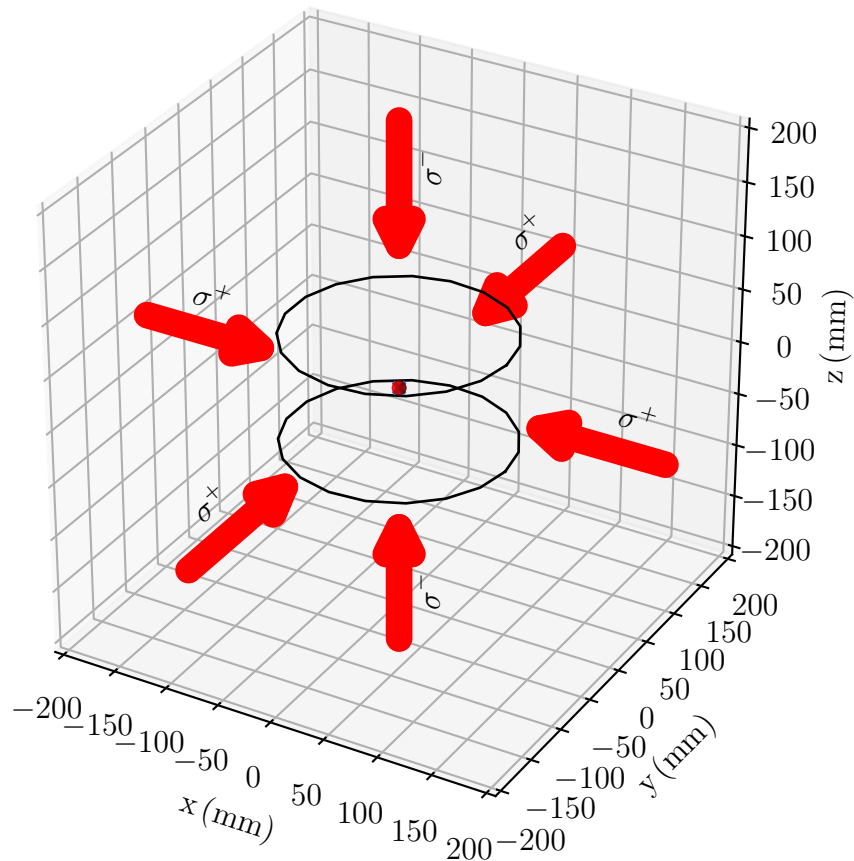


Figure 2.9.: The 3-dimensional magneto-optical trap: six laser beams are used for Doppler cooling in all spatial dimensions. A pair of anti-Helmholtz coils with radius $R = 100$ mm at a distance R along z produce magnetic field gradients along all three dimensions. The polarization of each beam is given relative to its propagation direction. In the radial direction (on the x and y -axis), the magnetic field is pointing outwards from the origin, so the photon spin has to point inwards to excite the excited state with lower energy (the Zeeman shift is $\propto \vec{\mu} \cdot \vec{B}$ and the photon spin is transferred to the magnetic moment $\vec{\mu}$ of the atom), which is closer to resonance with the red-detuned laser beam (cf. fig 2.7). The magnetic field in the z -direction is pointing inwards (cf. fig. 2.8a), therefore the polarization is σ_- . The red sphere in the middle represents the cloud of trapped atoms, its radius is typically less than a millimeter.

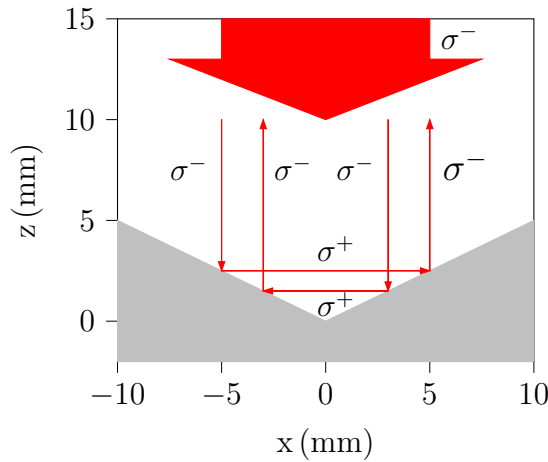


Figure 2.10.: The pyramidal MOT. A single beam is reflected on a mirror with a pyramid-shaped hole. The beam is reflected twice, propagating along the x -direction (and analogously the y -direction) in between, resulting in effectively six beams. Because the mirror is retro-reflecting (angled incident beams are reflected in the very direction they came from), a slight misalignment of the laser beam does not significantly affect the MOT. At the reflection, the polarization (defined with respect to the propagation direction of each beam) changes from σ^- to σ^+ and vice-versa, giving the polarizations needed for a MOT with anti-Helmholtz coils along z -direction.

trapped inside the pyramidal shape, which limits the optical access e.g. for imaging. There are other variants of single-beam MOTs, for instance using a grating that creates the additional beams by reflection. It should also be mentioned that only four beams are strictly necessary to form a MOT, known as *tetrahedral MOT* [42], [43].

To sum up, a quadrupole magnetic field creates a Zeeman splitting that can be used to trap atoms by making the Doppler cooling force position-dependent when the laser beams are circularly polarized. The magnetic field can be generated by a pair of coils with opposite current flow, called the *anti-Helmholtz configuration*. Finally, it is possible to create a MOT with only one beam by using concave pyramidal mirrors that reflect parts of the beam to generate six beams, thereby simplifying the alignment and saving laser power.

2.5. MOT loading

In the previous section it was shown how to cool atoms and trap them in a magneto-optical trap. This has to be done in vacuum to prevent external influence on the atoms. There are different techniques for bringing atoms into the MOT volume where

they can be finally trapped. Several techniques will be presented and discussed in this section.

2.5.1. Loading from background gas

One possible source of atoms is to use the solid state of the element. At room temperature, some atoms can leave the solid state giving a partial vapour pressure of 1.3×10^{-8} mbar for potassium [23]. By heating up the metallic sample, the vapour pressure increases and can thus be controlled. The easiest way to load a MOT is by using the vapour pressure in the vacuum chamber caused by the background gas. At temperature T , the atoms have velocities according to the Maxwell-Boltzmann distribution, resulting in the density n of atoms with velocities between v and $v + dv$ [21, p.195]

$$n(v)dv = N \cdot \left(\frac{m}{2\pi k_B T} \right)^{3/2} \cdot 4\pi v^2 \cdot \exp\left\{ -\frac{mv^2}{2k_B T} \right\} dv, \quad (2.24)$$

with atomic mass m . The most probable speed v_p (derived by maximizing $n(v)$) is about 350 m s^{-1} for ^{39}K at room temperature ($v_p = \sqrt{\frac{2k_B T}{m}}$, [21, p.196]).

The maximum velocity at which atoms can be trapped in a MOT, called capture velocity v_c , can be estimated by requiring that an atom of velocity v has to lose its kinetic energy E_{kin} when passing through the MOT beams, which overlap on a sphere of radius z' . Assuming large beam powers (where the saturation parameter $s_0 \rightarrow \infty$), the Doppler cooling force (equ. 2.3) can be assumed to be the maximum possible $F_{max} = \hbar k \Gamma / 2$. For the atom to be captured, it is required that

$$E_{kin} = 2z' \cdot F_{max}. \quad (2.25)$$

This gives a capture velocity

$$v_{cap} = \sqrt{\frac{2z' \hbar k \Gamma}{m}}. \quad (2.26)$$

For beam diameters of 20 mm, v_c is around 100 m s^{-1} .

The loading of a MOT is described by

$$N(t) = N_0 \left(1 - e^{-\frac{t}{\tau}} \right). \quad (2.27)$$

The atom number $N(t)$ increases until the steady state number N_0 is reached at $t = \infty$. The loading rate τ is the inverse loss rate due to collisions of the trapped atoms with

atoms from the background gas (^{39}K atoms and other residual atoms). The mean free path in the background gas is [24, p.27]

$$l = \frac{1}{\sqrt{2}n\sigma} = \frac{k_B T}{\sqrt{2}p\sigma} \quad (2.28)$$

where n is the density, p the pressure and σ the cross section of the atoms, which can be approximated with a hard sphere model [24, pp.27, 109] as $\sigma = \pi(2a_B \frac{n^2}{Z})^2$ with the Bohr radius a_B , the main quantum number n and the atomic number Z ($n = 4$ and $Z = 19$ for potassium). The velocity of the atoms divided by the mean free path gives the loading/loss rate of the MOT

$$\frac{1}{\tau} = \frac{v_K}{l_K} + \frac{v_{nonK}}{l_{nonK}}, \quad (2.29)$$

where contributions from potassium (K) and residual ($nonK$) atoms are considered.

The atom number in equilibrium N_0 can be written as (with the MOT surface area S of the MOT volume and the mean velocity of the Boltzmann distribution $v_{avg} = \sqrt{\frac{8k_B T}{\pi m}}$, [21, p.196])

$$N_0 = 0.1 \frac{S}{\sigma_K} \left(\frac{v_c}{v_{avg}} \right)^4 \quad (2.30)$$

when the K background pressure is much larger than the pressure by the caused by the residual atoms.

When the background pressure of the non-potassium atoms is low, the loading rate is proportional to the background pressure (this is not true for higher MOT densities, where *reradiation* has effects, see section 2.6.1. At a pressure of 10^{-8} mbar, the loading rate of potassium is ≈ 200 s. Heating up the metallic sample to its melting point at 336.8 K gives a vapour pressure of more than 10^{-6} mbar allows for loading times of ≈ 3 s. In practice, the loading is stopped when only a fraction of the $N_0 \sim 10^{12}$ atoms is loaded, leading to shorter effective loading times. When performing experiments, collisions with other atoms are unwanted systematic effects. Low vapour pressures imply long loading times though, which leads to one run of the experiment taking minutes. Fast repetition rates facilitate the alignment of optical components, magnetic fields etc. A few techniques that have been developed to shorten loading times while keeping ultra high vacuum in the experiment chamber are presented in the following subsections [44].

2.5.2. Zeeman slower

A *Zeeman slower* is used to create cold atomic beams [45]. A collimated beam exits an oven and is then cooled by a counterpropagating beam. During the cooling, the atoms slow down and lose resonance with the laser beam, requiring the adjustment of the laser frequency. This is possible when creating only pulses of atoms (called *chirped cooling*). Alternatively, the atoms can stay on resonance using a magnetic field gradient that produces Zeeman shifts, thus the name *Zeeman slower*. The atoms leave the oven attached to a tube (which is about 50 cm long) with coils generating the magnetic field. When entering the latter, those with a certain velocity v_0 are in resonance and are subsequently cooled down. Slower atoms are moving unaffected until they are on resonance and are slowed down afterwards. Therefore, atoms with speed $v < v_0$ are cooled down into one velocity group with speeds as low as 10 m s^{-1} (this was achieved for ^{87}Rb ; for potassium, the velocity would be higher due to the smaller mass). The presence of a magnetic field has another advantage: it creates a cycling transition. In case of ^{39}K , this would be the $|F = 2, m_F = +2\rangle$ to $|F' = 3, m_F = +3\rangle$ excitation (for σ_+ light). Because of the circularly polarized light, atoms excited to $|F' = 3, m_F = +3\rangle$ can only decay back to $|F = 2, m_F = +2\rangle$ and are therefore in a closed cooling cycle without the need of a repumper [45], [46].

When the collimated beam leaves the oven, it can pass through a small tube acting as a *differential pumping stage* [47]. In this manner, a pressure difference can be maintained between the oven and the remaining vacuum system. Both sides of the differential pumping stage can have vacuum pumps to sustain the desired pressure difference. The lower vacuum on the MOT side results in fewer atom losses and the lower atom velocity facilitates the capturing. However, although Zeeman slowers can produce beams with low longitudinal speed, the transversal velocity components cause the beam diameter to increase when passing through the 50 cm long magnetic field gradient, indicating the need for additional transverse cooling.

2.5.3. The low velocity intense source

Another approach to the problem posed in section 2.5.1, namely that high loading rates imply low MOT lifetimes, is to use a double-MOT system: the first MOT is loaded from background gas, and the atoms are then transferred through a differential pumping stage to the second MOT, which operates at low pressure with long lifetimes.

One particular setup is the *Low Velocity Intense Source* (LVIS, [48]). The setup is the same as for a MOT, except for one beam, which has a dark spot (zero intensity) in the middle so the atoms can exit towards the second MOT. The dark spot is achieved

by reflecting the beam from a mirror with a hole in its center. In *continuous mode*, the atoms are trapped in the LVIS and can continuously exit towards the MOT. In *pulsed mode*, a plug beam is shone sideways in the beam with the dark spot, keeping the atoms from exiting. After the LVIS is loaded, the plug beam is turned off and the second MOT is loaded. With this method, continuous beams with 1×10^9 atoms per second and pulsed beams with a flux of $1 \times 10^{10} \text{ s}^{-1}$ are achieved. Due to the dark spot in one beam, the atoms are cooled less in the forward direction, resulting in longitudinal velocities of around 14 m s^{-1} for ^{87}Rb atoms. Again, for potassium, one expects higher velocities because of the lower mass. The divergence of the beams is less than 50 mrad , corresponding to a temperature of a few mK [48].

2.5.4. 2D MOT

A different method to generate atomic beams is the *2D MOT* [49], where the atoms are cooled and trapped only in transversal directions. The principle is shown in figure 2.11: two pairs of rectangular anti-Helmholtz coils are aligned such that they compensate each other along the z -axis (the rectangular shape enables to create magnetic fields gradients more efficiently for the rectangular geometry of the 2D MOT). Four laser beams are used for transversal cooling. In the easiest configuration, there are no longitudinal beams. Through a small hole (indicated by the gray mirror at $z = +100$), which has a diameter on the order of a mm, atoms can exit towards the 3D MOT. In order to leave through the hole, the atoms' transversal temperature must be lowered sufficiently when passing through the beams. This filters out atoms with higher longitudinal velocity, since they scatter fewer photons. In practice, the beams are shaped elliptically, which extends the interaction times with the light [50]. An atomic beam is formed along the z -axis leading to the exit, whose atomic flux is roughly proportional to the vapour pressure. For ^{39}K , loading rates of 1×10^9 atoms/s can be achieved ([51]). It was reported that 2D MOTs have loading rates comparable to a LVIS, however, much less laser power is needed. One drawback of the 2D MOT is that atoms can exit on both sides along the z -axis, and thus half of them are lost [50].

2D+ MOT

To prevent atoms from escaping in the wrong direction, an additional beam, called *push beam* can be used [50]. It also pushes the atoms towards the exit leading to the 3D MOT, hence the name. A counter-propagating beam (CP beam), which is retroreflected by a mirror with a hole leading to the 3D MOT, can be further used to recycle atoms which fail to hit the outlet and to reduce the longitudinal velocity of the formed

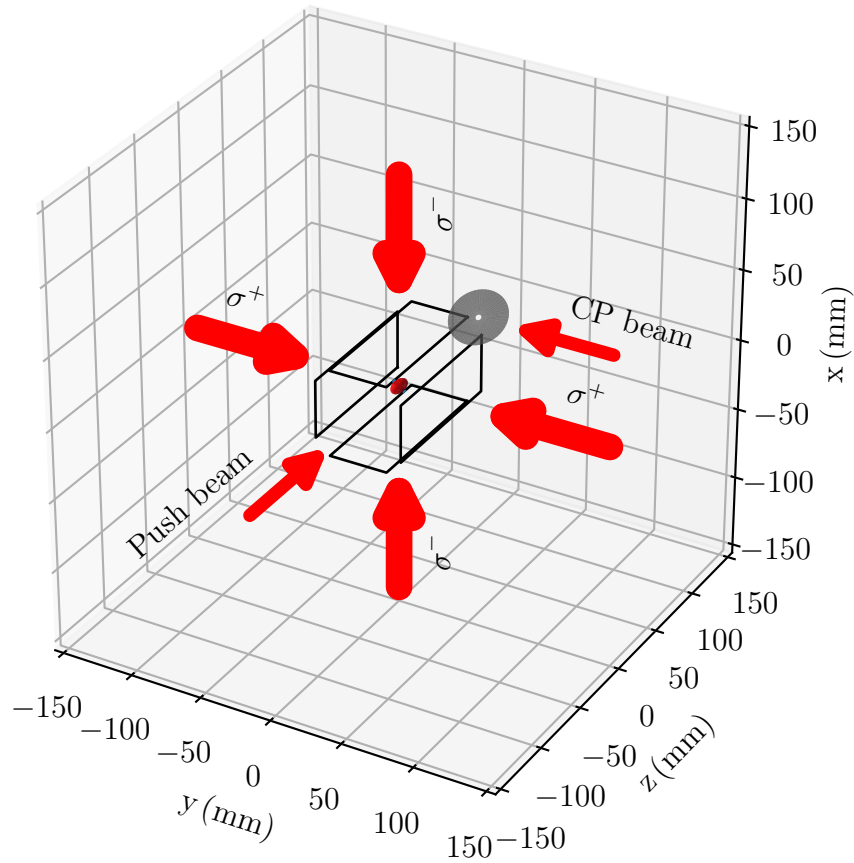


Figure 2.11.: The 2-dimensional magneto-optical trap: two pairs of anti-Helmholtz coils are used to eliminate the magnetic field along the z -axis. Transversal elliptically shaped beams cool the atoms in the x - and y -directions to form an atomic beam. The atoms can leave the 2D MOT through an aperture (on the gray mirror at $z = 100$ mm). To prevent atoms from leaving in $-z$ -direction, a *push beam* is used. Together with a *counterpropagating beam* (CP beam), which cools the beam in longitudinal direction and recaptures atoms that did not hit the exit hole, they form a $2D+$ MOT.

atom beam. This setup is called *2D+ MOT*. Both push and CP beam are smaller in diameter compared to the MOT beams, as indicated in the drawing (fig. 2.11). The optimal detunings of those beams might be different, some experiments only use either repumping or cooling light. For potassium, fluxes up to 1×10^{11} atoms/s with longitudinal velocities of around 30 m s^{-1} have been reported [52].

Tilted 2D MOT

The *Tilted 2D MOT* [53] is an approach to realise a 2D+ MOT without the need for two additional beams. The two beams along x - and y -axis are tilted slightly with respect to the z -axis, therefore emulating push- and CP-beam. The optimum tilting angle was reported to be 4° , loading rates of nearly 1×10^{10} atoms/s were achieved with low laser power.

2.5.5. Pyramidal LVIS

It should also be mentioned that analogous to the pyramidal MOT, concepts to simplify the setup and alignment using pyramidal shapes with a hole to form a LVIS have been implemented with a flux of 1×10^9 atoms/s [54], [55]. However, for technical reasons that are explained in the experimental part of this thesis, the one-beam setups are not a suitable option (see sec. 3.3).

2.5.6. Conclusion

To sum up, loading a magneto-optical trap from the background gas is not a viable option because neither high loss rates nor long MOT loading times are acceptable for the planned experiment. Zeeman slower are rather large in size (the length of the magnetic field is typically 50 cm), while a MOT as an atom source is more compact and those more suitable. From a technical point of view, the LVIS has been superseded by the 2D MOT, which is the most commonly used option nowadays. Because it can be easily improved by either tilting the beams or adding additional beams to form a 2D+ MOT in case higher loading rates are needed, it constitutes a reasonable solution and was thus chosen for the setup presented in this thesis.

2.6. Compressing the MOT

After the MOT is loaded, the atomic cloud can be compressed by the subsequent methods, facilitating the loading of the atoms into a magnetic or optical trap. In addition, the lower intensities and larger detunings simplify the transition to cooling mechanisms that reach temperatures below the Doppler cooling limit.

2.6.1. CMOT

As outlined in section 2.4.1, atoms in the MOT are trapped by a magnetic field gradient A , which causes a position-dependent Zeeman splitting, resulting in a harmonic oscillator potential with spring constant $\kappa \propto A$. There are two limiting factors on the density that have to be considered. Firstly, the thermal energy of the atoms counteracts the trapping force

$$\frac{1}{2}k_B T = \frac{1}{2}\kappa(\Delta z)^2 \quad (2.31)$$

in each spatial dimension, leading to the peak density $n_p \propto N \left(\frac{\kappa}{k_B T}\right)^{3/2}$. Secondly, photons emitted from atoms in the cloud might be absorbed by other atoms, which is called *reradiation*. If the resulting force is in equilibrium with the trapping force, the reradiation density limit is given by $n_r \propto \frac{\kappa}{I}$, I being the intensity of the cooling light. Both limits depend on κ and thus on the magnetic field gradient. By increasing A the MOT can be compressed, hence the name *compressed MOT* (CMOT). The reradiation can be also reduced by decreasing the intensity and increasing the detuning. Axial MOT gradients of 10 G cm^{-1} as well as the detuning are ramped up (to 60 G cm^{-1} and 7Γ in [56] for ^{85}Rb), leading to densities of $1 \times 10^{11} \text{ atoms/cm}^3$, an order of magnitude higher than in a MOT. The shape of the CMOT is Gaussian (which is not strictly the case for a MOT), though for even higher gradients, a diffuse shape can appear outside of the Gaussian. This might be attributed to sub-Doppler cooling forces (see section 2.7) which are active in the center at low magnetic field, while outside the Doppler cooling force is still significant [56].

For potassium, similar gradients and detunings are used [30, p.78] and the suspected sub-Doppler cooling forces can be enhanced by adding light from the D1 transition which is needed for the gray molasses cooling described in section 2.7.2 [19].

2.6.2. Dark SPOT

As mentioned above, reducing the intensity of the cooling light helps to increase the density of the MOT. To further reduce the radiation pressure, the repumper can be turned off. Consequently, atoms that decay back to the lower ground state ($|F = 1\rangle$ for potassium) are out of resonance and therefore *dark*. Instead of turning the repumper off (or reducing its intensity), repumping beams with a dark spot (therefore *dark SPOT*, which also stands for *spontaneous-force optical trap*, a general concept that includes the MOT, [57]) in the middle can be used. The overlapping beams form a dark sphere in the center of the MOT. Faster atoms, which move out of this region, are recaptured by the repumper beams before they leave the MOT. With this concept, densities of 1×10^{12} atoms/cm³ could be achieved for sodium atoms. The hyperfine splitting of the ground state of alkali atoms impacts the dark SPOT, since for a higher splitting fewer atoms decay to the lower ground state. Using a *depumping beam*, this can be done in a controlled way and large splittings are therefore advantageous [58].

Because the setup with the dark spot in the repumping beams is rather complicated (in [58], the repumping light was sent to the MOT in two extra beams). It is easier to reduce the repumping light, which is also used in potassium experiments ([30, p.75], the second phase of the CMOT cooling stage).

2.7. Sub-Doppler cooling

In section 2.1, the Doppler cooling limit was introduced. However, in experiments even lower temperatures are achieved [59]. This led to theoretical models being developed to explain these surprising results. While the Doppler cooling force relies on a two-level system, the explanation of the mechanisms shown below consider the fact that real atoms have magnetic sublevels leading to further cooling forces [60].

The Doppler temperature of potassium is 145 μ K. Because sub-Doppler cooling is also based on spontaneous emission, the recoil of the last emitted photon with wave vector k gives the minimal temperature T_{rec} for an atom with mass m , called *recoil temperature*,

$$T_{rec} = \frac{(\hbar k)^2}{2k_B m} \quad (2.32)$$

which is about 0.4 μ K for ³⁹K and ⁴¹K. Consequently, much lower temperatures can be reached, which is needed to do precision measurements or as a further step towards the formation of Bose-Einstein condensates.

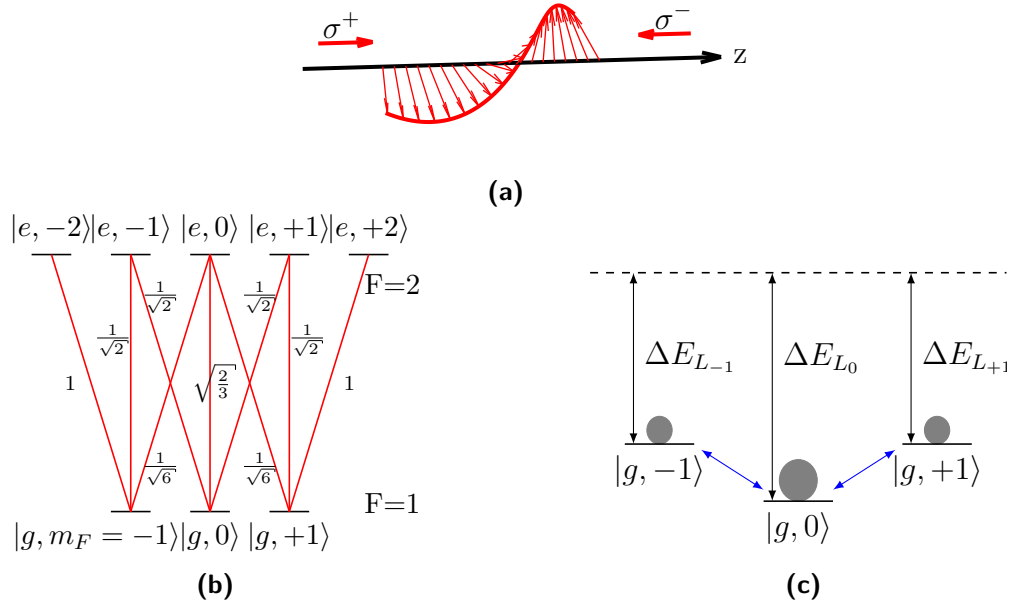


Figure 2.12.: Polarization gradient cooling with circular polarization: (a) The polarizations of the two laser beams. Together, they give a linear polarization that rotates around z . (b) The magnetic substates with the Clebsch-Gordan coefficients for a $F = 1$ to $F = 2$ transition. For the $|g, \mp 1\rangle$ states, the coefficients differ by a factor six between σ^+ and σ^- beams. Therefore, a motion-induced imbalance between the two state causes a slowing force. (c) The light shifts of the ground states, which are different due to the Clebsch-Gordan coefficients for the π -transitions. The gray spheres denote the atom distribution in the steady state, with $9/17$ in $|g, 0\rangle$ and $4/17$ in each $|g, \pm 1\rangle$ state. If an atom moves fast enough so it cannot follow the polarization of the light, it experiences a magnetic field along z that introduces a coupling between the ground states, denoted by the blue arrows. This results in a population imbalance between the $|g, \pm 1\rangle$ ground states.

2.7.1. Polarization gradient cooling with circularly polarized light

While sub-Doppler cooling was first observed in optical molasses with linearly polarized light [59], magneto-optical traps require circular polarizations. Therefore, the following cooling scheme uses circular polarization. It is limited to cooling in one dimension, where theoretical explanations are available without the need for numerical calculations.

The spatial part of the electrical field of the σ^+ and σ^- light with equal powers propagating along z (as shown in figure 2.12a) with wave vector k can be written as

$$\vec{\mathbf{E}}(z) \propto \vec{\epsilon}^+ e^{ikz} + \vec{\epsilon}^- e^{-ikz} \quad (2.33)$$

where ϵ^+ and ϵ^- are the polarization vectors of the laser beams moving in $+z$ and $-z$ directions respectively. They can be written in terms of x and y -components $\vec{\epsilon}_x$ and $\vec{\epsilon}_y$:

$$\begin{aligned}\vec{\epsilon}^+ &\propto -(\vec{\epsilon}_x + i\vec{\epsilon}_y) \\ \vec{\epsilon}^- &\propto \vec{\epsilon}_x - i\vec{\epsilon}_y,\end{aligned}\tag{2.34}$$

giving

$$\vec{\mathbf{E}}(z) \propto \vec{\epsilon}_x \sin kz + \vec{\epsilon}_y \cos kz.\tag{2.35}$$

This is a linear polarization that rotates along the z -axis forming a helix, as shown in figure 2.12a. The polarization changes in space, forming a *polarization gradient*. The level system considered (see fig. 2.12b) is the simplest possible, formed by a $F = 1$ to $F' = 2$ transition, but works for higher F too. The number beside the transition lines indicate the relative transition strength, also called *Clebsch-Gordan coefficients* [22, pp.50–56] These lead to different populations between the ground states. $|g, 0\rangle$ contains 9/17 of the population, while the $|g, \pm 1\rangle$ contain each 4/17.

An important effect for sub-Doppler cooling is the *light shift*. It is an AC Stark shift caused by the electromagnetic field of the wave, resulting in shifts of [22, pp.8, 25]

$$\Delta E_L = \frac{\hbar\Omega^2}{4\delta}\tag{2.36}$$

in the low-intensity limit ($\Omega \ll |\delta|$) for the ground state (the excited state is shifted with $-\Delta E_L$). Ω is the *Rabi frequency*, which is the inverse of the time a two-level system needs to be excited to its excited state and driven back by stimulated emission when driven by a laser field. It is related to the saturation parameter s_0 (see section 2.1) by $s_0 = 2\Omega^2/\Gamma^2$. Γ and δ are the natural linewidth of the transition and the detuning of the laser to the transition frequency respectively.

The different Clebsch-Gordan coefficients of the π -transitions in fig. 2.12b form the level scheme in fig. 2.12c. It is required that the light shift is much larger than Γ , so the splitting between the ground states is considerable. Now consider an atom moving in $+z$ -direction with speed v . At a velocity close to $v = 0$, it can adiabatically follow the rotation of the light field polarization. If it is faster however, because of the *nonadiabaticity*, the preferred orientation of the atom is different from the polarization of the light field. In the reference frame of the atom, the light field resembles a magnetic field along z , with a Larmor frequency $\propto kv$. This introduces a coupling between the ground states (the blue arrow in fig. 2.12c) limited by the energy splitting between the $|g, \pm 1\rangle$ and $|g, 0\rangle$ states with energies $\Delta E_{L_{\pm 1}}$ and ΔE_{L_0} , pumping the atom towards

the $|g, -1\rangle$ state. For $v > 0$, this leads to a population difference

$$\Pi_{-1} - \Pi_{+1} = \frac{kv}{\Delta E_{L_{\pm 1}} - \Delta E_{L_0}}. \quad (2.37)$$

between $|g, -1\rangle$ and $|g, +1\rangle$ with populations Π_{-1} and Π_{+1} . Because in $|g, -1\rangle$ the Clebsch-Gordan coefficients are different for σ^+ and σ^- , more counterpropagating σ^- photons are scattered (the atom being excited to $|e, -2\rangle$ and decaying back) and thus slowed down.

To calculate the force, the population difference from equ. 2.37 caused by the ground state coupling is multiplied with the scattering rate

$$\gamma = \frac{\Omega^2}{\delta^2} \Gamma. \quad (2.38)$$

For each scattering process, the atomic momentum is reduced by $\hbar k$, thus giving a force

$$F_P \propto \hbar k^2 \frac{\Gamma}{\delta} v. \quad (2.39)$$

As in case of the Doppler cooling force, it is proportional to the velocity, damping the atoms. However, it does not depend on the light intensity, although the capture range does (and we required the intensity to be low). The velocity v is assumed to be small, since for larger velocities Doppler cooling becomes the dominant process. The temperature limit is T_{rec} , but extending the semiclassical treatment here with quantized momenta, temperatures below T_{rec} are theoretically possible in one dimension [61].

In real atoms, the situation is more complex. Atoms have more sublevels ($F = 2$ and $F' = 3$ for ^{39}K and ^{41}K), there is a second hyperfine ground state which might need repumping, and the polarizations are more complicated in three dimensions. Because the beams overlap, linear polarizations might play a role, leading to *Sisyphus cooling* [61], a different sub-Doppler cooling mechanism. With potassium, the narrow excited state manifold makes the hyperfine pumping (atoms are decaying back to the $F = 1$ state) more impactful. This can also be of advantage, as with low or no repumping light, $F = 1$ is a dark state, which limits the reradiation (the number of atoms leaving the trap can be controlled by setting the intensity of the repumping light), as discussed in section 2.6.2 [62].

In [62], a strategy for sub-Doppler cooling with potassium is explained. After the CMOT phase, the repumping light is reduced to 1/100 of the intensity of the cooling light. The detuning of the latter is set to 0.5Γ , and 10 ms later the intensity is reduced to zero while the detuning is increased to about 2.5Γ . Temperatures of $25(3)\ \mu\text{K}$ and $47(5)\ \mu\text{K}$ have been reached for ^{39}K and ^{41}K respectively, well below the Doppler limit

of 145 μK .

In conclusion, polarization gradient cooling with σ -polarized light uses the *non-adiabatic* movement of atoms through a light field with rotating linear polarization to produce population differences between ground states so the atoms perceive a damping force. This damping force is independent of the light intensity (which is required to be low), but the capture velocity depends on the intensity. For potassium, the narrow hyperfine splitting degrades the effectiveness of this cooling mechanism, however, schemes exist which make it possible to reach sub-Doppler temperatures.

2.7.2. Gray molasses cooling

The problem of the narrow hyperfine splitting in the excited state of the D2 lines of ^{39}K and ^{41}K can be overcome by using the D1 line instead (see fig. 2.2). The transition from $F = 2$ to $F' = 2$ allows for *gray molasses cooling*, a technique that combines *velocity-selective coherent population trapping* (VSCPT, [63]) and a nonadiabatic force.

Velocity-selective coherent population trapping

Consider a $F = 1$ to $F' = 1$ transition as shown in figure 2.13a. In addition to the electronic state, the momentum p of the atom in one dimension (along z) is quantized and written in units of $\hbar k$, k being the wave vector of the cooling light. Using the same laser beam configuration as in fig. 2.12a, $|g, m_F = -1, p = -1\rangle$, $|g, +1, +1\rangle$ and $|e, 0, 0\rangle$ form an effective Λ -system. This can be understood by considering that atoms residing in $|g, 0, 0\rangle$ are pumped to $|e, \pm 1\rangle$ and partly decay into $|g, \pm 1\rangle$, which depumps the $|g, 0\rangle$ level over time. The coupling of the two ground states via the excited state results in the formation of the stationary states

$$|\pm\rangle = |\pm, m_F = 0, p = 0\rangle = \frac{1}{\sqrt{2}} (|g, -1, -1\rangle \pm |g, +1, +1\rangle) \quad (2.40)$$

The electric dipole matrix element of those states with $|e, 0, 0\rangle$ is

$$\langle e, 0, 0 | \vec{\mathbf{d}} | \pm \rangle = \langle e, 0, 0 | \vec{\mathbf{d}} | g, -1, -1 \rangle \pm \langle e, 0, 0 | \vec{\mathbf{d}} | g, +1, +1 \rangle, \quad (2.41)$$

with the dipole moment operator $\vec{\mathbf{d}}$. The momentum of the atom has no effect on the matrix element, and the magnetic quantum number causes a -1 for the first term (due to the Clebsch-Gordan coefficients), giving

$$\langle e, 0, 0 | \vec{\mathbf{d}} | + \rangle = 0. \quad (2.42)$$

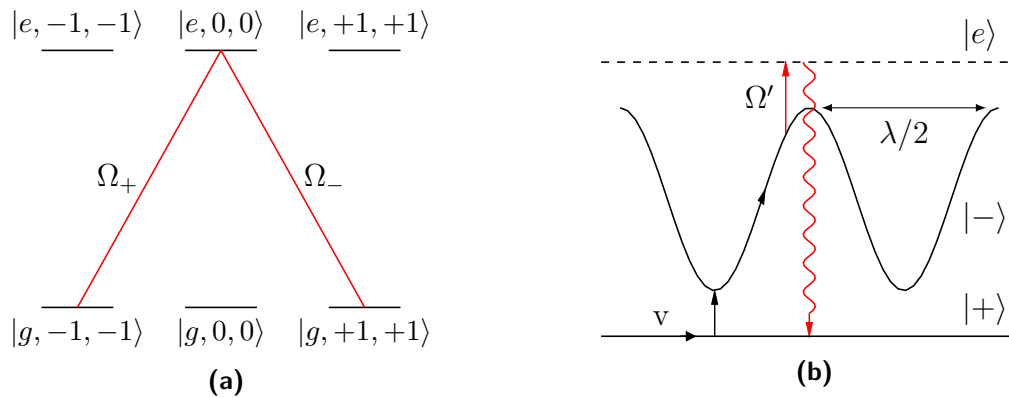


Figure 2.13.: (a) The easiest level scheme for VSCPT is a $F = 1$ to $F' = 1$ transition considering the m_F states as second and the momentum p quantized in units of $\hbar k$ as third parameter of the ket-vector. Two ground states are coupled by two σ -polarized beams. The coupling between $|g, m_F = 0, p = 0\rangle$ and $|e, \mp 1, \mp 1\rangle$ is not considered because atoms excited on these transition can decay to $|g, \mp 1, \mp 1\rangle$, thereby emptying the $|g, 0, 0\rangle$ ground state. The coupling results in two dressed states $|\pm, 0, 0\rangle$. Only the $|-\rangle = |-, 0, 0\rangle$ state couples to the light field, $|+\rangle = |+, 0, 0\rangle$ is a *dark state*. Therefore, atoms at $p = 0$ remain in the dark state avoiding photon scattering. For $p > 0$ the dark state $|+\rangle$ evolves to the *bright state* $|-\rangle$ and scatters photons. After a random walk in momentum space reaching $p \approx 0$, it can decay to the dark state. (b) The VSCPT technique can be improved by using the fact that the bright state experiences light shifts. When two beams form a standing wave, light shifts cause a periodic variation of the energy. Atoms evolving from the dark to the bright state have to climb a potential hill where they lose kinetic energy, resulting in a friction force. It is therefore called *Sisyphus cooling*.

This means that $|+\rangle$ is not coupled to the excited state, and is therefore called a *dark state*. Both $|\pm\rangle$ have the same energy, and $|-\rangle$ (which is referred to as *bright state*) is coupled to $|e\rangle$ with the Rabi frequency $\Omega' = \sqrt{\Omega_+^2 + \Omega_-^2}$ (Ω_\pm refers to the Rabi frequency of the coupling between $|g, \mp 1, \mp 1\rangle$ and $|e, 0, 0\rangle$). For now, only specific momenta have been allowed in the Λ -system. Assuming states $|g, +1, p+1\rangle$ and $|g, -1, p-1\rangle$ with some $p \neq 0$, their kinetic energies would be different, preventing the formation of the dark state because the system is no longer steady-state. From $\frac{(p+1)^2}{2m} = \frac{(p-1)^2}{2m}$ follows $p = 0$. This can be interpreted by noticing that due to the different momenta, the Doppler shift is different for the two beams, which leads to oscillations between the dark and the bright state at a frequency $2kp/m$, which is twice the Doppler shift (m is the atomic mass, k the wave vector of the laser beams). For $p > 0$, the atoms in $|+\rangle$ will thus evolve to $|-\rangle$, and can thus be excited to $|e\rangle$. The spontaneous emission from the decays leads to a random walk in momentum space. At lower velocities, atoms will be in the dark state $|+\rangle$ for longer times. At the end of the cooling process, the majority of atoms occupy the dark state. In momentum space this gives two peaks at $+\hbar k$ and $-\hbar k$ [22, pp.251–156], [63].

Additional nonadiabatic force

The following derivation mainly follows [64]. Consider two counterpropagating beams with linear polarizations that form a standing wave. The angle ϕ describes the phase between those beams, $\phi = 0$ being the case of constructive and $\phi = \pi/2$ destructive interference. A similar level scheme causes the formation of dark states as in VSCPT. The light waves couple $|-\rangle$ to $|e\rangle$ with the Rabi frequency Ω' . This results in a light shift which is, because the light intensity varies in space, position-dependent, giving the level scheme in figure 2.13b. One important change is that now the Ω_+ and Ω_- beams are both blue-detuned (the laser frequency is larger than the transition frequency) with respect to $|e\rangle$ by δ , where $\delta > \Gamma$ (Γ is the natural linewidth) is required for the detuning to be effective. This is necessary because in case of red detuning, the light shift (see equ. 2.36) would be negative and $|-\rangle$ would be energetically below $|+\rangle$, which would cause heating.

The cooling process depicted in fig. 2.13b works as follows: atoms in the non-coupling state $|+\rangle$ with non-zero velocity $v > 0$ evolve to the coupled state $|-\rangle$ with probability (assuming $\delta^2 \gg \omega^2$)

$$P \propto \left(\frac{kv \sin \phi}{E_C/\hbar(1 - \cos \phi)^2} \right)^2, \quad (2.43)$$

which was calculated by the overlap between the reverse time evolution of $|-\rangle$ with

2. Theory

$|+\rangle$. As expected intuitively, it becomes larger with increasing velocity and is reduced for large energy differences between the two levels, which is on average $E_C = \frac{\hbar\Omega^2}{4\delta}$. The ϕ dependence is due to the different amplitude of the energy variation of $|-\rangle$. Atoms in the $|-\rangle$ state have to climb a potential hill until they are excited to $|e\rangle$. The energy difference E_S that is overcome is up to

$$\Delta E_S = \frac{\hbar\Omega^2}{4\delta} \cos \phi, \quad (2.44)$$

which is the light shift reduced by the dependence on ϕ . This process takes place during the optical pumping time τ_P , until the atom is transferred to $|e\rangle$. The atoms move by about one quarter-wavelength with velocity v , giving the proportionality (with $\lambda = \frac{2\pi}{k}$)

$$\frac{1}{\tau_P} = \gamma_P \propto kv. \quad (2.45)$$

γ_P is the photon scattering rate, which is defined as the inverse of τ_P . From $|e\rangle$, the atom can decay back to the dark state $|+\rangle$. The overall cooling force can be estimated by calculating the dissipated power in one cooling cycle which is

$$\frac{dW}{dt} = \frac{\Delta E_S}{\tau_P} \cdot P = -Fv. \quad (2.46)$$

Inserting eqs. 2.43, 2.44 and 2.45 into equation 2.46 and considering that $-Fv = -F\frac{\gamma_P}{k}$, results in

$$F \propto \hbar k \frac{\delta^3}{\Gamma} \cdot \frac{(kv)^3}{\Omega^4} \cdot \frac{\sin \phi^2 \cos \phi}{(1 - \cos \phi)^4}. \quad (2.47)$$

This force vanishes for $\phi = \pi/2$, which is clear since the light fields cancel out. At $\phi = 0$, it diverges at the cost that $|+\rangle$ and $|-\rangle$ overlap and also atoms at $v = 0$ are coupled to the bright state, undermining the VSCPT process. Consequently, $0 < \phi < \pi/2$ is required.

The gray molasses cooling scheme has been successfully implemented [19], [65], [66] on the D1 line of ^{39}K where both the cooling ($F = 2$ to $F' = 2$) and the repumping beam ($F = 1$ to $F' = 2$) are detuned by 3.5Γ to 5Γ . This can be viewed as gray molasses on the cooling line (which works analogously to the level system assumed above but has multiple dark states because of multiple Λ systems that exist), with a repumping beam that couples the $F = 1$ ground state to the system forming even more dark states. One should note that a gray molasses scheme is not possible on the D2 line because the $F = 2$ to $F' = 3$ transition forbids the formation of dark states (states generated by coupling in Λ -like systems would still couple to the light field). Temperatures lower than $10\ \mu\text{K}$ have been achieved with intensities varying between

tenths of the saturation intensity I_S and a few I_S . For ^{41}K , temperatures of $42\ \mu\text{K}$ have been achieved for similar detunings and intensities [67].

Summing up, light-induced coherence between magnetic sublevels causes the formation of dark states, for atoms at zero velocity. Atoms with $v > 0$ can interact with the light field, being slowed down by a Sisyphus cooling process, climbing up a potential hill formed by the light shift due to the standing wave generated by the two counter-propagating laser beams. For potassium, gray molasses cooling on the D1 line allows for lower temperatures to be reached compared to conventional polarization gradient cooling.

2.8. Optical dipole trap

Atoms captured in a MOT are continuously undergoing photon scattering, which limits the achievement of temperatures lower than the Doppler limit T_D or the recoil limit T_{rec} for sub-Doppler cooling techniques. To keep the atoms trapped, they can be loaded into magnetic or optical traps. While the former requires the atoms to be in a specific magnetic substate, the latter is more flexible and is introduced in this section.

This derivation mainly follows [68]. The idea of a *dipole trap* is that a light field $\vec{\mathbf{E}}(\vec{\mathbf{r}})$ with frequency ω induces dipole moments $\vec{\mathbf{p}}$ in the electronic shell of the atoms, giving

$$\vec{\mathbf{p}} = \alpha \cdot \vec{\mathbf{E}} \quad (2.48)$$

with the polarizability α , which is a complex number with a real (dispersive) and complex (absorptive) component. This induced dipole moment couples to the electric field, resulting in a potential energy ($\langle \cdot \rangle$ is the time average) $U_{dip} = \frac{1}{2} \langle \vec{\mathbf{p}} \cdot \vec{\mathbf{E}} \rangle$ which gives (with the electric field intensity $I = 2\epsilon_0 c |E|^2$, ϵ_0 is the vacuum permittivity)

$$U_{dip} = -\frac{1}{2\epsilon_0 c} \text{Re}\{\alpha\} I(\vec{\mathbf{r}}). \quad (2.49)$$

On the other hand, the absorption probability given by $P_{abs} = \langle \dot{\vec{\mathbf{p}}} \cdot \vec{\mathbf{E}} \rangle = \frac{\omega}{\epsilon_0 c} \text{Im}(\alpha) I(\vec{\mathbf{r}})$, where $\dot{\vec{\mathbf{p}}}$ is the time-derivative of $\vec{\mathbf{p}}$, still causes a scattering rate

$$\gamma_{sc} = \frac{P_{abs}}{\hbar\omega} = \frac{1}{\hbar\epsilon_0 c} \text{Im}\{\alpha\} I(\vec{\mathbf{r}}). \quad (2.50)$$

Each atom's electron can be modeled as a Lorentz oscillator with a position x which evolves as $\ddot{x} + \gamma_D \dot{x} + \omega_0^2 x = \frac{-eE}{m_e}$ with resonance frequency ω_0 and damping rate γ_D . From classical optics, the polarizability for such an oscillator is known to be [39,

pp.184, 221–223]

$$\alpha = 6\pi\epsilon_0 c^3 \frac{\Gamma/\omega_0^2}{\omega_0^2 - \omega^2 - i(\omega^3/\omega_0^2)\Gamma}, \quad (2.51)$$

where $\gamma_D = (\omega/\omega_0)^2\Gamma$ is the damping coefficient of a radiating harmonic oscillator. For large detunings $\delta = \omega_0 - \omega$ and small population of the excited state and considering that $\frac{1}{\omega_0^2 - \omega^2} = \frac{1}{(\omega_0 - \omega)(\omega_0 + \omega)} \approx \frac{1}{2\omega_0(\omega_0 - \omega)}$, the potential energy of the dipole trap becomes

$$U_{dip}(\vec{\mathbf{r}}) = \frac{3\pi c^2}{2\omega_0^3} \frac{\Gamma}{\delta} I(\vec{\mathbf{r}}). \quad (2.52)$$

For red-detuning $\delta < 0$, this causes an attractive force $\vec{\mathbf{F}}_{dip} = -\nabla U_{dip}$. By focussing the light on a few tenths or hundreds of micrometers, atoms can be trapped in the focus of the light beam. U_{ind} is also called *trap depth*, typically given in Kelvin, implying that atoms at temperatures below this temperature can be captured. The scattering rate becomes

$$\gamma_{sc}(\vec{\mathbf{r}}) = \frac{3\pi c^2}{2\hbar\omega_0^3} \left(\frac{\Gamma}{\delta}\right)^2 I(\vec{\mathbf{r}}). \quad (2.53)$$

The frequency ω_0 is the atomic transition frequency. It is important that while the trap depth scales with δ^{-1} , the scattering rate scales with δ^{-2} . Consequently, the scattering by single photons can be reduced by using a far detuned light beam. For greater detunings, the trap depth can be preserved by increasing the intensity. The heating due to the scattering processes can be estimated by

$$\dot{T} = \frac{1}{3} T_{rec} \gamma_{sc}. \quad (2.54)$$

In the derivation above, only one resonance frequency ω_0 was assumed. However, alkali atoms like potassium have two important transition lines, D1 and D2. Thus, both detunings have to be incorporated, replacing $\frac{1}{\delta}$ by $\frac{2}{\delta_2} + \frac{1}{\delta_1}$ and $\frac{1}{\delta^2}$ by $\frac{2}{\delta_2^2} + \frac{1}{\delta_1^2}$ (the 2 in the numerator is due to the different line strengths) with detunings δ_2 and δ_1 for the D2 and D1 line respectively. This is valid as long as the detuning is much larger than the ground state hyperfine splitting. Otherwise, the m_F substates might lose degeneracy for circular polarization and have to be treated as separate transitions.

In a nutshell, a light field used to polarize atoms couples to the induced dipoles creating an attractive force for red-detuning and a repulsive force for blue-detuning. The larger the detuning of the light frequency from the atomic transitions, the fewer photon scattering events happen, which prevents heating of the atomic sample. This comes at the cost of a weaker trapping potential, which can be compensated for by increasing the light intensity. The formed potential resembles that of a harmonic oscillator, its quantization opens the possibility of cooling below the recoil limit which

is shown in the following section.

2.9. Raman sideband cooling

Raman sideband cooling is a ground state cooling technique which enables cooling below the recoil limit T_{rec} . Although this has not yet been achieved in practice with potassium, lower temperatures can be reached. Below, *degenerate Raman sideband cooling* (dRSC, [69]) is introduced.

As outlined in section 2.8, light can be used to trap atoms in a harmonic oscillator potential. The level spacing is determined by its eigenfrequency ω_E , which is given by $U_{dip} = \frac{1}{2}m\omega_E\vec{r}^2$ [24, p.135] with the atomic mass m . This leads to vibrational states \vec{n} in the oscillator potential with energies

$$E_n = \left(n + \frac{1}{2}\right) \hbar\omega_E, \quad (2.55)$$

as depicted in figure 2.14. Using standing waves, a lattice can be created with multiple lattice sites, each one being occupied at most by one atom and being described by a harmonical oscillator. A magnetic field is applied to shift the magnetic sublevels such that the states $|g, m_F = 0, n\rangle$, $|g, -1, n + 1\rangle$ and $|g, -2, n + 2\rangle$ are degenerate (the third number in the states denotes the vibrational state of the harmonic oscillator). Then, the following cooling cycle is performed: atoms in the $|g, -2, n\rangle$ state are transferred via $|g, -1, n - 1\rangle$ to $|g, 0, n - 2\rangle$ by Raman coupling. This is achieved using the lattice light, which is far detuned from the excited state. Then, a σ^- polarized beam called *polarizer* excites the atoms to $|e\rangle$, from where they decay preferentially (due to the Clebsch-Gordan coefficients) to $|g, -2, n - 2\rangle$. The vibrational state is conserved as long as the level splitting of the harmonic oscillator is much larger than the recoil energy from spontaneous emission, i.e. the Lamb-Dicke parameter $\eta = \sqrt{\frac{E_{rec}}{\hbar\omega_E}} \ll 1$. This is called the *Lamb-Dicke regime*, where the photon recoil is passed on to the lattice. At the end of the cooling cycle, some atoms might end up in the $|g, -1, 0\rangle$ state. A slight π -polarization component is thus added to the polarizer which empties it. Finally, all atoms are in one state, $|g, -2, 0\rangle$, which is advantageous when commencing experiments [20].

In practice some obstacles remain [70]. Firstly, the σ^- beam causes a light shift and broadening of the $|g, -2, n\rangle$ states, which might cause the states to lose degeneracy. In the case of potassium, the narrow hyperfine splitting requires a repumper for the cooling to function. In [20], the cooling is done on the ^{39}K D1 line, where mainly the $F = 2$ to $F' = 1$ transition is used with blue detuning ($+1.25\Gamma$). The repumper is

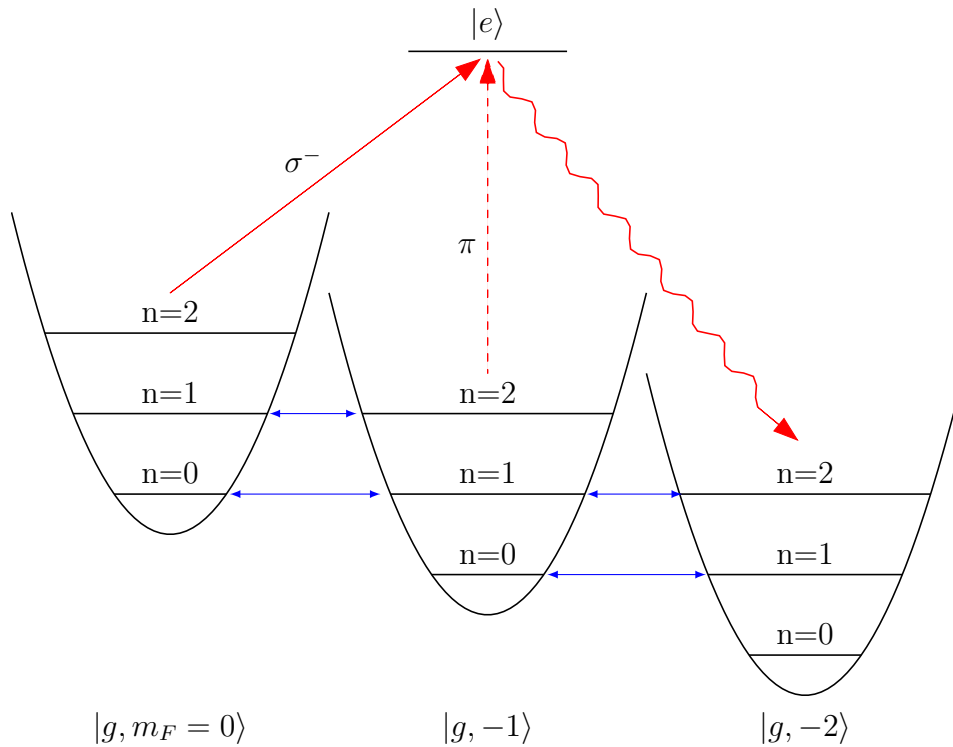


Figure 2.14.: The principle of degenerate Raman sideband cooling: atoms are trapped in an optical lattice (one per site), which can be described as a harmonic oscillator potential, where they occupy vibrational states n . The different m_F states are shifted by a magnetic field such that different vibrational states are degenerate. The cooling cycle is as follows: atoms in $|g, -2, n\rangle$ are transferred to $|g, 0, n - 2\rangle$ by Raman coupling by the lattice light (denoted by the blue arrows), which is far-detuned from the atomic transitions. Then, a σ^- -beam excites the atoms, which preferably decay to $|g, -2, n - 2\rangle$. The vibrational state is preserved for vibrational level splittings much larger than the recoil from the spontaneous decay, thereby facilitating cooling below the recoil limit. Finally, all atoms are in the $|g, -2, n = 0\rangle$ dark state, atoms ending up in $|g, -1\rangle$ are pumped towards the dark state with the π -polarized component of the laser beam.

operated on $F = 1$ to $F' = 2$, slightly red-detuned (-1.3Γ). Both beams have very low power (on the order of μW) and are shone towards the atoms along the magnetic field axis, with a slight tilt to generate the π -component needed. With this setup, temperatures as low as $1.5\ \mu\text{K}$ were achieved.

2.9.1. Raman sideband cooling to BEC

The capabilities of Raman sideband cooling go so far that a Bose-Einstein condensate (BEC) of ^{87}Rb was created without the need for evaporative cooling, the commonly used mechanism [71]. dRSC was performed in a 2-dimensional lattice (on the D1 line with a large red detuning of the σ^- beam of about 100Γ to reduce heating due to scattering processes), of which the confinement along one axis was turned off thereafter to compress the sample on the other axis. After another dRSC phase, the compression was repeated in the other direction followed by a final dRSC phase, after which a BEC of 1400 atoms was obtained in only 300 ms. This is fast compared to evaporative cooling which needs seconds to create a BEC (although the achievable atom number is larger for evaporative cooling, [72], [73]).

In conclusion, Raman sideband cooling is a technique to reach sub-recoil temperatures, even enabling the creation of Bose-Einstein condensates. Atoms are trapped in the vibrational states of an optical lattice, which prevents heating from recoil momenta. A cooling cycle consisting of Raman coupling between degenerate states and optical excitation transfers the atoms to low vibrational states. In the experiment, Raman sideband cooling might be used to reach even lower temperatures after gray molasses cooling if needed.

3. Experimental setup

As mentioned in the introduction, the experimental setup is designed to be able to perform different experiments, including:

- Lattice atom interferometry to perform precision measurements such as tests of gravity, fundamental constants, search for dark matter or dark energy to find physics beyond the standard model. The potential energy landscape close objects can be probed, and novel effects due to thermal radiation (e.g. objects in a thermal radiation bath) can be measured.
- Investigation of interactions between electrons and atoms. In particular the implementation of the *Quantum Klystron* (QUAK) experiment, which uses a modulated electron beam to drive hyperfine transitions. This requires the installation of an electron source in the vacuum chamber. Furthermore, atoms with a small ground state hyperfine splitting are favorable, because it is easier to modulate the electron beam at lower frequencies.

To perform these experiments, a magneto-optical trap is needed with further cooling mechanisms to reach lower temperatures. Thus, a vacuum chamber is needed for the MOT, with a 2D MOT as an atom source attached to it. The design of the chambers should allow for the realization of sub-Doppler- and Raman sideband cooling. Furthermore, the LATIN experiment requires a cavity to produce a standing wave which forms the lattice used to trap and hold the atoms during interferometry [74], [75], [12]. After performing experiments, it is necessary to read out the atomic state to observe the phase for LATIN or the transitions caused by the modulated electron beam. A *blowaway beam* is needed, resonant with the cooling transition, that spatially separates the atoms in the $F = 1$ and $F = 2$ ground states. This allows for the determination of the atom number in both states using fluorescence imaging [76]. Potassium atoms are used as the atomic species because of the small ground state hyperfine splitting of both the ^{39}K and ^{41}K isotopes, which is advantageous for the QUAK experiment. For LATIN and blackbody radiation experiments, the ^{39}K isotope will be used because the cooling techniques are more advanced and it should be easier to reach lower temperatures (see secs. 2.7.2 and 2.9). Concerning the electron beam, it might be necessary to replace the electron source to achieve the required density modulation and beam diameter. For maintenance and to exchange between different

electron sources, a transfer chamber with a separate vacuum pump is used which can be detached from the science chamber. In addition, the transfer chamber might be useful to insert objects into the chamber, e.g. test masses or a heated cylinder as in [7].

To drive hyperfine transitions with ultra high frequency (UHF) waves (which is needed e.g. for Ramsey interferometry, [77]), antennas will be placed outside of the vacuum chamber. In addition, after using Raman sideband cooling, it is necessary to move the atoms from a magnetically sensitive Zeeman substate to the $m_F = 0$ state. This can be achieved with UHF waves using stimulated rapid adiabatic passage (STIRAP) [78] or adiabatic passage [79, pp.49–50]

Subsequently, the vacuum setup is described briefly. The optical setup and generation of the desired laser frequencies are shown and the principle of the experiment control system is explained. Finally, simulations made to design the magnetic fields needed for the 2D and 3D MOT are presented as well as first measurements of the fields generated by the 2D MOT coils.

3.1. Vacuum setup

The vacuum chamber, shown in figure 3.1, consists of the following parts:

The science chamber (marked A in fig. 3.1), with the 3D MOT in its center, is where the experiments will take place. Three larger windows ensure optical access for imaging and additional light beams if needed. Plus, the atoms can be released into free fall and be imaged below the center. The laser beams for the 3D MOT and sub-Doppler cooling are fiber coupled and fixed to the vacuum chamber for higher stability, except for the two beams along the z -direction.

The 2D MOT (marked C) generates a beam of atoms to load the MOT. It is separated from the science chamber by a differential pumping stage, which maintains the pressure ratio of about 10^{-4} to capture many atoms from the background gas in the 2D MOT while keeping the pressure low in the science chamber to reduce collision losses during experiments. The 2D MOT ensures short loading times and thus fast experiment cycles (see section 2.5). It is pictured in more detail in fig. 3.2.

The transfer chamber (B) is separated from the science chamber with a valve (F). It can therefore be opened without losing the vacuum in the science chamber. This is useful to change electron sources or insert other objects into the chamber. A wobble stick (G) can be used to align inserted objects under vacuum. The

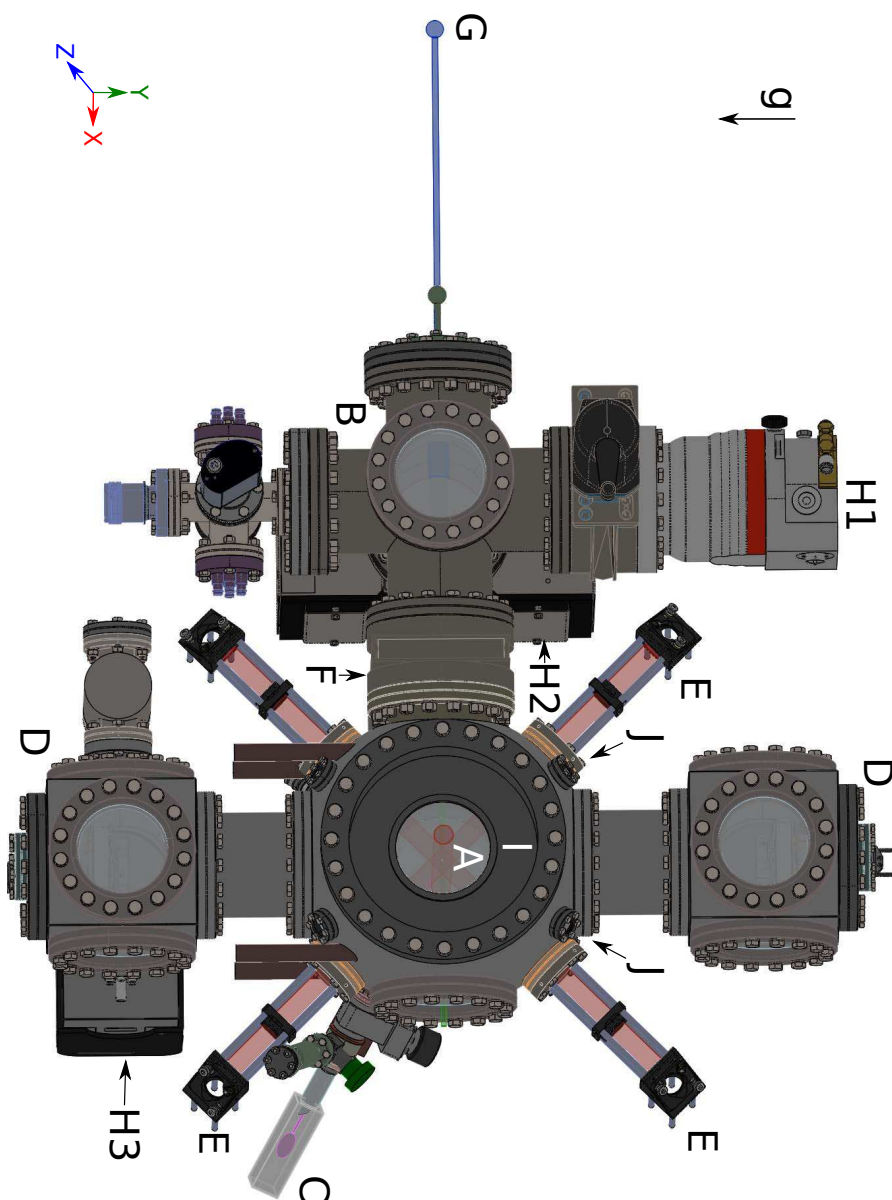


Figure 3.1.: The vacuum chamber: the experiments take place in the center of the science chamber (A): a 3D MOT is loaded using a 2D MOT (C), the light is supplied with cage systems (E) attached to the vacuum chamber and placed in front and back of the science chamber (not shown). The transfer chamber (B), separated from A with a valve (F) can be used to place electron sources for the QUAK experiment, which can be moved in the science chamber with a wobble stick (G). The two mirrors forming the cavity needed for LATIN are placed above and below the science chamber (D). Vacuum pumps (one turbomolecular pump, H1, and two mostly hidden ion getter pumps, H2 and H3) provide ultra-high vacuum $< 1 \times 10^{-10}$ mbar. The MOT coils are placed in the reentrance flange (I), additional vacuum windows (J) allow for the installation of a lattice for dRSC.

transfer chamber features its own set of vacuum pumps (a turbo and ion pump, H1 and H2) to reach pressures as low as in the science chamber ($\approx 10^{-11}$ mbar).

The cavity in the vertical direction (D) consists of two mirrors located in the upper and lower part of the setup. The distance between the two mirrors has to be a multiple of half the wavelength of the hyperfine ground state transition. This ensures that both wavelengths needed for the Raman transition can be cavity modes. The wavelength of the hyperfine transition of ^{39}K (^{41}K) is 32.4 cm (59 cm), so a cavity length of about 60 cm is thus needed in our setup. For fine adjustment, piezo controlled mirror mounts are used. To change between isotopes however, manual adjustment would be required. The bottom part of the cavity setup can also be used for imaging with a light sheet in the future, to detect single atoms [80].

Below, further details on the science chamber and 2D MOT are given.

3.1.1. Science chamber

The laser light for the MOT and sub-Doppler cooling is provided by six cage systems (see fig. 3.8), of which four are directly mounted on the vacuum chamber (E in fig. 3.1). Two are providing light along the z -axis and are placed next to the chamber. In addition, a pair of anti-Helmholtz coils which creates the magnetic field gradients for the MOT and CMOT will be mounted inside the reentrance flange of the science chamber (I). Three pairs of compensation coils form a cage around the science chamber to compensate for magnetic fields from the earth, vacuum pumps etc. to reach zero magnetic field during the gray molasses phase and when performing experiments (not shown).

A turbomolecular pump from Pfeiffer Vacuum attached to the transfer chamber (H1) with a 300 l s^{-1} pumping rate is used to reach pressures of about 10^{-7} mbar, subsequently ion getter pumps (H2 and H3) from Gamma Vacuum with 75 l s^{-1} and 100 l s^{-1} pumping rates respectively shall reach pressures lower than 10^{-10} mbar. Pumps H1 and H2 allow for the recovery of the vacuum after exchanging electron sources, for instance. Meanwhile, vacuum pump H3 holds the vacuum in the science chamber.

3.1.2. 2D MOT

The 2D MOT is pictured in fig. 3.2. Two pieces of metallic potassium in natural abundance (1 g each) in glass ampoules are put in a bellow (A) and are broken in vacuum. By heating the bellow, the vapour pressure inside the glass cell from Precision Glass-

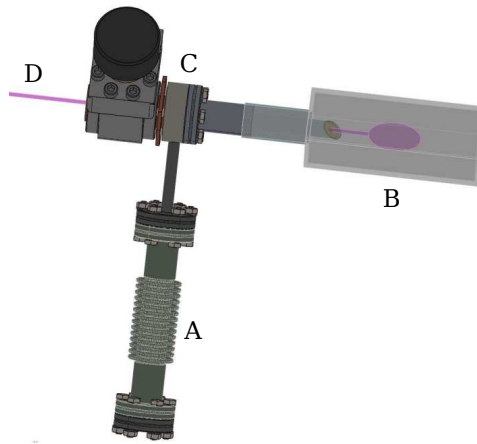


Figure 3.2.: The 2D MOT: a metallic potassium sample is heated up in (A). This results in a vapour pressure in the glass cell (B), where a 2D MOT captures the atoms (shown as a purple ellipse) which leave through a small hole in a copper tube (the differential pumping stage) towards the science chamber. The face of the tube forms an angle of 45° with its axis such that it can be used to reflect a counter-propagating beam (see sec. 2.5.4).

blowing (B) is controlled. Two retroreflected beams form a 2D MOT therein (with optional push- and counterpropagating beam, or the possibility to tilt the beams, see sec. 2.5.4). The atomic beam (colored in purple, D) exits towards the science chamber through a differential pumping stage formed by a copper tube with 2.4 mm diameter. Its face is chamfered at 45° , which allows for a counterpropagating beam to be used.

3.2. Laser setup

To be able to perform the experiments described above, laser light is needed:

- Laser light on the D2 line of ^{39}K and ^{41}K is needed for the 2D- and 3D MOT. A survey of different existing setups with potassium [30], [51], [81], [38], [29], [40] lead to the conclusion that less than one Watt of optical power for both the 2D- and the 3D MOT should be sufficient. It was therefore decided to purchase a TA pro 765 from Toptica, which provides 2.7 W at the output and 1.8 W coupled into an optical fiber. The narrow ground state hyperfine splitting of potassium allows us to generate all desired (cooling and repumping) frequencies from one single laser using acousto-optic modulators, as explained in section 3.3.
- Because the sub-Doppler cooling on the D2 line of potassium is difficult due to the small hyperfine splitting in the excited state (see sec. 2.7.1), additional

light on the D1 line is needed to perform gray molasses cooling (sec. 2.7.2). It is also required to perform Raman sideband cooling (sec. 2.9). The laser diode of a Toptica DL 100, which was previously used at 780 nm was replaced by a LD-0790-0120-AR-2 diode with a large tuning range to operate at 770 nm. A BoosTA 315 seeded with 25 mW optical power amplifies the light, resulting in 1.2 W of power at the output and about 700 mW fiber-coupled.

Below, the setups of both lasers including their stabilization is shown.

In figure 3.3, the Toptica TA pro 765 used to produce the D2 light (at 766.7 nm) called *Tom Turbo* is pictured as a blue rectangle. As sketched, it contains a laser, a tapered amplifier (TA) and two optical isolators (also called *Faraday isolators*). A small fraction of the light from the laser is split off and is mostly used to stabilize the laser. The laser is an *external-cavity diode laser* (ECDL), which consists of a laser diode (at a p-n-junction, electrons and holes recombine, emitting radiation, [24, pp.284–285]), whose wavelength is controlled by the supplied current and its temperature, and an external grating, which forms a resonator together with the diode. The resonator length is controlled by applying a voltage to a piezoelectric actuator [82]. The laser diode provides an overall power of ≈ 45 mW, which is not sufficient for our purpose. Thus, a TA increases the optical power by a factor of 100. It functions similarly to a laser diode except that the faces are not reflective and the shape is optimized to sustain the produced heat [73, p.20]. Two optical isolators prevent damage to the diode and the TA chip from backreflected light. The amplified laser power is coupled into a fiber leading to the setup described in section 3.3. The TA pro [83] is controlled by a Toptica DLC pro rack [84], which features not only the current and piezo supplies and the temperature stabilization, but also a locking module (DLC pro Lock) for laser stabilization. The latter is realized by modulating the laser current at low frequency $\omega_M = 2\pi \cdot 20$ kHz. This is well below the natural linewidth of potassium $\approx 2\pi \cdot 6$ MHz and should therefore not affect the atoms when interacting with the D2 light. The small fraction that is split off after the first optical isolator (about 2 mW optical power) is sent through an acousto-optic modulator (AOM), which is needed to prepare the desired frequencies as described in section 3.3. Afterwards, the beam is split in a pump and probe beam to perform saturation absorption spectroscopy, cf. section 2.3.1. The modulation of the beam is analogous to the frequency modulation spectroscopy described in sec. 2.3.2, except that the probe beam is modulated as well, which should not have a noticeable effect. The probe beam is detected by a photodiode (denoted PD in fig. 3.3) and the signal is fed back to the DLC pro, which generates the error signal using a lock-in-amplifier. To obtain a frequency spectrum, the piezo voltage is scanned. The stabilization of the laser (also known as *locking*) on the $F = 2$ to $F' = 3$ cooling transition (see fig. 2.2), is done on the DLC's touch screen or in a graphical user interface on a connected computer. Two internal PID-regulators are used to adjust the

diode current and piezo voltage to correct for changes of the laser frequency. Because the potassium in the vapour cell (Thorlabs GC25075-K) is in its natural abundance, the laser is always stabilized to the cooling transition of ^{39}K because ^{41}K transitions are difficult to see due to the low occurrence of the ^{41}K isotope.

The ECDL laser used to produce the laser light for the D1 line (at 770.1 nm) is a repurposed Toptica DL 100 [85] named *Mimi*. It is controlled by a Toptica SYS DC 110 rack [86], as shown in figure 3.4. The temperature and current of the laser diode are controlled by the DTC 110 and DCC 110 modules. The piezo voltage is generated in the PID 110 module, which generates a ramp to scan the spectrum (the function generator symbol “~”) and includes a PID regulator for stabilization of the laser frequency. To prevent modejumps which could occur when adjusting only the position of the grating (by changing the piezo voltage), the *feed forward* function allows the current to be changed simultaneously which, when appropriately adjusted, allows for a large mode-hop-free tuning range [85]. The majority of the output power is sent to the Toptica BoosTA 315 through a fiber, from which it is delivered to the main optical setup (see sec. 3.3). A small fraction is used for spectroscopy. After shifting the frequency by +90 MHz with an AOM, the light is split into a pump beam which passes through the vapour cell (a Thorlabs GC25075-K) after being phase modulated by an electro-optical modulator (EOM, a resonant PM7-NIR_T from Qubig is used) with frequency $\omega_M = 2\pi \cdot 5 \text{ MHz}$, and an unmodulated probe beam which passes directly through the cell before being detected by a photodiode (a Thorlabs PDA36A-EC with 10 MHz bandwidth). Inside the vapour cell, the sidebands of the pump beam are transferred to the probe beam by *four-wave mixing* if both beams are on resonance with atoms of the same velocity v . This technique is called modulation transfer spectroscopy (MTS) and was explained earlier in section 2.3.3. Because the nonlinear four-wave mixing only occurs on resonance, the signal detected on the photodiode resembles equation 2.17. The DC component of the PD signal, which contains the absorption spectrum, is split off with a Bias-T (Minicircuits ZFBT-6GW+) and shown on an oscilloscope. Afterwards, the generation of the error signal is done by applying the *Pound Drever Hall method* on the AC component. The photodiode signal is mixed with a *local oscillator*, a signal with frequency $\omega_{LO} = \omega_M$ generated by the same function generator that drives the EOM (Rigol DG832). The mixing circuit (a Minicircuits ZRPD-1) is the electronic analogue of mathematical multiplication. Together with the 2.5 MHz low-pass filter (Minicircuits BLP-2.5+), the error signal results in what was yielded in equations 2.18 and 2.19, depending on the phase between the photodiode signal and the local oscillator. The PID regulator of the PID 110 module is finally used to “lock” the laser on the coinciding ^{39}K crossover transitions of the $F = 1$ to $F' = 2$ and $F = 2$ to $F' = 1$, and $F = 2$ to $F' = 1$ and $F = 1$ to $F' = 2$, with a frequency offset of +90 MHz created by the AOM. This is done by applying the

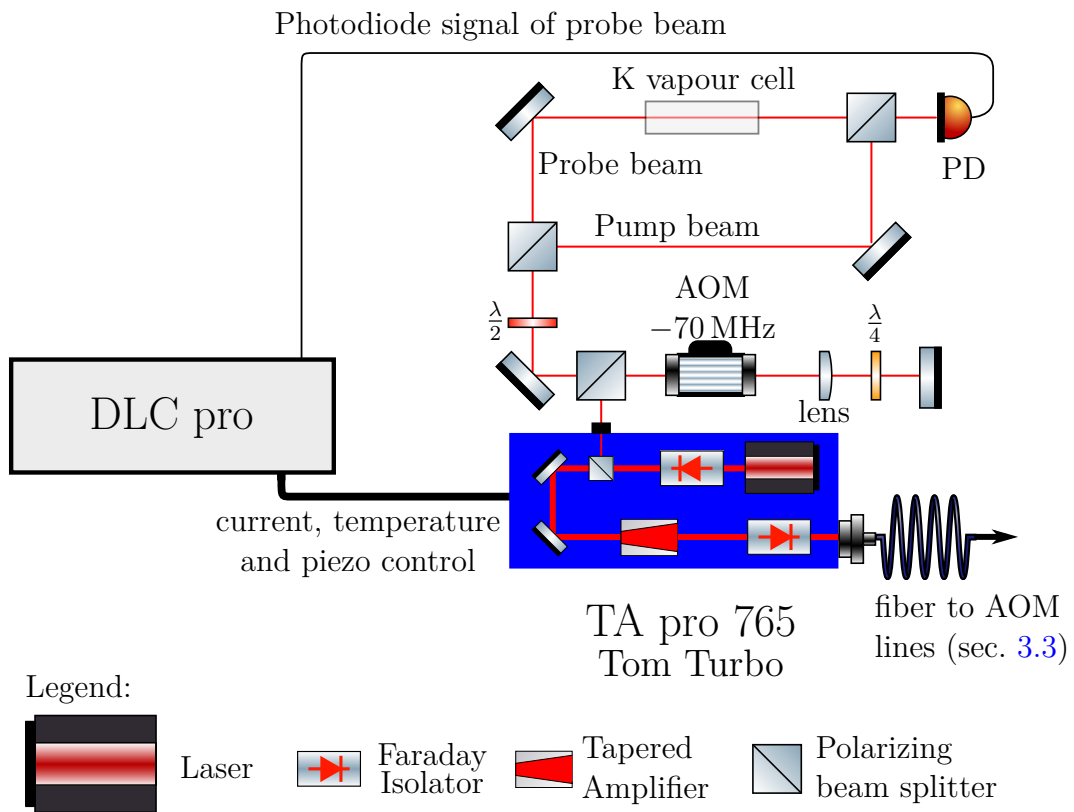


Figure 3.3.: Setup and stabilization of the TA pro 765 used to generate the D2 light for the experiment: the light of the laser seeds a tapered amplifier (TA), which generates the power needed for the experiment. A small fraction is used to perform spectroscopy. After passing twice through an AOM operating at -70 MHz frequency, it is split into pump and probe beam and sent through a vapour cell with potassium in its natural abundance. The probe beam is detected by a photodiode and the signal is sent to the DLC pro. An error signal is obtained by modulation of the laser diode current at 20 kHz and a lock-in amplifier inside the DLC pro. The laser is stabilized to the cooling transition of ^{39}K ($F = 2$ to $F' = 3$), with a frequency offset of $+140$ MHz due to the AOM.

3. Experimental setup

error signal to the laser's piezo voltage and diode current instead of the ramp used to obtain an absorption spectrum. Again, due to the low abundance of ^{41}K , the locking transition remains the same when changing the isotope. However, the AOM will be turned off when using ^{41}K (see fig. 3.7).

To sum up, two lasers producing light on the D2 and D1 lines of potassium are stabilized using saturation absorption spectroscopy. The error signals are obtained using FMS with a low modulation frequency and a lock-in amplifier, and MTS with an EOM and a self-built Pound-Drever Hall detector. The lasers are stabilized to the cooling transition and the crossover transition between the ground states of ^{39}K . In order to get the needed cooling and repumping frequencies, the laser frequency is shifted by AOMs, as explained below.

3. Experimental setup

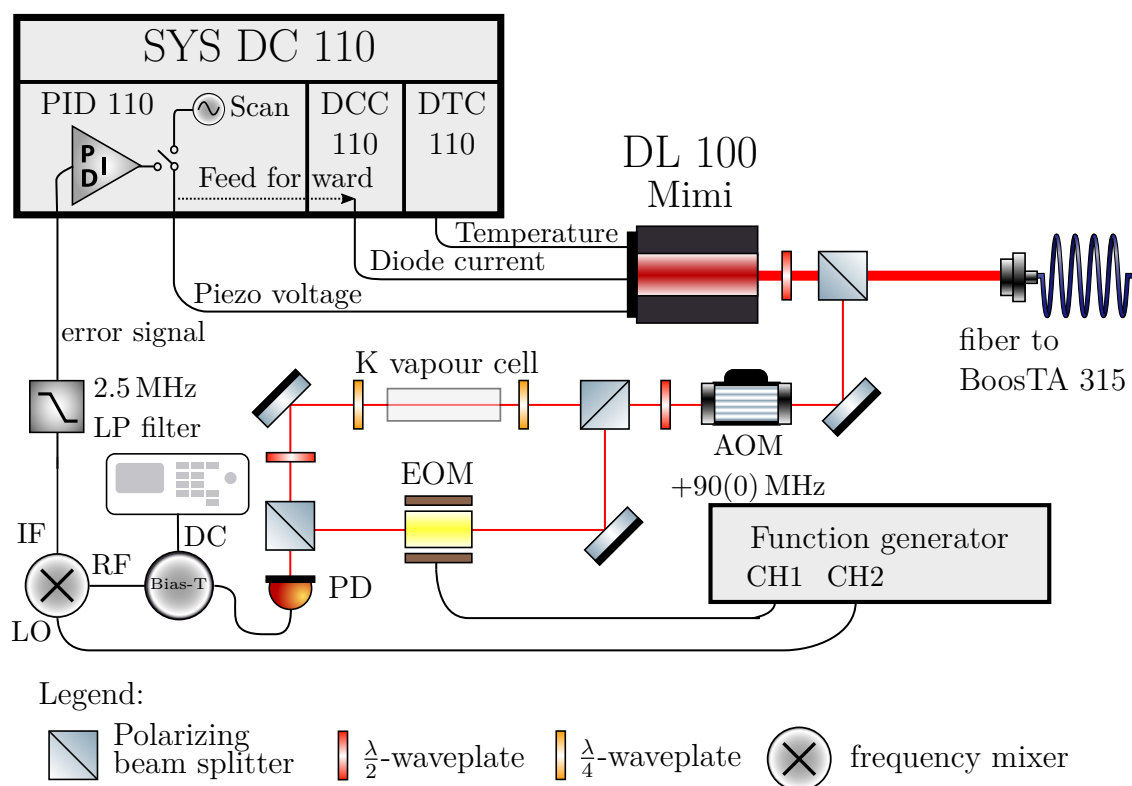


Figure 3.4.: Setup and stabilization of the DL 100 laser producing the D1 light needed for gray molasses and Raman sideband cooling: the majority of the optical power is used to seed the BoosTA 315 amplifier, from which the light is delivered to the AOM line setup described in sec. 3.3. A small fraction is split off to perform modulation transfer spectroscopy (MTS). With an electro-optic phase modulator, frequency sidebands are applied to the probe beam at a frequency $\omega_M = 5$ MHz. In the potassium vapour cell, these are transferred to the probe beam via a nonlinear process only if both beams are resonant with the same atoms (the same condition as in Doppler-free spectroscopy). The probe beam is detected on a photodiode and the DC part containing the saturation absorption spectrum, is split off with a Bias-T and displayed on an oscilloscope. The oscillating part of the signal is mixed with a local oscillator signal (LO) at frequency ω_M . After a low-pass filter, an error signal is obtained containing the absorptive and dispersive derivatives of the transmission through the cell depending on the phase between photodiode signal and local oscillator, cf. sec. 2.3.3. The PID 110 module of the Toptica SYS DC 110 laser controller provides a sawtooth signal to scan the laser frequency, as well as a PID regulator to stabilize the laser on a transition using the error signal. The laser is stabilized on the crossover transition between the hyperfine ground states of ^{39}K , shifted by +90 MHz by the AOM shown. When using the ^{41}K isotope, the AOM is turned off.

3.3. Optical setup

In this section, the optical setup used to generate the laser frequencies needed for the various cooling techniques is shown. The difficulties of obtaining the correct polarizations and switching between the two isotopes, ^{39}K and ^{41}K , are discussed. Finally, the system for aligning the beam in the vacuum chamber is presented.

The frequency shifting is done by acousto-optic modulators (AOM), which consist of a crystal with a piezo transducer attached to it. The piezo driven at frequencies in the range from 80 MHz up to several hundred MHz produces sound waves or phonons inside the crystal (see fig. 3.5a). A photon passing through the crystal can absorb or emit a phonon depending on the angle between their momenta. The photons' frequency and propagation direction is thereby changed, leading to different diffraction orders, comparable to Bragg scattering. The incident angle θ is chosen according to Bragg's law

$$2\lambda_S \sin \theta = m\lambda_L \quad (3.1)$$

where λ_L and λ_S are the wavelengths of the photon and phonon, and m is the diffraction order. Therefore, AOMs enable the precise control of the light frequency and amplitude by controlling the frequency and power of the sound wave. By turning the frequency supply on and off, they can be used as fast switches (on the order of 100 ns). The drivers providing the RF power (radiofrequency power) to the AOMs are discussed in section 3.4. A commonly used configuration known as *double-pass* is shown in figure 3.5b, where the refracted beam is reflected back into the AOM and hence modulated twice. A lens with focal length f is used to collimate the first diffraction order, assuming they originate from a point source within the crystal. Thereby, changes of the diffraction angle originating from changes with the modulation frequency do not change the alignment. The beam itself is focused onto the mirror, which makes it necessary to position the mirror at a distance f from the lens. The zero-order beam is dumped and a quarter-waveplate changes the polarization such that the reflected beam can be separated from the incident beam using a polarizing beam splitter (PBS) [87]. Typical diffraction efficiencies are 70%-90% for a single-pass setup; for a double-pass setup the efficiency is reduced accordingly [88].

The optical setup was designed to meet the following requirements:

- The power available on the D2 line is only 1.8 W. Compared to other experiments, where additional tapered amplifiers are often used after generating the frequencies with the AOMs, it has to be used economically.
- The setup should allow for switching between the ^{39}K and ^{41}K isotopes.
- As explained thoroughly in section 2.2, the repumper plays an important role

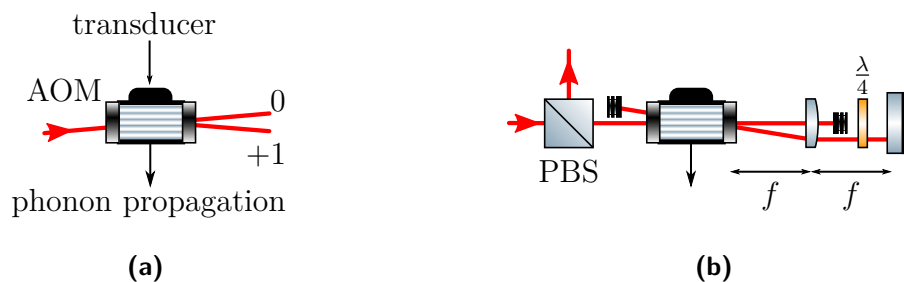


Figure 3.5.: (a) The functionality of an acousto-optic modulator: a piezo attached to a crystal generates a sound wave of frequency ω_S . Photons can absorb or create a phonon inside the crystal if Bragg's law is fulfilled. Photons diffracted into the ± 1 order have their frequency shifted by $\pm\omega_S$. This allows for control of the laser frequency and amplitude, by changing the wavelength and intensity of the sound wave. (b) The double-pass setup: the laser beam passes through the AOM twice. After the first diffraction, a lens compensates for the diffraction angle varying with frequency. A quarter-waveplate is passed twice, changing the horizontal polarization of the incident beam to vertical, such that the reflected beam can be separated with a polarizing beam splitter (PBS).

when laser cooling potassium. Therefore, the polarization of the repumper in the MOT has to match the cooler polarization, which might not be important in experiments with rubidium or cesium.

- If possible, the setup should be flexible, meaning that as many parameters (e.g. frequency and intensity of a beam) as possible should be tunable to be able to optimize the different cooling stages independently.

The first two requirements suggest that each light beam that is generated for a specific purpose should only pass one AOM to minimize losses and use the available power efficiently (adding a second AOM in series for the second isotope would cause additional loss, for instance). This can be seen in figure 3.6, where the setup is shown (AOMs in double-pass configuration are simplified, the lens and quarter-waveplate pictured in fig 3.5b are not shown). Several beams are split off the incoming D2 or D1 light using half-waveplates and polarizing beam splitters, pass through one AOM and the beams are finally overlapped to achieve the desired frequency combinations needed for the 2D MOT, 3D MOT etc. The switching between the two isotopes is accomplished by rotating waveplates (marked with “S”) to guide the light to different AOMs. These can be motorized to automate the switching process.

The overlapping of the beams is challenging, because the polarization of the overlapped beams has to be the same, which is not the case when using a PBS. Alternatively, a non-polarizing beam splitter can be used and either half of the power is blocked afterwards (which is not an option for this setup) or both outputs are used.

The latter option has the drawback that it is impossible to manufacture a beam splitter such that transmission and reflection are exactly equal. Consequently, the beams are overlapped on a PBS with orthogonal polarization, a $\frac{\lambda}{2}$ -plate applies a rotation of 45° and both the cooling and repumping light are split on a second PBS into two. The intensity might be different in both outputs, which can be compensated by dropping the power difference if needed. In addition, the D1 and D2 light have to be overlapped, which is achieved using two interference filters from Radiant Dyes, with a FWHM of less than a nanometer. The consequence of this solution is that for each application (2D and 3D MOT) there are always two beams, which make the use of a miniaturized setup such as a pyramidal MOT less beneficial since either 50% of the power is lost or the concept has to be adapted to work with two beams (cf. secs. 2.4.3 and 2.5.5).

The last requirement is flexibility. A double-pass AOM configuration is preferred because its alignment is less sensitive to variations of frequency. However, for the gray molasses cooling (GMC) the frequency is constant which explains the use of single-pass setups for the D1 light. Fig. 3.6 also shows the mechanical shutters (the design was adapted from [89] by our electronic workshop) used to block the remaining light from leaking into the vacuum chamber to prevent scattering during the experiment, which would cause systematic error and instabilities. In the 2D MOT part, one shutter is used to deliver light for the blowaway beam, which is generated by reusing the cooler AOM of the 2D MOT.

In figure 3.7, the frequencies needed for the 2D-, 3D MOT and GMC are given, with the laser frequencies at the LOCK points. The detunings were taken from [30] to provide a starting point when optimizing the setup. The lock point of the D1 laser is shifted when switching isotopes (the AOM ahead of the spectroscopy is turned off for ^{41}K , see fig. 3.4), so one repumper AOM can be used for both isotopes.

The six fibers leading to the 3D MOT are connected to the cage system shown in fig. 3.8. It is connected directly to the vacuum chamber with an adapter. A Schäfter+Kirchhoff 60FC-T-4-M100S-02 collimator parallelizes the beam to a waist diameter of ≈ 16 mm. It is mounted on a mirror mount which provides, together with the gold-coated mirror M, enough degrees of freedom to align the beam such that they overlap in the center of the science chamber. A quarter-waveplate mounted in a clear 22.9 mm aperture produces circular polarization and ensures that more than 98% of the power can pass through. The MOT beams are also used to perform fluorescence imaging. After the experiment, the atomic cloud will be in free fall for a few milliseconds. Therefore, one has to ensure that the beam diameter is large enough to saturate the atoms. This motivates the calculation of an effective beam diameter wherein the light intensity is above saturation. On resonance, it is larger than the aperture (24.6 mm), which allows for free-fall times up to 30 ms (this corresponds to

3. Experimental setup

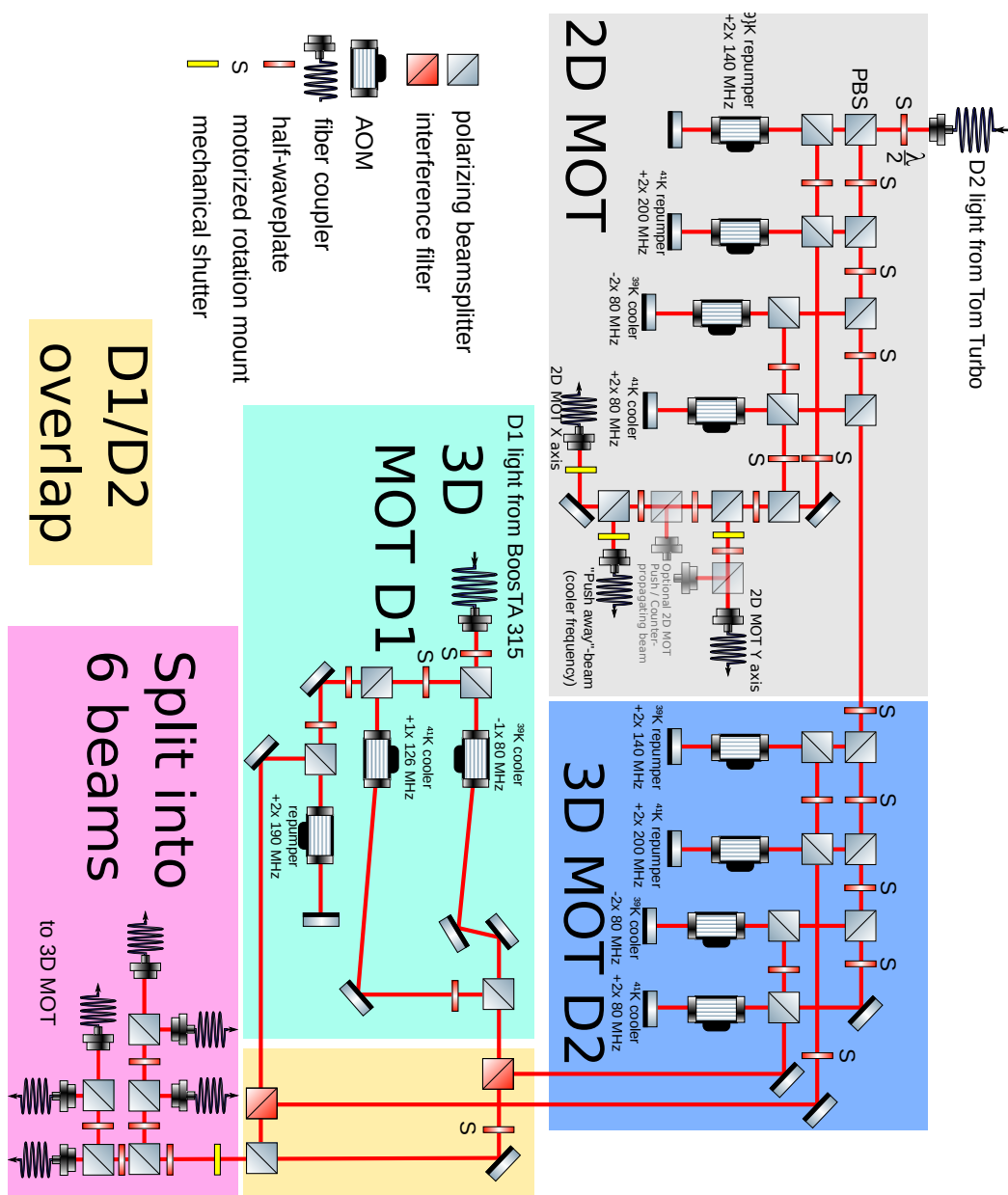


Figure 3.6.: The optical setup producing the frequencies needed for the 2D MOT, 3D MOT and GMC. AOMs in double-pass configuration are displayed simplified (without lens and $\lambda/4$ -plate). The switching between the ^{39}K and ^{41}K isotopes is done by rotation mounts which might be motorized in the future (marked with “S”). The push- and counterpropagating beams might be needed in the future and are thus semi-transparent. The cooling and repumping beams of the D1- and D2 line are overlapped using interference filters and two polarizing beam splitters. Mechanical shutters are used to prevent leakage of light during the experiment and to reuse a part of the 2D MOT light for the blowaway beam.

3. Experimental setup

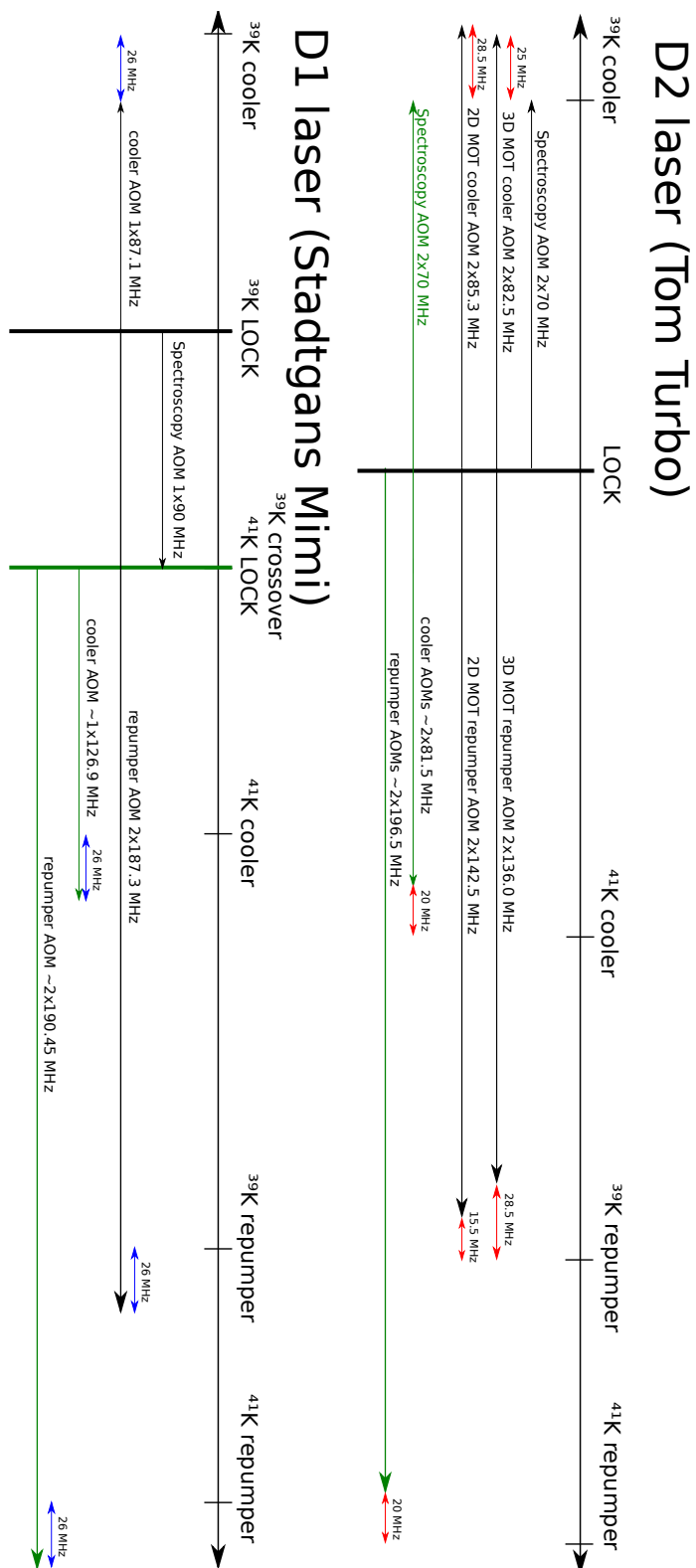


Figure 3.7.: Sketch on the frequencies produced by the AOMs in fig. 3.6. The detunings were taken from [30] to be used as initial values for later optimization.

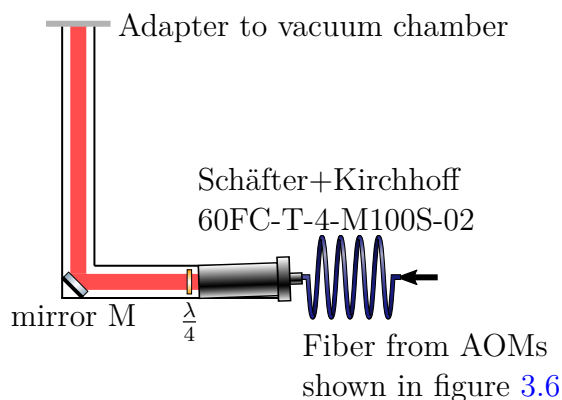


Figure 3.8.: The cage system which is attached to the vacuum chamber: a collimator from Schäfter+Kirchhoff is attached to a mirror mount. Together with mirror M, sufficient degrees of freedom are available to overlap the MOT beam in the center of the vacuum chamber. The quarter wave plate changes the linear polarization of the light from the fiber to circular polarization.

a displacement of 4.5 mm).

In conclusion, acousto-optic modulators generate the frequencies for the 2D MOT, 3D MOT, gray molasses cooling and the blowaway beam. The switching between the two isotopes is achieved by rotating wave plates, thereby selecting different AOMs. Cage systems attached to the vacuum chamber allow for a stable alignment of the 3D MOT beams.

3.4. Frequency generation with direct digital synthesis

The AOMs shown in fig. 3.6 and 3.7 operate at frequencies of 70 MHz to 200 MHz. Depending on the frequency, 1 W to 2 W of radiofrequency (RF) power have to be supplied. In this section, the frequency source based on direct digital synthesis (DDS) is presented.

A DDS is running at a system clock frequency f_S which is derived from an external reference. The signal is synthesized by reading discrete values from a lookup table, a digital-to-analog converter creates the analog waveform [90]. This is advantageous compared to voltage controlled oscillators [91], which are LC oscillators tunable with variable capacitors whose resonance frequency might change with temperature. In order to stabilize them, phase-locked loops [92] have to be used. Also, instead of requiring a lot of knowledge of analog circuitry, the main challenge lies in programming. The DDS is convenient because it allows for applying frequency, phase and amplitude

sweeps while producing a stable frequency.

For the purpose of generating the RF signal for the AOMs, the Analog Devices AD9959 DDS chip was chosen [93]. It is clocked at frequencies up to 500 MHz, which allows us to synthesize sinusoidal signals up to 250 MHz (a limit which is set by the Nyquist-Shannon theorem, [94, p.419]). Its four channels allow for the generation of four signals, whose relative phases can be controlled. To avoid the difficulties involved with the design of a printed circuit board (PCB), the AD9959 Evaluation Board [95] was chosen, which features 200 MHz low-pass filters for each channel and outputs with $50\ \Omega$ impedance [95]. To operate the board, an external power supply and control of the AD9959 via SPI interface (serial I/O port interface) is needed, which lead to the design of two PCBs providing the supply (see fig. 2 in the appendix) and the serial interface (see fig. 3), which allows the control by an Arduino Nano microcontroller. The internal clock speed $f_S = 500$ MHz is derived from an external reference clock, which is a sinusoidal signal at 25 MHz generated by a Rigol DG832 function generator. The SPI interface is used to set frequencies and amplitudes of the four channels and to configure frequency sweeps. The sweeps are triggered by digital inputs, as suggested by figure 3.9. To protect the inputs of the AD9969 chip, optocouplers are used (Avago ACPL-772L, on the PCB providing the serial interface, see also fig. 3). The microcontroller itself is connected to the control computer via USB and appears as a serial COM port device which allows for communication via the RS232 protocol. In addition, the laser power has to be controlled (e.g. ramping is needed for various cooling techniques, see secs. 2.6.1, 2.6.2, 2.7) and be turned on and off quickly. Because changing the settings via RS232 takes a few 100 μ s per channel and can not be timed precisely, a variable voltage attenuator (VVA, a Minicircuits ZX73-2500-S+) and a RF switch (Minicircuits ZYSWA-2-50DR+ with switching times of 20 ns) are used. They are placed after the pre-amplifier (Minicircuits ZFL-500HLN+), which amplifies the DDS output signal of less than 4 dBm (this corresponds to a peak-to-peak voltage of 1 V, it gets lower with increasing frequency) to less than 15 dBm, and are controlled with analog and digital signals respectively. In figure 3.9 the setup is shown for one channel as an example. Pre-amplifiers and RF switches are needed for all four channels, the VVAs and trigger inputs are only available on two channels because frequency and amplitude sweeps are not needed for all AOMs (e.g. for the AOM in the spectroscopy or for gray molasses cooling). Outside of the DDS Box, a power amplifier amplifies the signal to powers of 1 W (Minicircuits ZHL-3A+) for the lower frequency AOMs and 2 W (Minicircuits ZHL-1-2W+) for the higher-frequency (> 150 MHz) ones. An attenuator is placed in front so as not to exceed the maximum input power of 10 dBm (chosen to account for losses in the VVA and RF switch). To change between isotopes, a Minicircuits ZSW2-63DR+ RF switch is used, which is capable of sustaining 4 W of RF power. The DDS Box can also be used to generate

3. Experimental setup

the signal for the UHF antennas used to drive hyperfine ground state transition and to transfer atoms between two different m_F states. To achieve higher frequencies, a Minicircuits FD-2+ frequency doubler is used together with a second Minicircuits ZFL-500HLN+ amplifier which compensates the losses in the former.

To sum up, signals for driving acousto-optic modulators are generated using direct digital synthesis (DDS). With additional amplifiers, 1 W to 2 W of electrical power is provided. Frequency and amplitude can be controlled with a RS232 interface and by analog and digital signals. This allows for integration in the controlling system described below.

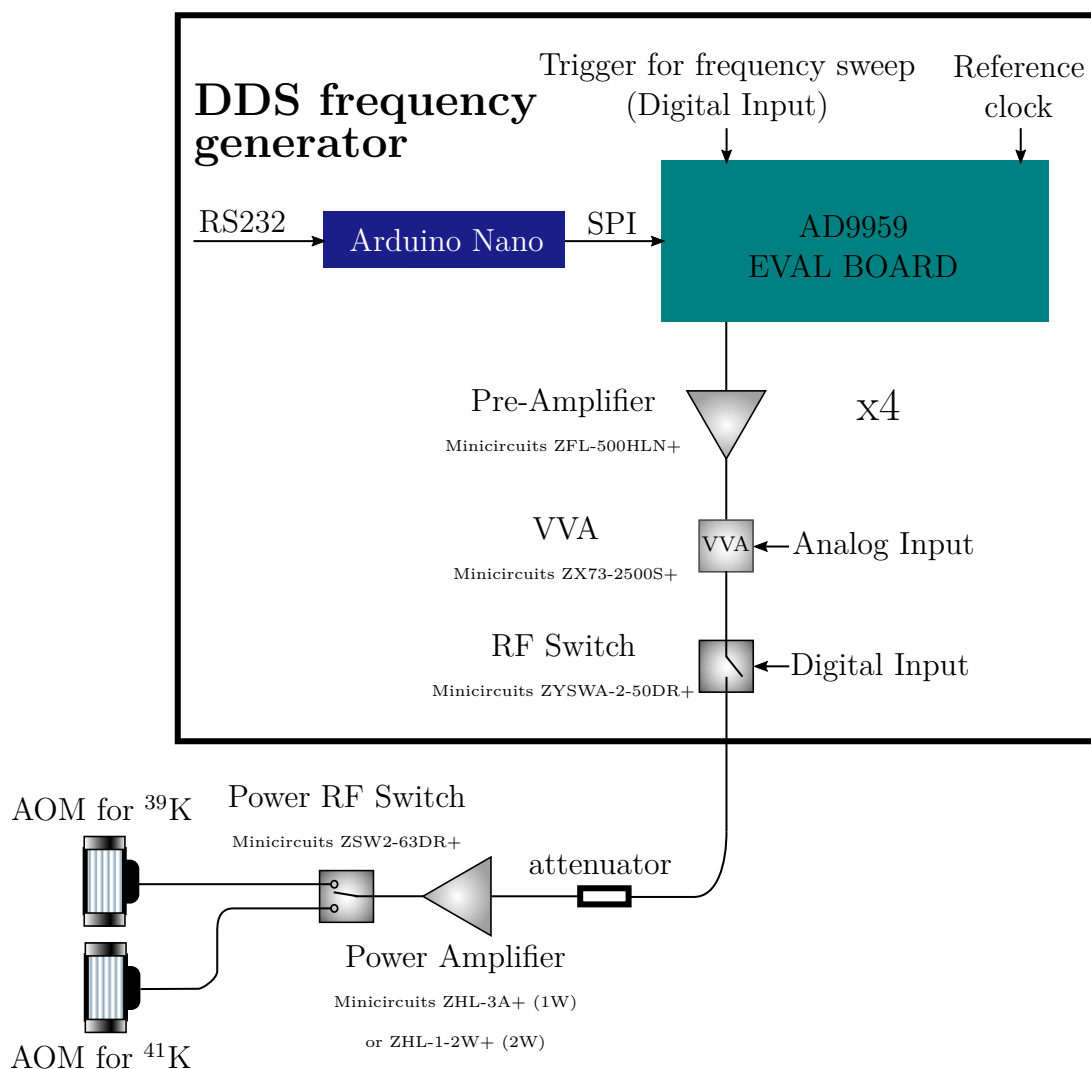


Figure 3.9.: The frequency generator used to drive the AOMs: an evaluation board from Analog Devices with an AD9959 DDS chip is used to generate four sinusoidal waveforms. The internal clock frequency of 500 MHz is derived from a reference clock at 25 MHz. Frequency, amplitude and frequency sweeps are set via SPI interface by an Arduino Nano. The sweeps are triggered with a digital input (for two channels). After pre-amplification, a voltage variable attenuator (usually only available for two channels) and RF switch are used to vary the intensity and turn the waveform on and off. A final amplifier provides 1 W to 2 W of RF power, which is delivered to the AOM after passing a switch which selects between the two AOMs used for the ^{39}K and ^{41}K isotopes respectively.

3.5. Controlling system

Each experimental run consists of three steps: firstly, atoms are captured, cooled to low temperatures and prepared in a certain quantum state. After the actual experiment is performed (e.g. atom interferometry or interactions between atoms and electrons), atoms in different hyperfine ground states are spatially separated and images of the atomic cloud are taken to determine the atom number in each state (this is called *imaging*, [76]). In order to perform the various laser cooling stages, experiments and imaging, a controlling system is needed. The Cicero Word Generator software [96] provides a graphical user interface to control analog and digital output cards from National Instruments and a plethora of devices using the RS232 serial protocol.

The structure of the controlling system is shown in figure 3.10. At its heart is the control PC “Fritz Fantom” which is running Cicero, the graphical user interface and Atticus, the accompanying server that controls the National Instrument cards to output analog (PCIe-6738) and digital (PCIe-6537B) signals. VHDCI cables [97] lead to a *breakout box*, where the analog and digital channels (32 each) are interactable via BNC connectors. The two cards are clocked at 350 kHz (they are synchronised with a RTSI cable), which results in time steps of 2.86 μ s. This is sufficient to perform linear ramps on analog outputs within several ms (which is needed e.g. for the CMOT and dark SPOT phases). Furthermore, Atticus can configure devices via the RS232 protocol (e.g. DDS frequency generators). In addition, a programme translating Ethernet VISA to RS232 commands allows the control of Ethernet devices (for instance the Rigol DP832 power supply). The analog and digital outputs (AO and DO producing voltage levels from -10 V to 10 V respectively TTL signals of 0 V and 3.3 V) control the magnetic field of the MOT coils, the mechanical shutters (which were adapted from [89]) and amplitude and frequency sweeps of the frequency generators for the AOMs and RF antennas. At the end of the experimental sequence, pictures of the atoms are taken with a Thorlabs DCC3240N camera, which is triggered by a digital signal. The image data is transferred via USB to the Control PC to perform data analysis. The pictures and the executed experimental sequence are both stored on a database.

A separate Raspberry Pi 4 computer (called “Das Frettchen”) is used to monitor environmental conditions such as temperature and humidity and the powers of the laser beams during the experimental runs. The latter is achieved by measuring stray light from mirrors or polarizing beam splitters with OP999 photodiodes to detect power reductions caused by slight misalignments of optical elements. Humidity and temperatures are recorded every minute (with a Pi-Plates THERMOplate and DHT 22 sensors) in a database on the logging device and can be viewed on a web interface. During each experimental cycle, the photodiode voltages are acquired with a Pi-Plates

3. Experimental setup

DAQC2plate and transferred to the Control PC, where they are stored alongside images and sequence data. In addition, voltages and currents of power supplies can be retrieved to detect and save indications of errors.

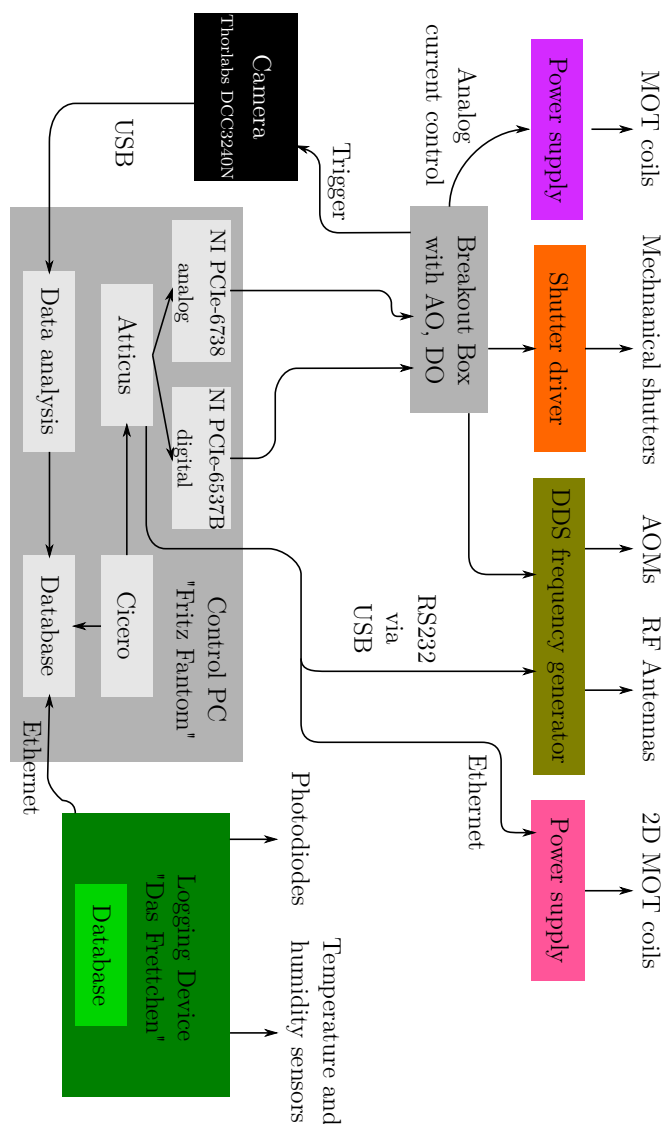


Figure 3.10.: The controlling system: analog and digital output card from Nation Instruments (NI PCIe-6738 and PCIe-6537B) are controlled by the Atticus server. In addition, commands can be sent to devices via RS232. Cicero is a graphical user interface to define the control sequences, which are finally executed by Atticus. The analog and digital outputs (AO and DO) on the breakout box control the magnetic field gradient for the MOT, mechanical shutters and the DDS-based frequency generators (the analog and digital inputs in fig. 3.9). The latter is also controlled via RS232, additional coils are programmed via Ethernet. At the end of each experiment, pictures of the atomic cloud are taken. This is done with a camera, the image is transferred via USB and saved in a database, together with the sequence data. A separate programme is used for data analysis. To monitor temperature and humidity of the environment and vacuum chamber, spectroscopy cells etc., a separate *logging device* is set up. During the experimental run, voltages from photodiodes collecting stray light from mirrors are measured to monitor the powers of the laser beams.

3.6. Magnetic field coils

For the 2D- and 3D MOT, magnetic field gradients have to be produced with anti-Helmholtz coils. To decide on coil size, current and number of windings, simulations were made using the *magpylib* Python library [98].

3.6.1. 3D MOT gradient coils

The 3D MOT coils have to provide a constant gradient during the MOT loading. In the subsequent CMOT phase, the gradient is increased during a few milliseconds. In a dark SPOT phase, the current is then ramped down (again in a few ms) and finally turned off before the gray molasses. During the molasses, no magnetic field is allowed (it would lift the degeneracy of the magnetic m_F substates), and the turn-off time has to be fast (less than a ms).

From [40] and [30] it was deduced that radial gradients from 5 G cm^{-1} to 10 G cm^{-1} are needed for the MOT, which are increased up to 30 G cm^{-1} during the CMOT phase. Since the scope of this experiment is not to create a BEC (where high densities are needed), the requirement for the CMOT phase was set to 15 G cm^{-1} .

The “speed” of the coil is determined by its time constant $\tau = \frac{L}{R_{ohm}}$, the ratio of its inductance L and its internal ohmic resistance R_{ohm} [39, pp.129–130]. Using a voltage source, it takes about 5τ for the coil to reach the desired current when turning it on or increasing the voltage. It should be noted however, that a current supply can turn the coil on much faster by applying higher voltages, but this is limited in practice and the regulation of a real power supply will cause oscillations of when reaching the set current. The gradient A of an anti-Helmholtz pair of coils with radius R , N windings and a current I is approximately ([39, p.92], replacing I with $N \cdot I$ for a coil with multiple windings)

$$A = \frac{48}{25\sqrt{5}} \frac{\mu_0 N I}{R^2} \quad (3.2)$$

with the magnetic vacuum permeability μ_0 . For a fixed gradient A and constant current I it follows that

$$N \propto R^2. \quad (3.3)$$

The inductance of a loop with radius R , wire radius a and N windings is approximately ([99], the factor N^2 was added by replacing the currents I_i with $N \cdot I_i$ in equ. (2))

$$L \approx \mu_0 N^2 R \left(\ln \frac{8R}{a} - 1.75 \right). \quad (3.4)$$

for $a \ll R$ and neglecting the skin effect for constant current operation. To first order and considering equ. 3.3, L is proportional to

$$L \propto N^2 R \propto R^5. \quad (3.5)$$

Consequently, the size of the coil determines to a large degree the inductance and thus the possible ramping speed, as required above. Due to the large size of the vacuum chamber (see sec. 3.1), the coils are placed in a reentrance window, as shown in fig. 3.1 (I). This resulting inductance is on the order of 10 mH, in contrast to about 80 mH when using coils with radii on the order of the vacuum chamber radii (the inductances are given neglecting the relative permeability of the vacuum chamber, which is slightly paramagnetic).

The time constant τ is also determined by the ohmic resistance R_{ohm} of the coil. It has to be reasonably low to avoid heating the coils too much, but high enough to allow for small τ .

As a compromise, coils with 125 mm (average) diameter placed at an (average) distance of 160 mm with 150 windings each are used. At a current of 7 A, the resulting magnetic field and its gradient (5.74 G cm^{-1} in radial direction) is shown in figs. 3.11a-3.11c. The dependence of gradient and heat dissipation (in one coil) on the current is shown in fig. 3.11d. The achievable gradient per unit current is $0.82 \text{ G cm}^{-1} \text{ A}^{-1}$. The heat dissipation for gradients smaller than 10 G cm^{-1} is less than 75 W per coil (since the CMOT phase is very short, the larger heat dissipation does not play a significant role). With a wire cross section of 2 mm^2 (consisting of an insulated copper band with $20 \times 0.1 \text{ mm}$ cross section), the inductance calculated using equ. 3.4 becomes 8.2 mH. The resistance per coil is 0.5Ω , which results in a time constant of $\approx 17 \text{ ms}$. This is rather large, but allows us to increase the magnetic field gradient from 5 G cm^{-1} to 15 G cm^{-1} by using the power supply (Delta Elektronika SM 70-22) as a current source. The same applies for decreasing the gradient. To achieve the fast turn-off requirement in less than a millisecond, a special snubber circuit [94, pp.38–39] will be developed.

3.6.2. 2D MOT

Concerning the 2D MOT, besides the coils configuration shown in fig. 2.11, an alternative configuration similar to the one shown in [52] was considered. As can be seen in fig. 3.12, two rectangular coils produce a quadrupole field, and most of the z -component is compensated with a circular coil. The resulting magnetic field is shown in figs. 3.13a and 3.13b for a current of 1.5 A with 100 windings on each coil. The gradient on the z -axis is shown in fig. 3.13d and enlarged in fig. 3.13e. On a length of

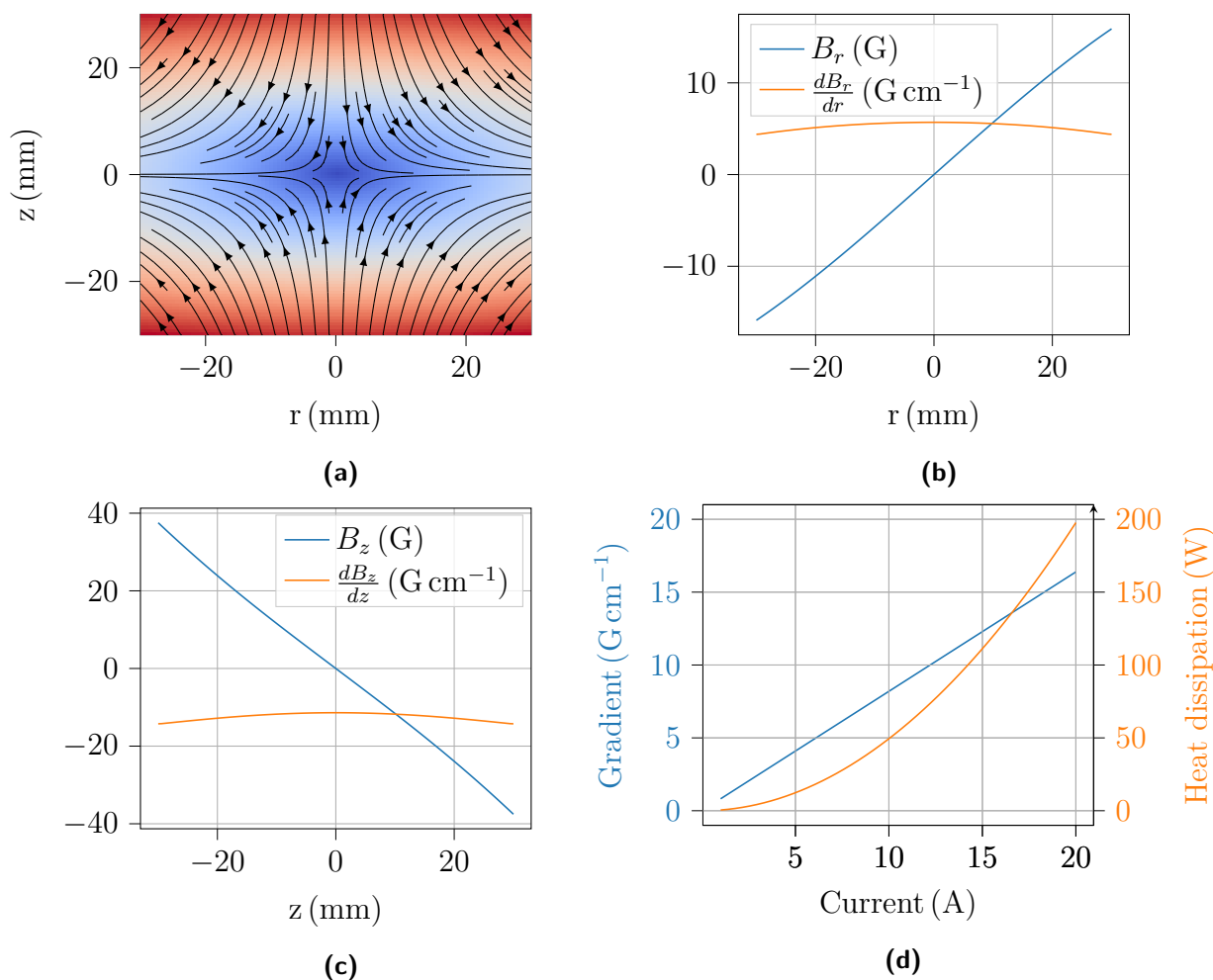


Figure 3.11.: (a) Magnetic field for the 3D MOT in radial and axial directions for the coils of 125 mm diameter at 160 mm distance with 150 windings at a current of 7 A. (b-c) Magnetic field and gradient for the 3D MOT in radial and axial directions respectively. (d) The dependence of the gradient (blue curve) on the current and the corresponding heat dissipation (orange line) for a 2 mm 2 wire cross section.

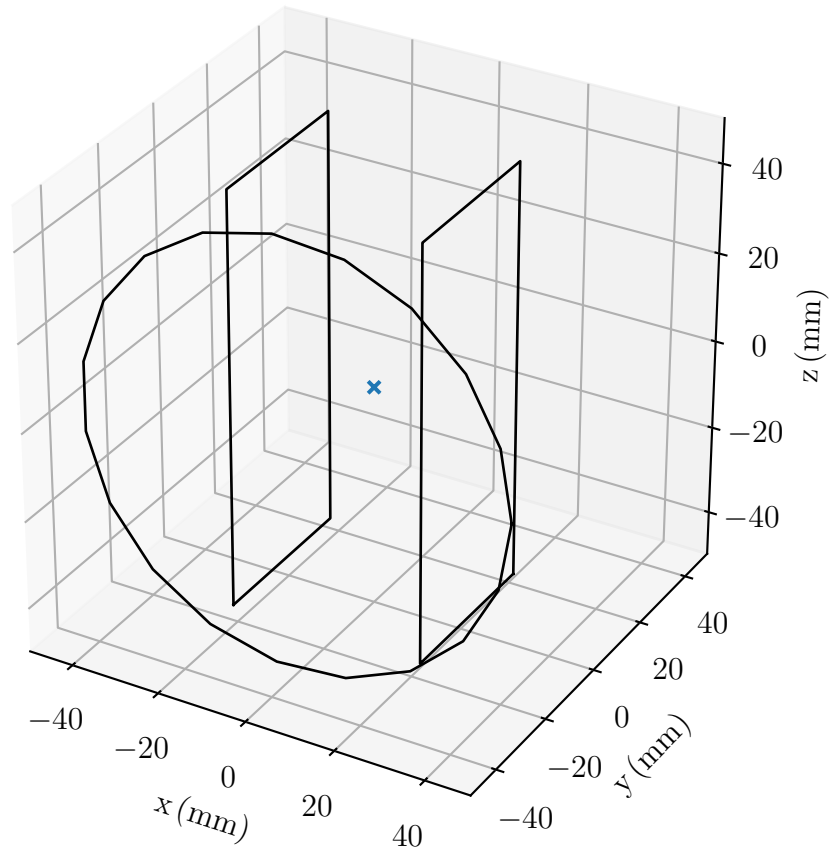


Figure 3.12.: The coil configuration for the 2D MOT, adapted from [52]: two rectangular coils form an anti-Helmholtz pair, whose gradient along the z -axis is mostly compensated by the circular coil (see fig. 3.13). By controlling the currents of the three coils independently, the zero line of the magnetic field can be moved in x - and y -directions such that the atoms exiting the MOT volume can leave through the differential pumping stage.

more than 30 mm around $z = 0$, the gradient is less than one tenth of the gradients in x - and y -direction. The magnetic field and gradient on the x -axis are shown in fig. 3.13c, the latter amounts to -17.38 G cm^{-1} at the origin. In the y -direction it is positive (17.27 G cm^{-1}) to conserve the magnetic flux. This setup is advantageous because it allows for shifting the z -axis for aligning it on the 2.5 mm hole leading to the differential pumping stage by controlling only three coils independently. Changing the current in one of the rectangular coils shift the axis in x -direction, a variation of the circular coil's current shifts it in y -direction. Consequently, only three currents have to be tuned separately.

The gradients used in potassium 2D MOTs are less than 20 G cm^{-1} [52],[51]. 100 windings have been chosen to let us use a Rigol DP832 power supply with its maximum current of 3 A. Gradients up to 30 G cm^{-1} should be accomplishable with this setup (see fig. 3.13f). The size was chosen based on a dimension of the glass cell used for the 2D MOT ($100 \times 30 \times 30 \text{ mm}$) to $94 \times 38 \text{ mm}$ for the rectangular coils (the distance in between is 43 mm) and a radius of 48 mm for the circular coils placed 31.5 mm from the origin. Windings with copper wires of 0.75 mm diameter have a resistance of $0.04 \Omega \text{ m}^{-1}$, resulting in heat dissipations of less than 12 W per coil at the maximum current.

In figures 3.14a and 3.14b, the first measurements of the magnetic fields along the x - and z -directions are depicted. The measurements were taken with a BCD AH49E Hall sensor which was coarsely calibrated using a long wire with 10 A of current as a crude reference (fine calibration will be done later using microwave spectroscopy). The sensor was moved with a stepper motor and measurements were taken in 2 mm steps. The measured magnetic field is a bit larger compared to the simulations. This might be due to the poor calibration of the sensor.

3.6.3. Compensation coils

Finally, three pairs of compensation coils will be used for the 3D MOT to compensate for external magnetic fields originating from the earth, lab equipment etc. Additionally, it is possible to provide small bias fields (as a quantization axis or to deliberately cancel the degeneracy of the Zeeman substates) up to 3 G.

3. Experimental setup

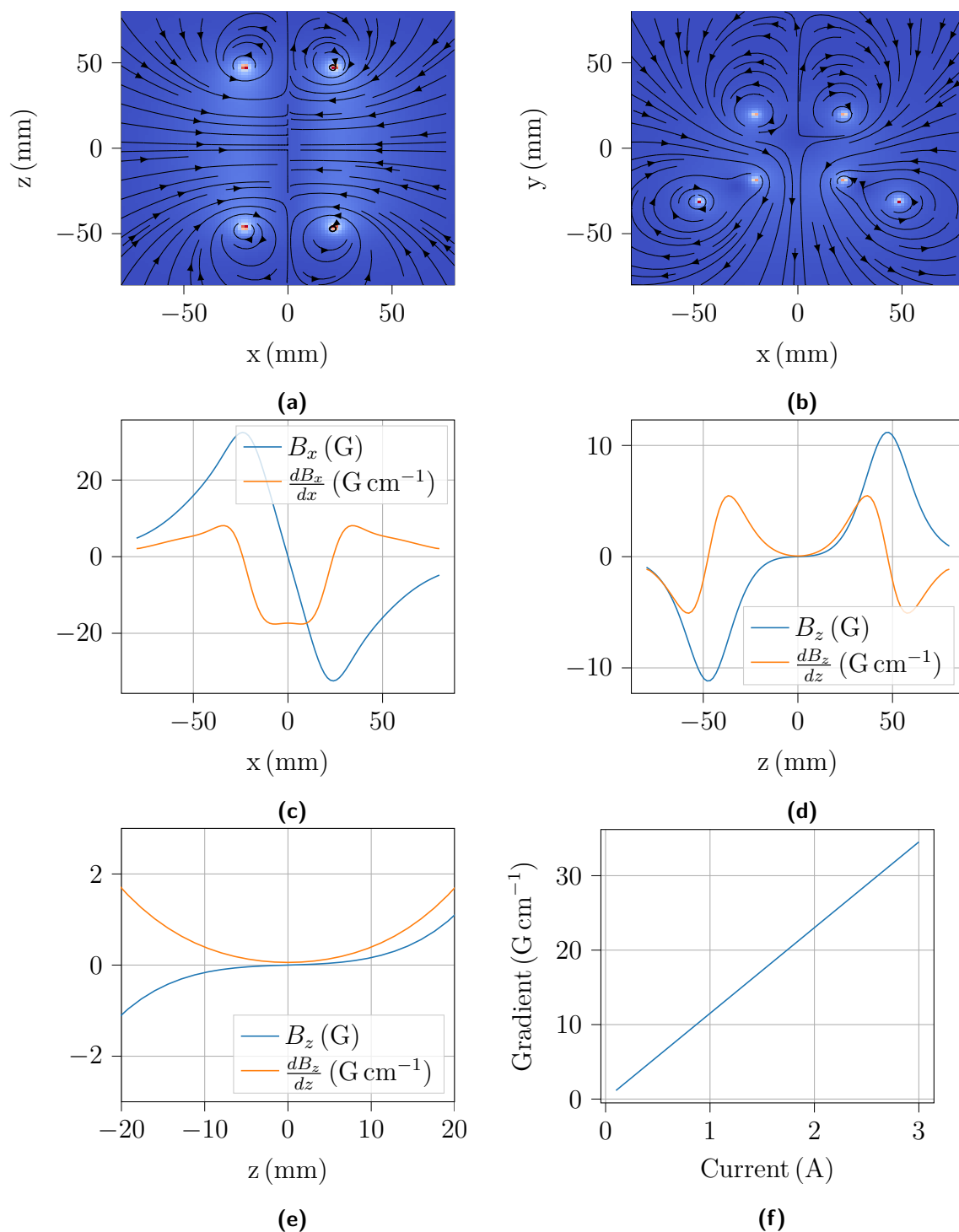


Figure 3.13.: In (a) and (b), the magnetic field resulting from the configuration shown in fig. 3.12 is depicted for a current of 1.5 A with 100 windings. The radial gradient is displayed in (c) for the x -axis, on the y -axis the magnetic field is similar but multiplied by -1 . Figures (d) and (e) show the remaining field and gradient on the z -axis, which is negligible for the purpose of a 2D MOT. In (f), the dependence of the radial gradient on the coil current is depicted.

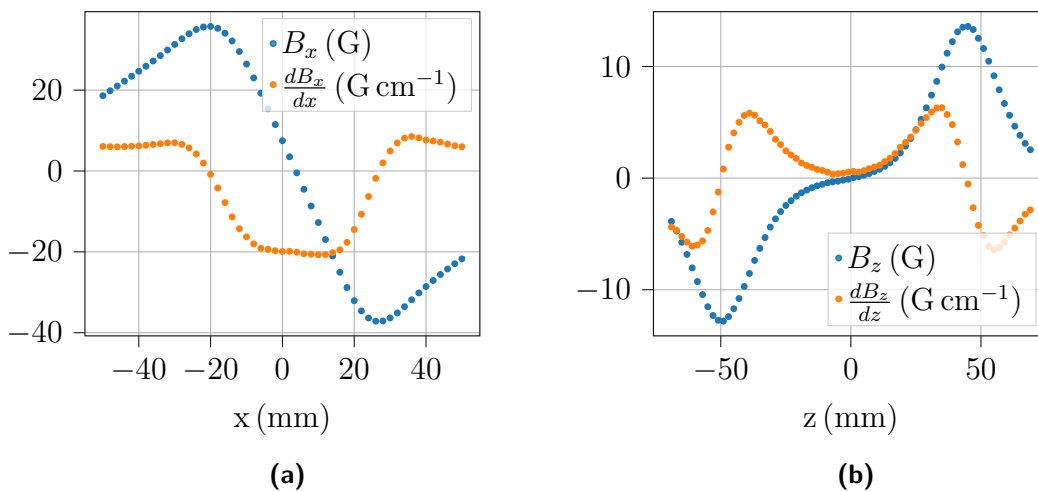


Figure 3.14.: First measurements of the magnetic field of the 2D MOT coils with a current of 1.5 A along the x - and z -direction, shown in (a) and (b) respectively. The AH49E Hall sensor which was used for the measurement was coarsely calibrated with a long wire with 10 A of current as reference. This causes a systematic error of 10% to 20% due to the coarse distance measurement between sensor and wire. The measurement uncertainty was estimated to be up to 200 mG. The uncertainty regarding the step size of the stepper motor causes an additional systematic error (up to 2%) for the magnetic field gradient.

3.7. Imaging

At the end of each experimental run, pictures of the atomic cloud are taken to determine the populations of the two hyperfine ground states. This is achieved by applying the *blowaway beam* on the cooling transition to spatially separate atoms in different states [76]. Finally, the MOT beams are turned on and an image of the fluorescence is taken to measure the atom numbers of the two distinct clouds.

A Thorlabs DCC3240N CMOS camera is used to take pictures of the fluorescence imaged by a camera objective with a 50 mm lens. The F number quantifies the luminosity of an objective defined by the ratio of the lenses focal length f and aperture D : $F = \frac{f}{D}$. When $D < f$, the solid angle captured from a point source (in the present case the atomic cloud) becomes [39, p.362]

$$\Omega = \frac{\pi}{4} \frac{1}{F^2}. \quad (3.6)$$

This becomes important when measuring the atom number, because smaller F increases the sensitivity (see below). For the purpose of this experiment, objectives with $F = 1.4$ or $F = 1.1$ will be used.

3.7.1. Estimation of the atom number

The number of photons originating from the atomic cloud is determined by the photon scattering rate $\gamma_P = \Gamma\rho_{ee}$ (see equ. 2.2, [22, p.25]) multiplied by the atom number N . The objective captures the fraction $\frac{\Omega}{4\pi}$ (see equ. 3.6) of emitted photons with energy $\hbar\omega_P$. The (spatially resolved) image on the camera results in a signal (the sum of all photons detected on the camera)

$$U = \epsilon \cdot N \frac{\Omega}{4\pi} \cdot \hbar\omega_P \cdot \gamma_P, \quad (3.7)$$

which is limited by the detection efficiency ϵ (the DCC3240N has a quantum efficiency of $\approx 60\%$). To determine the latter, a calibration has to be performed using a laser beam with a known intensity. For the purpose of the experiment presented in this thesis, two spatially separated atomic clouds are recorded (the different states), from which the photons are counted separately. To subtract residual features not originating from the atomic cloud, a second picture is taken after the atoms moved out of view due to gravity [100, pp.58–66].

3.7.2. Temperature measurement

The temperature of the atoms is measured by observing the expansion of the atomic cloud as a function of time, which is also called time-of-flight measurement (TOF). Assuming a Gaussian shape of the cloud, its density distribution is (with the waist w)

$$n(r) = n_0 e^{-\frac{2r^2}{w^2}}, \quad (3.8)$$

where a spherical symmetry was presumed with radial coordinate r . The expansion of the atomic cloud due to the non-zero atomic velocities results in a growth of the waist following

$$w^2(t) = w_0^2 + (\Delta v)^2 t^2. \quad (3.9)$$

Using equation 2.22, the velocity spread Δv can be replaced by temperature T yielding

$$T = \frac{m}{k_B} \left(\frac{\sigma^2(t) - \sigma_0^2}{t^2} \right) \quad (3.10)$$

with the atomic mass m and the Boltzmann constant k_B [100, pp.66–67]. w_0 is the waist at $t = 0$, measurements are done after different expansion times and the temperature T is obtained by fitting a straight line to multiple datapoints ($\sigma(t)$ over t).

To sum up, an imaging system consisting of the six MOT beams (causing the atoms to fluoresce), an objective and a CMOS camera is used to determine the atom num-

3. Experimental setup

ber and temperature, the former to determine the population difference between the hyperfine ground states, the latter to characterize the performance of the cooling processes and to quantify temperature-dependent systematic effects in experiments.

4. Outlook

This thesis mostly consists of design and groundwork towards a cold atom experiment with potassium. At the time of writing, the further setup of the experiment was slowed down by the Covid-19 pandemic. However, the DDS generators, and the controlling system (secs. 3.4 and 3.5) have largely been set up. The next steps include the finalization of the optical and vacuum setup and the characterization of the magnetic field coils to eventually trap potassium atoms. Along the way, the UHF antennas have to be built, and the electron source needed to perform the Quantum Klystron (QUAK) experiment has to be finished, leading the way to perform first experiments with cold atoms.

Appendix

A. DDS Frequency generator design and schematics

In this section, further details on the DDS frequency generator presented in section 3.4 are given. In fig. 1, the wiring of the components is shown. The *Arduino adapter board* (also see the schematic in fig. 3) is attached to the U2 and U13 pin header rows of the EVAL-AD9959 featuring a SN74LVC541APWR buffer driver which transforms the 5 V level from the Arduino Nano to the 3.3 V signal level of the AD9959 chip. Two ACPL-772L optical isolators are used to protect the trigger pins of the AD9959 used to start frequency sweeps. The power supply board (see fig. 2) produces voltages of 1.8 V and 3.3 V with LDO regulators (LD117V18 and LD1117V33, *Low Dropout Regulators* are linear regulators with a low voltage drop, [94, p.611]) for the AD9959 Eval board and the VVAs (Minicircuits ZX73-2500(-S)+). Between the 1.8 V supplies for digital and analog parts of the AD9959, a ferrite bead (Murata BLM41PG750SN1L) is placed to avoid the 500 MHz clock signal interfering on the analog part of the circuit ([90]).

DDS frequency generator wiring diagram

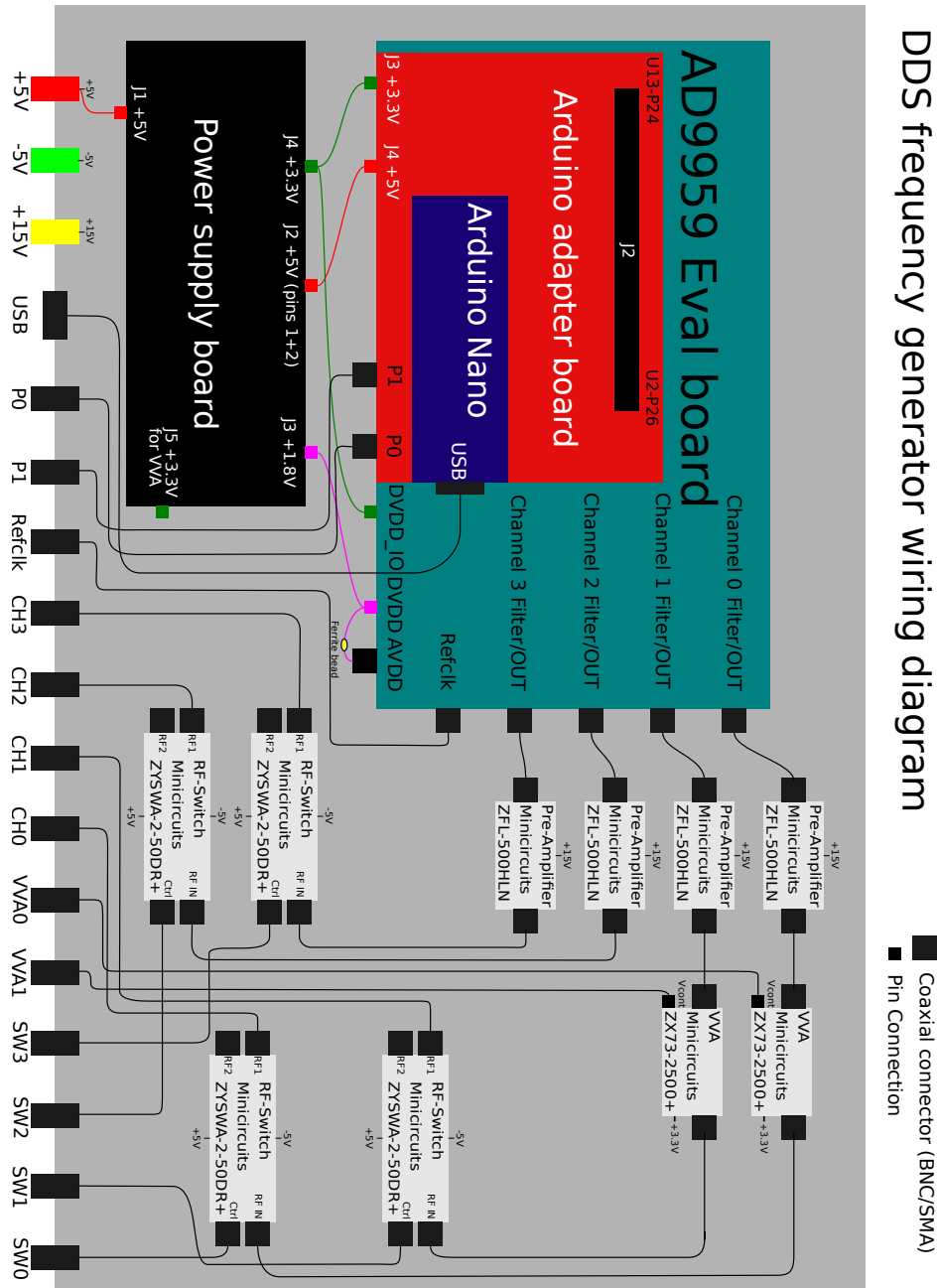


Figure 1.: The wiring digram of the DDS frequency generators: The AD9959 Eval board draws its power from the power supply board (see fig. 2) and is controlled by and Arduino Nano, which is connected via the Arduino Adapter Board. The latter also provides optocouplers to protect the trigger pins (used for the frequency sweeps) of the AD9959 chip. The further setup is a more detailed version of fig. 3.9.

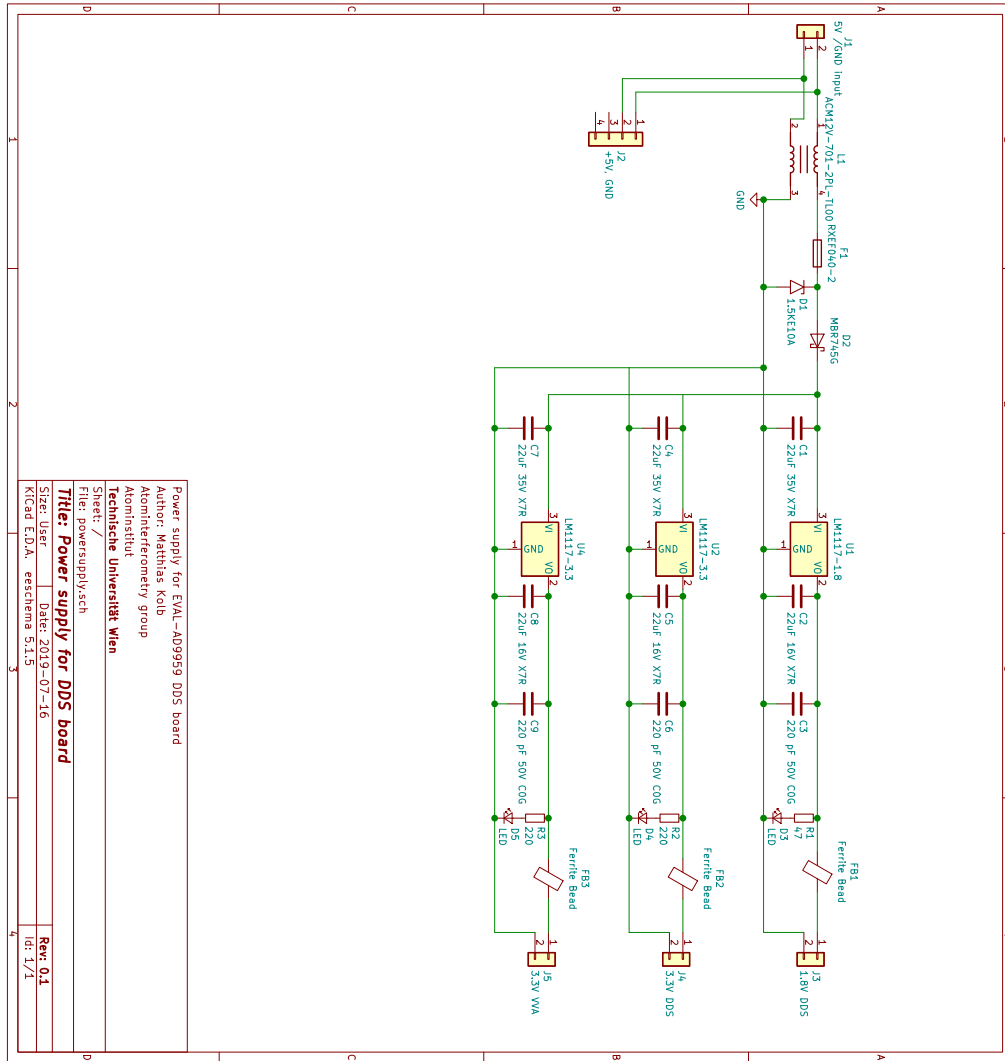


Figure 2.: Schematic of the board supplying power for the AD9959 Eval board and the VVAs. Multi-Layer Ceramic Capacitors (MLCC, X7R and C0G dielectrics) are used as storage capacitors because of the low equivalent series resistance (ESR) to suppress ripple from the supply voltage. Ferrite beads (Murara BLM41PG750SN1L) damp higher frequencies.

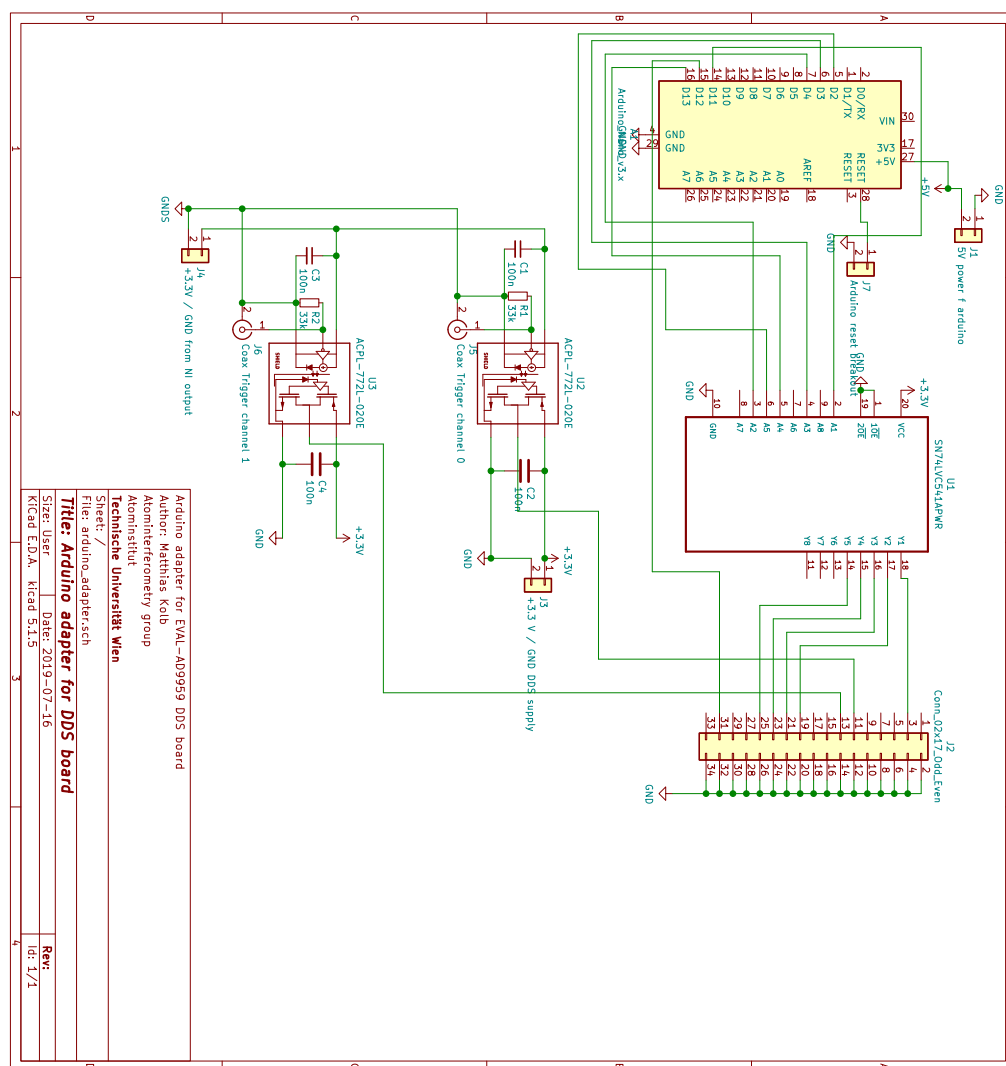


Figure 3.: The schematic of the Arduino adapter board provides a buffer driver (U1) to transform the 5 V logic level of the Arduino to the 3.3 V of the AD9959. Two optocouplers (U2 and U3) protect the trigger inputs of the AD9959 (used to start frequency sweeps).

List of Figures

1.1. The proposed Quantum Klystron experiment	2
2.1. The Doppler cooling process.	7
2.2. The D1 and D2 lines for ^{39}K and ^{41}K	9
2.3. Feshbach resonances: Lennard-Jones potential and scattering length	11
2.4. Feshbach resonances of ^{39}K	12
2.5. Saturation absorption spectroscopy and generation of an error signal	14
2.6. Frequency modulation spectroscopy	16
2.7. The principle of a magneto-optical trap in one dimension	21
2.8. The quadrupole magnetic field	23
2.9. The 3D MOT	24
2.10. The pyramidal MOT	25
2.11. The 2D MOT	30
2.12. Polarization gradient cooling with circular polarization	34
2.13. The gray molasses cooling process	38
2.14. The principle of degenerate Raman-sideband cooling	44
3.1. The vacuum chamber	48
3.2. The 2D MOT setup	50
3.3. Setup and stabilization of the TA pro 765 used to generate the D2 light for the experiment	53
3.4. Setup and stabilization of the DL 100 laser producing the D1 light needed for gray molasses and Raman sideband cooling	55
3.5. Acousto-optic modulators	57
3.6. The optical setup producing the frequencies needed for laser cooling	59
3.7. The frequencies needed for laser cooling	60
3.8. The cage system which is attached to the vacuum chamber	61
3.9. The DDS frequency generator	64
3.10. The controlling system	67
3.11. Magnetic fields for the 3D MOT	70
3.12. The coil configuration of the 2D MOT	71
3.13. The magnetic field gradients of the 2D MOT	73
3.14. First measurements of the 2D MOT coils	74

List of Figures

1.	DDS frequency generator wiring diagram	79
2.	Schematic of the powersupply board	80
3.	Schematics of the Arduino adapter board	81

List of Tables

2.1. Important transitions of ^{39}K	11
2.2. Important transitions of ^{41}K	12
2.3. Feshbach resonances of ^{39}K	13

List of Symbols

Acronyms / Abbreviations

AOM	Acousto-optic modulator
BEC	Bose-Einstein condensate
CMOT	Compressed magneto-optical trap
DDS	Direct digital synthesis
dRSC	degenerate Raman sideband cooling
ECDL	External-cavity diode laser
FMS	Frequency modulation spectroscopy
FWHM	Full width half maximum
LATIN	Lattice atom interferometry
LVIS	Low velocity intense source
MOT	Magneto-optical trap
MTS	Modulation transfer spectroscopy
PBS	Polarizing beam splitter
PCB	Printed circuit board
QUAK	Quantum Klystron
SPOT	Spontaneous-force optical trap
TA	Tapered amplifier
TOF	Time of flight

UHF Ultra high frequency

VSCPT Velocity-selective coherent population trapping

VVA Variable voltage attenuator

Constants

ϵ_0 Electric vacuum permittivity $8.854 \times 10^{-12} \text{ F m}^{-1}$

\hbar Reduced Planck constant $\frac{h}{2\pi} = 1.055 \times 10^{-34} \text{ J s}$

μ_0 Magnetic vacuum permeability $1.257 \times 10^{-6} \text{ N A}^{-2}$

a_B Bohr radius $5.292 \times 10^{-11} \text{ m}$

c Speed of light $2.998 \times 10^8 \text{ m s}^{-1}$

h Planck's constant $6.626 \times 10^{-34} \text{ J s}$

k_B Boltzmann constant $1.381 \times 10^{-23} \text{ J K}^{-1}$

m_e Electron mass $9.109 \times 10^{-31} \text{ kg}$

Acknowledgements

Finally, I would like to thank all the people that helped during my thesis and will still be helping setting up the experiment afterwards. First of all, I am grateful to Philipp Haslinger, my supervisor, for the opportunity to conduct my thesis in his group, for guiding me through the process of starting a new experiment and igniting my enthusiasm towards electronics. Additionally, he facilitated my first conference and the opportunity to visit other scientific groups.

I thank my colleagues Thomas Weigner and Samuel Rind working on the vacuum and optical setup respectively, for their ideas and support. I am especially grateful to Thomas for providing his thorough L^AT_EX thesis template and to Sam and Daniel Hartley for help with my thesis. I would like to thank our postdoc, Michael Scheucher, for general advice on cold atoms experiments. Furthermore, I appreciate the work of the theorists Dennis Rätzel and Daniel Hartley together with Philipp Haslinger, who laid the groundwork for the QUAK experiment.

For help and fruitful discussions I am grateful to Michael Gröbner, Rugway Wu, Andrzej Pelczar, Stefanie Manz, Dennis Schlippert, Alexander Herbst, Johannes Majer, Pawel Arciszewski, Mateusz Bochenski, Étienne Wodey, Isabella Fritzsche, Jakub Dobosz and many more.

Finally, several project students helped setting up lasers, spectroscopy and the controlling system, namely Nicolas Weilguny, Frank Ebel and Katharina Buczolich.

Numerous schematics in this thesis were created using the ComponentLibrary (<http://www.gwoptics.org/ComponentLibrary/>) by Alexander Franzen, licensed under a Creative Commons Attribution-NonCommercial 3.0 Unported License (<https://creativecommons.org/licenses/by-nc/3.0/>).

References

- [1] W. D. Phillips, “Laser cooling and trapping of neutral atoms”, *Reviews of Modern Physics*, 1998. DOI: [10.1103/RevModPhys.70.721](https://doi.org/10.1103/RevModPhys.70.721).
- [2] E. A. Cornell and C. E. Wieman, “Nobel Lecture: Bose-Einstein condensation in a dilute gas, the first 70 years and some recent experiments”, *Reviews of Modern Physics*, 2002. DOI: [10.1103/RevModPhys.74.875](https://doi.org/10.1103/RevModPhys.74.875).
- [3] W. Ketterle, “Nobel lecture: When atoms behave as waves: Bose-Einstein condensation and the atom laser”, *Reviews of Modern Physics*, 2002. DOI: [10.1103/RevModPhys.74.1131](https://doi.org/10.1103/RevModPhys.74.1131).
- [4] A. Morales, P. Zupancic, J. Léonard, T. Esslinger, and T. Donner, “Coupling two order parameters in a quantum gas”, *Nature Materials*, 2018. DOI: [10.1038/s41563-018-0118-1](https://doi.org/10.1038/s41563-018-0118-1).
- [5] I. Buluta and F. Nori, “Quantum Simulators”, *Science*, 2009. DOI: [10.1126/science.1177838](https://doi.org/10.1126/science.1177838).
- [6] M. Jaffe, P. Haslinger, V. Xu, *et al.*, “Testing sub-gravitational forces on atoms from a miniature in-vacuum source mass”, *Nature Physics*, 2017. DOI: [10.1038/nphys4189](https://doi.org/10.1038/nphys4189).
- [7] P. Haslinger, M. Jaffe, V. Xu, *et al.*, “Attractive force on atoms due to blackbody radiation”, *Nature Physics*, 2018. DOI: [10.1038/s41567-017-0004-9](https://doi.org/10.1038/s41567-017-0004-9).
- [8] R. H. Parker, C. Yu, W. Zhong, B. Estey, and H. Müller, “Measurement of the fine-structure constant as a test of the Standard Model”, *Science*, 2018. DOI: [10.1126/science.aap7706](https://doi.org/10.1126/science.aap7706).
- [9] S. M. Dickerson, J. M. Hogan, A. Sugarbaker, D. M. S. Johnson, and M. A. Kasevich, “Multi-axis Inertial Sensing with Long-Time Point Source Atom Interferometry”, *Physical Review Letters*, 2013. DOI: [10.1103/PhysRevLett.111.083001](https://doi.org/10.1103/PhysRevLett.111.083001).
- [10] B. Barrett, L. Antoni-Micollier, L. Chichet, *et al.*, “Dual matter-wave inertial sensors in weightlessness”, *Nature Communications*, 2016. DOI: [10.1038/ncomms13786](https://doi.org/10.1038/ncomms13786).
- [11] H. Müntinga, H. Ahlers, M. Krutzik, *et al.*, “Interferometry with Bose-Einstein Condensates in Microgravity”, *Physical Review Letters*, 2013. DOI: [10.1103/PhysRevLett.110.093602](https://doi.org/10.1103/PhysRevLett.110.093602).
- [12] V. Xu, M. Jaffe, C. D. Panda, *et al.*, “Probing gravity by holding atoms for 20 seconds”, *Science*, 2019. DOI: [10.1126/science.aay6428](https://doi.org/10.1126/science.aay6428).

- [13] D. Rätzel, D. Hartley, O. Schwartz, and P. Haslinger. (2020). “A Quantum Klystron – Controlling Quantum Systems with Modulated Electron Beams”, [Online]. Available: <http://arxiv.org/abs/2004.10168>.
- [14] A. S. Gilmour, *Klystrons, Traveling Wave Tubes, Magnetrons, Crossed-Field Amplifiers, and Gyrotrons*, ser. Artech House Microwave Library. Boston, MA: Artech House, 2011.
- [15] G. K. Brennen, C. M. Caves, P. S. Jessen, and I. H. Deutsch, “Quantum Logic Gates in Optical Lattices”, *Physical Review Letters*, 1999. DOI: [10.1103/PhysRevLett.82.1060](https://doi.org/10.1103/PhysRevLett.82.1060).
- [16] A. Omran, H. Levine, A. Keesling, *et al.*, “Generation and manipulation of Schrödinger cat states in Rydberg atom arrays”, *Science*, 2019. DOI: [10.1126/science.aax9743](https://doi.org/10.1126/science.aax9743).
- [17] P. Rez, T. Aoki, K. March, *et al.*, “Damage-free vibrational spectroscopy of biological materials in the electron microscope”, *Nature Communications*, 2016. DOI: [10.1038/ncomms10945](https://doi.org/10.1038/ncomms10945).
- [18] P. Haslinger. (2018). “Lattice Atom Interferometry (LATIN). FWF START grant abstract.”, [Online]. Available: https://pf.fwf.ac.at/project_pdfs/pdf_abstracts/y1121e.pdf (visited on 04/13/2020).
- [19] G. Salomon, L. Fouché, P. Wang, *et al.*, “Gray-molasses cooling of ^{39}K to a high phase-space density”, *EPL (Europhysics Letters)*, 2013. DOI: [10.1209/0295-5075/104/63002](https://doi.org/10.1209/0295-5075/104/63002).
- [20] M. Gröbner, P. Weinmann, E. Kirilov, and H.-C. Nägerl, “Degenerate Raman sideband cooling of ^{39}K ”, *Physical Review A*, 2017. DOI: [10.1103/PhysRevA.95.033412](https://doi.org/10.1103/PhysRevA.95.033412).
- [21] W. Demtröder, *Experimentalphysik 1*, ser. Springer-Lehrbuch. Berlin, Heidelberg: Springer Berlin Heidelberg, 2013. DOI: [10.1007/978-3-642-25466-6](https://doi.org/10.1007/978-3-642-25466-6).
- [22] H. J. Metcalf and P. van der Straten, *Laser Cooling and Trapping*, ser. Graduate Texts in Contemporary Physics. New York: Springer-Verlag, 1999. DOI: [10.1007/978-1-4612-1470-0](https://doi.org/10.1007/978-1-4612-1470-0).
- [23] T. Tiecke. (2011). “Properties of Potassium”, [Online]. Available: <http://www.tobiastiecke.nl/archive/PotassiumProperties.pdf> (visited on 01/20/2020).
- [24] W. Demtröder, *Experimentalphysik 3*, ser. Springer-Lehrbuch. Berlin, Heidelberg: Springer Berlin Heidelberg, 2010. DOI: [10.1007/978-3-642-03911-9](https://doi.org/10.1007/978-3-642-03911-9).
- [25] International Association of Sound and Audiovisual Archives. (2009). “Guidelines on the Production and Preservation of Digital Audio Objects”, [Online]. Available: <https://www.iasa-web.org/tc04/optical-disc-introduction> (visited on 08/07/2020).

- [26] C. J. Pethick and H. Smith, *Bose–Einstein Condensation in Dilute Gases*, 2nd ed. Cambridge: Cambridge University Press, 2008.
DOI: [10.1017/CBO9780511802850](https://doi.org/10.1017/CBO9780511802850).
- [27] D. A. Steck. (2019). “Rubidium 87 D Line Data”,
[Online]. Available: <http://steck.us/alkalidata/rubidium87numbers.pdf>.
- [28] C. Fort, A. Bambini, L. Cacciapuoti, *et al.*, “Cooling mechanisms in potassium magneto-optical traps”, *The European Physical Journal D - Atomic, Molecular and Optical Physics*, 1998. DOI: [10.1007/s100530050154](https://doi.org/10.1007/s100530050154).
- [29] D. Schlippert, “Quantum Tests of the Universality of Free Fall”, dissertation, Gottfried Wilhelm Leibniz Universität Hannover, 2014.
- [30] M. Gröbner, “A quantum gas apparatus for ultracold mixtures of K and Cs”, dissertation, Universität Innsbruck, 2017.
- [31] C. Chin, R. Grimm, P. Julienne, and E. Tiesinga, “Feshbach Resonances in Ultracold Gases”, version 2, *Reviews of Modern Physics*, 2010.
DOI: [10.1103/RevModPhys.82.1225](https://doi.org/10.1103/RevModPhys.82.1225).
- [32] C. D’Errico, M. Zaccanti, M. Fattori, *et al.*, “Feshbach resonances in ultracold ^{39}K ”, *New Journal of Physics*, 2007. DOI: [10.1088/1367-2630/9/7/223](https://doi.org/10.1088/1367-2630/9/7/223).
- [33] D. W. Preston, “Dopplerfree saturated absorption: Laser spectroscopy”, *American Journal of Physics*, 1998. DOI: [10.1119/1.18457](https://doi.org/10.1119/1.18457).
- [34] L. Mudarikwa, K. Pahwa, and J. Goldwin, “Sub-Doppler modulation spectroscopy of potassium for laser stabilization”, *Journal of Physics B: Atomic, Molecular and Optical Physics*, 2012.
DOI: [10.1088/0953-4075/45/6/065002](https://doi.org/10.1088/0953-4075/45/6/065002).
- [35] L. Corman, “Towards a novel ultracold Rubidium experiment”, Master thesis, ETH Zürich.
- [36] C. C. Gerry and P. Knight, *Introductory Quantum Optics*. Cambridge, UK ; New York: Cambridge University Press, 2005.
- [37] D. J. McCarron, S. A. King, and S. L. Cornish, “Modulation transfer spectroscopy in atomic rubidium”, *Measurement Science and Technology*, 2008.
DOI: [10.1088/0957-0233/19/10/105601](https://doi.org/10.1088/0957-0233/19/10/105601).
- [38] M. Landini,
“A tunable Bose-Einstein condensate for quantum interferometry”, PhD Thesis, Università degli Studi di Trento, 2011.
- [39] W. Demtröder, *Experimentalphysik 2*, ser. Springer-Lehrbuch. Berlin, Heidelberg: Springer Berlin Heidelberg, 2013.
DOI: [10.1007/978-3-642-29944-5](https://doi.org/10.1007/978-3-642-29944-5).
- [40] G. Salomon, “Production tout optique de condensats de Bose-Einstein de ^{39}K : des interactions contrôlables pour l’étude de gaz quantiques désordonnés en dimensions réduites”, dissertation, Institut d’Optique Graduate School, 2014.

- [41] K. I. Lee, J. A. Kim, H. R. Noh, and W. Jhe, “Single-beam atom trap in a pyramidal and conical hollow mirror”, *Optics Letters*, 1996. DOI: [10.1364/OL.21.001177](https://doi.org/10.1364/OL.21.001177).
- [42] M. Vangeleyn, P. F. Griffin, E. Riis, and A. S. Arnold, “Laser cooling with a single laser beam and a planar diffractor”, *Optics Letters*, 2010. DOI: [10.1364/OL.35.003453](https://doi.org/10.1364/OL.35.003453).
- [43] F. Shimizu, K. Shimizu, and H. Takuma, “Four-beam laser trap of neutral atoms”, *Optics Letters*, 1991. DOI: [10.1364/OL.16.000339](https://doi.org/10.1364/OL.16.000339).
- [44] C. Wieman, G. Flowers, and S. Gilbert, “Inexpensive laser cooling and trapping experiment for undergraduate laboratories”, *American Journal of Physics*, 1995. DOI: [10.1119/1.18072](https://doi.org/10.1119/1.18072).
- [45] W. D. Phillips and H. Metcalf, “Laser Deceleration of an Atomic Beam”, *Physical Review Letters*, 1982. DOI: [10.1103/PhysRevLett.48.596](https://doi.org/10.1103/PhysRevLett.48.596).
- [46] T. E. Barrett, S. W. Dapore-Schwartz, M. D. Ray, and G. P. Lafyatis, “Slowing atoms with σ^- polarized light”, *Physical Review Letters*, 1991. DOI: [10.1103/PhysRevLett.67.3483](https://doi.org/10.1103/PhysRevLett.67.3483).
- [47] G. E. Marti, R. Olf, E. Vogt, A. Öttl, and D. M. Stamper-Kurn, “Two-element Zeeman Slower for Rubidium and Lithium”, *Physical Review A*, 2010. DOI: [10.1103/PhysRevA.81.043424](https://doi.org/10.1103/PhysRevA.81.043424).
- [48] Z. T. Lu, K. L. Corwin, M. J. Renn, *et al.*, “Low-Velocity Intense Source of Atoms from a Magneto-optical Trap”, *Physical Review Letters*, 1996. DOI: [10.1103/PhysRevLett.77.3331](https://doi.org/10.1103/PhysRevLett.77.3331).
- [49] S. Weyers, E. Auccouturier, C. Valentin, and N. Dimarcq, “A continuous beam of cold cesium atoms extracted from a two-dimensional magneto-optical trap”, *Optics Communications*, 1997. DOI: [10.1016/S0030-4018\(97\)00312-X](https://doi.org/10.1016/S0030-4018(97)00312-X).
- [50] K. Dieckmann, R. J. C. Spreeuw, M. Weidemüller, and J. T. M. Walraven, “Two-dimensional magneto-optical trap as a source of slow atoms”, *Physical Review A*, 1998. DOI: [10.1103/PhysRevA.58.3891](https://doi.org/10.1103/PhysRevA.58.3891).
- [51] T. Uehlinger, “A 2D Magneto-Optical Trap as a High-Flux Source of Cold Potassium Atoms”, Master thesis, ETH Zürich, 2008.
- [52] J. Catani, P. Maioli, L. De Sarlo, F. Minardi, and M. Inguscio, “Intense slow beams of bosonic potassium isotopes”, *Physical Review A*, 2006. DOI: [10.1103/PhysRevA.73.033415](https://doi.org/10.1103/PhysRevA.73.033415).
- [53] J. R. Kellogg, D. Schlippert, J. M. Kohel, *et al.*, “A compact high-flux cold atom beam source”, *Applied Physics B*, 2012. DOI: [10.1007/s00340-012-5220-5](https://doi.org/10.1007/s00340-012-5220-5).
- [54] J. Arlt, O. Maragò, S. Webster, S. Hopkins, and C. Foot, “A pyramidal magneto-optical trap as a source of slow atoms”, *Optics Communications*, 1998. DOI: [10.1016/S0030-4018\(98\)00499-4](https://doi.org/10.1016/S0030-4018(98)00499-4).

- [55] J. M. Kohel, J. Ramirez-Serrano, R. J. Thompson, *et al.*, “Generation of an intense cold-atom beam from a pyramidal magneto-optical trap: Experiment and simulation”, *Journal of the Optical Society of America B*, 2003. DOI: [10.1364/JOSAB.20.001161](https://doi.org/10.1364/JOSAB.20.001161).
- [56] W. Petrich, M. H. Anderson, J. R. Ensher, and E. A. Cornell, “Behavior of atoms in a compressed magneto-optical trap”, *Journal of the Optical Society of America B*, 1994. DOI: [10.1364/JOSAB.11.001332](https://doi.org/10.1364/JOSAB.11.001332).
- [57] D. E. Pritchard, E. L. Raab, V. Bagnato, C. E. Wieman, and R. N. Watts, “Light Traps Using Spontaneous Forces”, *Physical Review Letters*, 1986. DOI: [10.1103/PhysRevLett.57.310](https://doi.org/10.1103/PhysRevLett.57.310).
- [58] W. Ketterle, K. B. Davis, M. A. Joffe, A. Martin, and D. E. Pritchard, “High densities of cold atoms in a *dark* spontaneous-force optical trap”, *Physical Review Letters*, 1993. DOI: [10.1103/PhysRevLett.70.2253](https://doi.org/10.1103/PhysRevLett.70.2253).
- [59] P. D. Lett, W. D. Phillips, S. L. Rolston, *et al.*, “Optical molasses”, *JOSA B*, 1989. DOI: [10.1364/JOSAB.6.002084](https://doi.org/10.1364/JOSAB.6.002084).
- [60] P. L. Gould, P. D. Lett, and W. D. Phillips, “New Measurements with Optical Molasses”, in *Laser Spectroscopy VIII*, W. Persson and S. Svanberg, Eds., ser. Springer Series in Optical Sciences, Berlin, Heidelberg: Springer, 1987. DOI: [10.1007/978-3-540-47973-4_16](https://doi.org/10.1007/978-3-540-47973-4_16).
- [61] J. Dalibard and C. Cohen-Tannoudji, “Laser cooling below the Doppler limit by polarization gradients: Simple theoretical models”, *Journal of the Optical Society of America B*, 1989. DOI: [10.1364/JOSAB.6.002023](https://doi.org/10.1364/JOSAB.6.002023).
- [62] M. Landini, S. Roy, L. Carcagní, *et al.*, “Sub-Doppler laser cooling of potassium atoms”, *Physical Review A*, 2011. DOI: [10.1103/PhysRevA.84.043432](https://doi.org/10.1103/PhysRevA.84.043432).
- [63] A. Aspect, E. Arimondo, R. Kaiser, N. Vansteenkiste, and C. Cohen-Tannoudji, “Laser Cooling below the One-Photon Recoil Energy by Velocity-Selective Coherent Population Trapping”, *Physical Review Letters*, 1988. DOI: [10.1103/PhysRevLett.61.826](https://doi.org/10.1103/PhysRevLett.61.826).
- [64] M. Weidemüller, T. Esslinger, M. A. Ol’shanii, A. Hemmerich, and T. W. Hänsch, “A Novel Scheme for Efficient Cooling below the Photon Recoil Limit”, *Europhysics Letters (EPL)*, 1994. DOI: [10.1209/0295-5075/27/2/006](https://doi.org/10.1209/0295-5075/27/2/006).
- [65] D. Nath, R. K. Easwaran, G. Rajalakshmi, and C. S. Unnikrishnan, “Quantum-interference-enhanced deep sub-Doppler cooling of ^{39}K atoms in gray molasses”, *Physical Review A*, 2013. DOI: [10.1103/PhysRevA.88.053407](https://doi.org/10.1103/PhysRevA.88.053407).
- [66] M. Gröbner, P. Weinmann, F. Meinert, *et al.*, “A new quantum gas apparatus for ultracold mixtures of K and Cs and KCs ground-state molecules”, *Journal of Modern Optics*, 2016. DOI: [10.1080/09500340.2016.1143051](https://doi.org/10.1080/09500340.2016.1143051).

- [67] H.-Z. Chen, X.-C. Yao, Y.-P. Wu, *et al.*, “Production of large ^{41}K Bose-Einstein condensates using D1 gray molasses”, *Physical Review A*, 2016. DOI: [10.1103/PhysRevA.94.033408](https://doi.org/10.1103/PhysRevA.94.033408).
- [68] R. Grimm, M. Weidemüller, and Y. B. Ovchinnikov. (1999). “Optical dipole traps for neutral atoms”, [Online]. Available: <http://arxiv.org/abs/physics/9902072>.
- [69] S. E. Hamann, D. L. Haycock, G. Klose, *et al.*, “Resolved-Sideband Raman Cooling to the Ground State of an Optical Lattice”, *Physical Review Letters*, 1998. DOI: [10.1103/PhysRevLett.80.4149](https://doi.org/10.1103/PhysRevLett.80.4149).
- [70] A. J. Kerman, V. Vuletic, C. Chin, and S. Chu, “Beyond Optical Molasses: 3D Raman Sideband Cooling of Atomic Cesium to High Phase-Space Density”, *Physical Review Letters*, 2000. DOI: [10.1103/PhysRevLett.84.439](https://doi.org/10.1103/PhysRevLett.84.439).
- [71] J. Hu, A. Urvoy, Z. Vendeiro, *et al.*, “Creation of a Bose-condensed gas of ^{87}Rb by laser cooling”, *Science*, 2017. DOI: [10.1126/science.aan5614](https://doi.org/10.1126/science.aan5614).
- [72] M. H. Anderson, J. R. Ensher, M. R. Matthews, C. E. Wieman, and E. A. Cornell, “Observation of Bose-Einstein Condensation in a Dilute Atomic Vapor”, *Science*, 1995. DOI: [10.1126/science.269.5221.198](https://doi.org/10.1126/science.269.5221.198).
- [73] M. Gröbner, “Aufbau und Charakterisierung eines Lasersystems zum Kühlen und Fangen von Kalium-Atomen”, Master thesis, Universität Innsbruck.
- [74] R. Charrière, M. Cadoret, N. Zahzam, Y. Bidet, and A. Bresson, “Local gravity measurement with the combination of atom interferometry and Bloch oscillations”, *Physical Review A*, 2012. DOI: [10.1103/PhysRevA.85.013639](https://doi.org/10.1103/PhysRevA.85.013639).
- [75] X. Zhang, R. P. del Aguila, T. Mazzoni, N. Poli, and G. M. Tino, “Trapped-atom interferometer with ultracold Sr atoms”, *Physical Review A*, 2016. DOI: [10.1103/PhysRevA.94.043608](https://doi.org/10.1103/PhysRevA.94.043608).
- [76] G. W. Biedermann, X. Wu, L. Deslauriers, K. Takase, and M. A. Kasevich, “Low-noise simultaneous fluorescence detection of two atomic states”, *Optics Letters*, 2009. DOI: [10.1364/OL.34.000347](https://doi.org/10.1364/OL.34.000347).
- [77] N. F. Ramsey, “A Molecular Beam Resonance Method with Separated Oscillating Fields”, *Physical Review*, 1950. DOI: [10.1103/PhysRev.78.695](https://doi.org/10.1103/PhysRev.78.695).
- [78] M. Dupont-Nivet, M. Casiulis, T. Laudat, C. I. Westbrook, and S. Schwartz, “Microwave-stimulated Raman adiabatic passage in a Bose-Einstein condensate on an atom chip”, *Physical Review A*, 2015. DOI: [10.1103/PhysRevA.91.053420](https://doi.org/10.1103/PhysRevA.91.053420).
- [79] M. Jaffe, “Atom interferometry in an optical cavity”, dissertation, University of California, Berkeley, 2018.
- [80] R. Bücker, A. Perrin, S. Manz, *et al.*, “Single-particle-sensitive imaging of freely propagating ultracold atoms”, *New Journal of Physics*, 2009. DOI: [10.1088/1367-2630/11/10/103039](https://doi.org/10.1088/1367-2630/11/10/103039).

- [81] V. Gokhroo, G. Rajalakshmi, R. K. Easwaran, and C. S. Unnikrishnan, “Sub-Doppler deep-cooled bosonic and fermionic isotopes of potassium in a compact 2D⁺-3D MOT setup”, *Journal of Physics B: Atomic, Molecular and Optical Physics*, 2011. DOI: [10.1088/0953-4075/44/11/115307](https://doi.org/10.1088/0953-4075/44/11/115307).
- [82] Toptica Photonics AG, “DL pro Grating Stabilized Diode Laser Head designed for DLC pro”, Manual, Gräfelfing, 2018.
- [83] Toptica Photonics AG, “TA pro Tapered Amplifier System designed for DLC pro”, Manual, Gräfelfing, 2018.
- [84] Toptica Photonics AG, “DLC pro Digital Laser Controller”, Manual, Gräfelfing, 2018.
- [85] Toptica Photonics AG, “DL 100 Grating Stabilized Diode Laser Head”, Manual, Gräfelfing, 2006.
- [86] Toptica Photonics AG, “Sys DC 110 Diode Laser Supply Electronics”, Manual, Gräfelfing, 2017.
- [87] D. J. McCarron. (2007). “A Guide to Acousto-Optic Modulators”, [Online]. Available: <http://www.jila1.nickersonm.com/papers/A%20Guide%20to%20Acousto-Optic%20Modulators.pdf> (visited on 04/17/2020).
- [88] E. A. Donley, T. P. Heavner, F. Levi, M. O. Tataw, and S. R. Jefferts, “Double-pass acousto-optic modulator system”, *Review of Scientific Instruments*, 2005. DOI: [10.1063/1.1930095](https://doi.org/10.1063/1.1930095).
- [89] G. H. Zhang, B. Braverman, A. Kawasaki, and V. Vuletic, “Note: Fast compact laser shutter using a direct current motor and three-dimensional printing”, *Review of Scientific Instruments*, 2015. DOI: [10.1063/1.4937614](https://doi.org/10.1063/1.4937614).
- [90] E. Murphy and C. Slattery. (2004). “All About Direct Digital Synthesis | Analog Devices”, [Online]. Available: <https://www.analog.com/en/analog-dialogue/articles/all-about-direct-digital-synthesis.html> (visited on 04/20/2020).
- [91] Mini Circuits. (2015). “Understanding VCO Concepts”, [Online]. Available: <https://www.minicircuits.com/app/AN95-007.pdf> (visited on 04/20/2020).
- [92] Mini Circuits. (1999). “Phase locked loop fundamentals”, [Online]. Available: <https://www.minicircuits.com/app/VCO15-10.pdf> (visited on 04/20/2020).
- [93] Analog Devices. (2008). “AD9959 datasheet”, [Online]. Available: <https://www.analog.com/media/en/technical-documentation/data-sheets/AD9959.pdf> (visited on 04/20/2020).
- [94] P. Horowitz, *The Art of Electronics*, Third edition. New York: Cambridge University Press, 2015.

References

- [95] Analog Devices. (2005). “AD9959/PCB Evaluation Board”, [Online]. Available: https://www.analog.com/media/en/technical-documentation/evaluation-documentation/57418637811849AD9959_pcb_0.pdf (visited on 04/20/2020).
- [96] A. Keshet and W. Ketterle, “A Distributed GUI-based Computer Control System for Atomic Physics Experiments”, *Review of Scientific Instruments*, 2013. DOI: [10.1063/1.4773536](https://doi.org/10.1063/1.4773536).
- [97] National Instruments. (2018). “PCIe-6738 Specifications”, [Online]. Available: <https://www.ni.com/pdf/manuals/377270b.pdf> (visited on 05/18/2020).
- [98] SAL - Silicon Austria Labs. (2019). “Magpylib”, [Online]. Available: <https://magpylib.readthedocs.io/en/latest/> (visited on 06/29/2020).
- [99] R. Dengler, “Self inductance of a wire loop as a curve integral”, *Advanced Electromagnetics*, 1 2016. DOI: [10.7716/aem.v5i1.331](https://doi.org/10.7716/aem.v5i1.331).
- [100] G. Valtolina, “Development of an experimental apparatus for the production and study of ultracold atomic gases of fermionic lithium”, Master thesis, Università degli Studi di Milano - Bicocca, 2012.